

Structure and reactivity of iron and copper-containing high-silica zeolites

Citation for published version (APA):

Li, G. (2013). *Structure and reactivity of iron and copper-containing high-silica zeolites*. [Phd Thesis 1 (Research TU/e / Graduation TU/e), Chemical Engineering and Chemistry]. Technische Universiteit Eindhoven.
<https://doi.org/10.6100/IR750184>

DOI:

[10.6100/IR750184](https://doi.org/10.6100/IR750184)

Document status and date:

Published: 01/01/2013

Document Version:

Publisher's PDF, also known as Version of Record (includes final page, issue and volume numbers)

Please check the document version of this publication:

- A submitted manuscript is the version of the article upon submission and before peer-review. There can be important differences between the submitted version and the official published version of record. People interested in the research are advised to contact the author for the final version of the publication, or visit the DOI to the publisher's website.
- The final author version and the galley proof are versions of the publication after peer review.
- The final published version features the final layout of the paper including the volume, issue and page numbers.

[Link to publication](#)

General rights

Copyright and moral rights for the publications made accessible in the public portal are retained by the authors and/or other copyright owners and it is a condition of accessing publications that users recognise and abide by the legal requirements associated with these rights.

- Users may download and print one copy of any publication from the public portal for the purpose of private study or research.
- You may not further distribute the material or use it for any profit-making activity or commercial gain
- You may freely distribute the URL identifying the publication in the public portal.

If the publication is distributed under the terms of Article 25fa of the Dutch Copyright Act, indicated by the "Taverne" license above, please follow below link for the End User Agreement:

www.tue.nl/taverne

Take down policy

If you believe that this document breaches copyright please contact us at:

openaccess@tue.nl

providing details and we will investigate your claim.

Structure and Reactivity of Iron and Copper-Containing High-Silica Zeolites

PROEFSCHRIFT

ter verkrijging van de graad van doctor aan de
Technische Universiteit Eindhoven, op gezag van de
rector magnificus, prof.dr.ir. C.J. van Duijn, voor een
commissie aangewezen door het College voor
Promoties in het openbaar te verdedigen
op donderdag 7 maart 2013 om 16.00 uur

door

Guanna Li

geboren te Ruzhou, China

Dit proefschrift is goedgekeurd door de promotoren:

prof.dr. R.A. van Santen
en
prof.dr. C. Li

Copromotor:

dr. E.A. Pidko

A catalogue record is available from the Eindhoven University of Technology Library

ISBN: 978-90-386-3333-6

Cover design: Fengtao Fan (DICP) and Guanna Li

Printed by: Ipskamp Drukkers



**Inorganic
Materials
Chemistry**

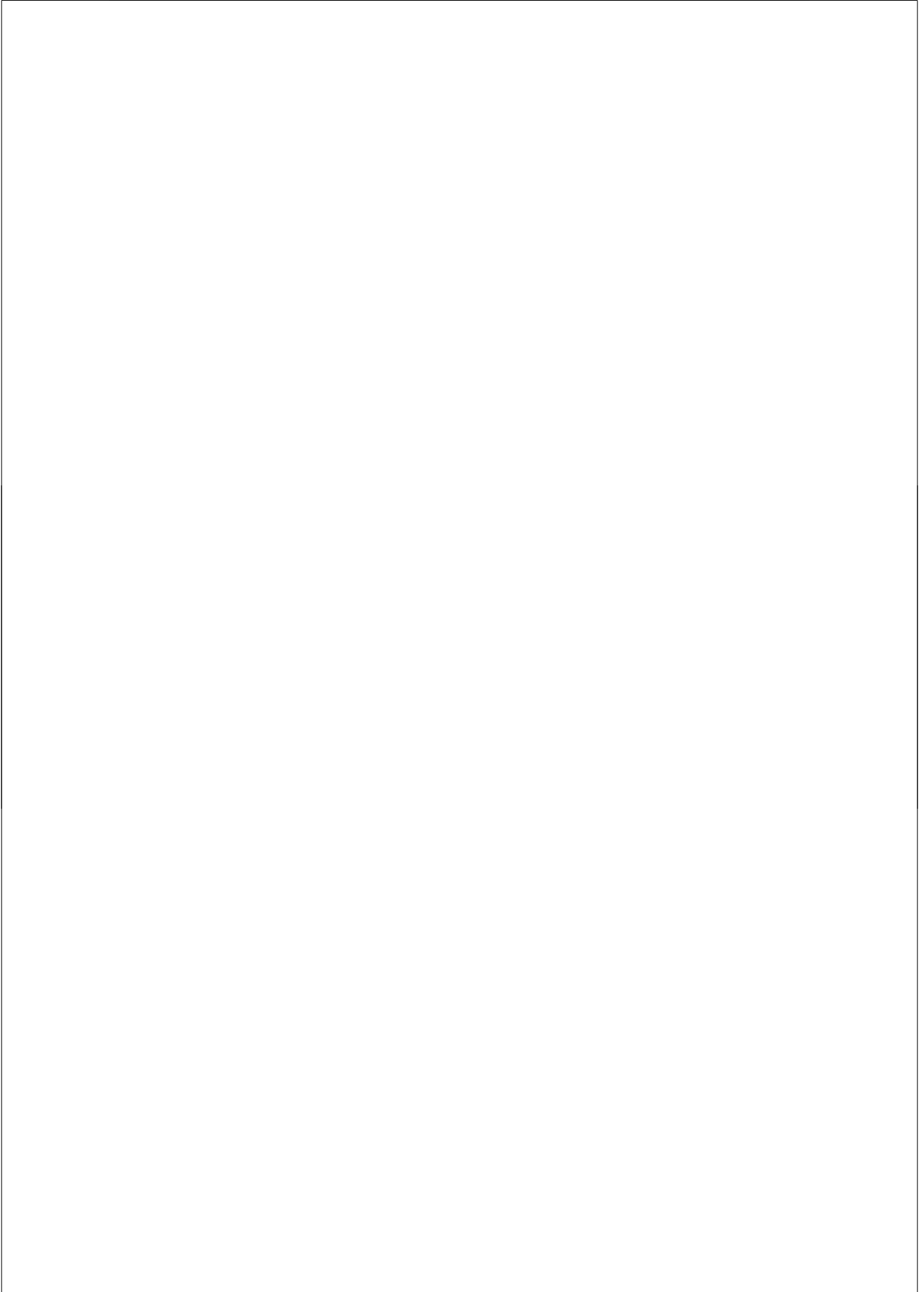
Department of Chemical Engineering & Chemistry



This work is part of the research programme for Strategic Scientific Alliances between China and The Netherlands (2008DFB50130). The computational facilities were supported by the National Computing Facilities Foundation (NCF).

Copyright © 2013 by Guanna Li





CONTENTS

STRUCTURE AND REACTIVITY OF IRON AND COPPER-CONTAINING HIGH-SILICA ZEOLITES

Chapter 1. Introduction	1
Chapter 2. Stability of extraframework iron-containing complexes in ZSM-5 zeolite	17
Chapter 3. Direct benzene oxidation to phenol in Fe/ZSM-5: a comprehensive periodic DFT study	49
Chapter 4. Catalytic properties of extraframework iron-containing species in ZSM-5 for N ₂ O decomposition	73
Chapter 5. On the nature of active sites and mechanism of selective methane oxidation over Cu/ZSM-5 zeolite	97
Summary	115
Acknowledgements	119
List of publications	123
Curriculum vitae	125



CHAPTER 1

INTRODUCTION

1.1. What are zeolites?

Zeolites are naturally occurring mineral combinations of microporous aluminosilicates that can be found in rock deposits around the world. The term zeolite is rooted in the Greek words ζέω (zédō), meaning “to boil”, and λίθος (líthos), meaning “stone”. More than 200 years ago, a Swedish mineralogist named Axel Fredrik Cronstedt discovered a mineral that upon heating produced large amounts of steam from water that could be then adsorbed back into the “stone” upon its cooling. This observation inspired him to name the mineral using the Greek words meaning “stone that boils” – zeolite [1].

Zeolites are formed in nature when ancient volcanic ash flows react with fresh groundwater or sea water in neighboring seas and lakes. Abundant zeolite minerals can be found in sedimentary rocks. Because such deposits are usually located near the surface of earth, they had been produced by hydrothermal synthesis at temperatures around 25-150 °C. Geological processes require anywhere between 50 and 10,000 years to complete the formation of zeolites. Nature-occurring zeolites are very similar by their composition to clay minerals. Despite both types of materials are aluminosilicates, they are characterized by distinctly different crystalline structures. Clays have layered crystalline structures and therefore can undergo shrinking and swelling when water molecules enter or leave the interlayer space upon adsorption or desorption, respectively. In contrast, crystal structures of zeolites are represented by rigid three-dimensional networks of interconnected channels and cages resembling honeycombs. Water and other molecules can enter and escape from these channels and cages without significantly affecting the crystalline lattice of zeolites.

A representative and key property of zeolites is that their frameworks are made up of interconnected networks of elementary silica and/or alumina units. The term “zeolite” corresponds to a crystalline aluminosilicate or a microporous silica polymorph constructed of $[\text{SiO}_4]$ and $[\text{AlO}_4]$ tetrahedral elementary building units. These $[\text{TO}_4]$ (T = Si and Al) tetrahedra are linked through corner-sharing oxygen atoms resulting in a three-dimensional framework with uniformly sized pores of molecular dimensions (Figure 1.1). Therefore, the net formulae of the structure-forming tetrahedra in these materials are SiO_2 and AlO_2 .

One should note that, the unit of one $[\text{AlO}_2]$ has a negative charge of -1 when the T-center of tetrahedron is Al^{3+} , whereas it is neutral of one $[\text{SiO}_2]$ unit since in this case the T-center is Si^{4+} . To have a charge-neutral material, these $[\text{AlO}_2]^-$ framework anions require the presence of charge-compensating cations in their immediate vicinity, which can be protons or small cations such as Na^+ , K^+ , and others. An important peculiarity in zeolite chemistry is the principle of “aluminum avoidance” or Löwenstein’s rule [2]. According to this rule, the $\text{Al}-\text{O}-\text{Al}$ linkages in the zeolitic framework are forbidden. In materials prepared by normal hydrothermal routes only $\text{Si}-\text{O}-\text{Si}$ or $\text{Si}-\text{O}-\text{Al}$ linkages are allowed. Therefore, the degree of Al for Si substitution in zeolitic materials ranges from zero ($\text{Si}/\text{Al} = \infty$) to 1:2 ($\text{Si}/\text{Al} = 1$).

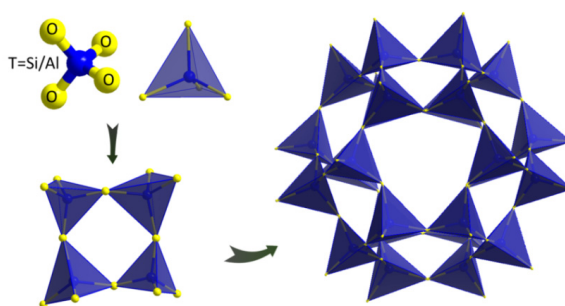


Figure 1.1. Building units of zeolite.

Naturally occurring zeolites are excluded from many important industrial and commercial applications because their uniformity and purity are usually quite low due to the contamination by other minerals such as different metal-containing materials, quartz, or other zeolites. While possessing similar unique structural and physicochemical properties, synthetic zeolites take some key advantages over their natural analogs. Synthetic zeolites can be manufactured in a uniform, phase-pure state on a large scale. More importantly, many desirable zeolites with specific structures that do not appear in nature can be successfully synthesized artificially. Because silica and alumina are among the most abundant mineral components on earth, the potential to supply feedstock for zeolite synthesis is virtually unlimited. On the other hand, the artificial synthesis processes requires significantly less time than the 50 to 50,000 years prescribed by nature. By the end of 2011, over 40 naturally occurring zeolite frameworks are known, whereas more than 150 unique zeolite frameworks have been synthesized (Figure 1.2) [3].

Being a well-defined crystalline porous aluminosilicates, zeolites have many important and sometimes unique physical and chemical properties. Zeolites are widely used in water purification, softening, and other applications as ion-exchange reagents. In the petrochemical industry, synthetic zeolites play an important role as catalysts for fluid catalytic cracking and hydrocracking. When the lattice anionic charges of zeolites are compensated by protons, the resulting so-called hydrogen form of zeolites show pronounced Brønsted acidity. The intrazeolitic Brønsted acid sites that can be formally

viewed as H^+AlO_2^- structure units make such materials powerful solid acids that can promote a wide variety of acid-catalyzed reactions such as isomerization, alkylation, and cracking [4]. In addition to the presence of well-defined active sites in their microporous space, there is a range of specific structural characteristics for microporous materials that make zeolites particularly important both for academia and industry. These include the shape and size of pores that define how molecules are confined inside the zeolite matrix, the accessible void space dictating whether molecules of particular size can actually enter its pores, the dimensionality of the channel system that influences the way molecules diffuse through the zeolite crystal, the number and local structure of cationic sites as well as strong electric fields within the micropores determining the way how molecules are adsorbed and activated inside zeolites [5]. Therefore, development of a systematic and in-depth molecular-level understanding of how all these factors influence and control particular chemical processes occurring within zeolites is crucial for further rational design of novel and improved zeolite-based materials tailored for a specific application.

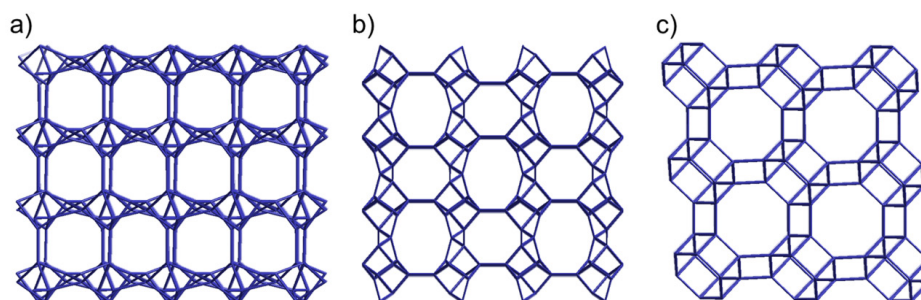


Figure 1.2. Three different structural variations of zeolites: a) chain-like structures; b) sheet-like structures; c) framework structures equant in dimensions.

1.2. Extraframework transition metal cations in zeolites

One important property of zeolites is their ability to participate in ion-exchange reactions. As it was mentioned before, the negative charges on the zeolite lattice introduced by the isomorphous substitution of silicon with aluminum atoms are normally compensated by Brønsted acidic protons bonded to bridging oxygen atoms connecting framework silicons and aluminums or by other exchangeable cations (Na^+ , K^+ , Mg^{2+} et al.) located in the channels or cages of the zeolite matrix [6]. More important is that these H^+ ions or metal cations can be further exchanged by other cationic species, especially by transition metal cations. The incorporation of various transition metal ions, such as iron, copper, cobalt ions, into these materials can drastically change the chemical properties of zeolites making them active and efficient catalysts for a wide range of redox processes [7].

The catalytic properties of transition metal-exchanged zeolites are strongly influenced by the composition, location, and structures of the reactive metal species introduced into the microporous space [8]. Because of the poor control over the process of the introduction of

metal species into the zeolite matrix, in real catalysts the exchanged transition metal-containing species are often quite heterogeneously dispersed over the zeolite micropores resulting in the formation of isolated ions, dimers, oligomers and oxidic clusters. The identification of the active sites for a particular chemical transformation in such a mixture by using conventional characterization techniques is very challenging [9]. In many cases, one can identify the active oxidation state of the transition metal ions, but the nuclearity of these species and their structural properties cannot be determined unambiguously.

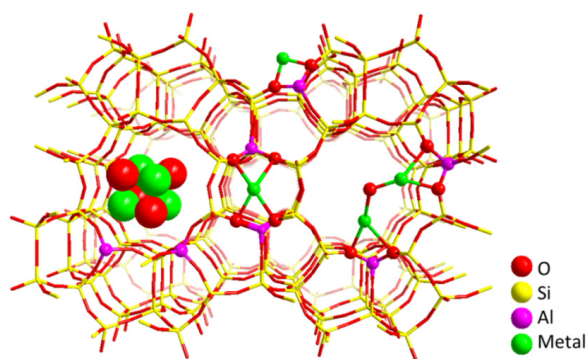


Figure 1.3. Schematic representation of different transition metal species confined in zeolite micropores: isolated M^+ , M^{2+} , binuclear $[M(\mu-O)M]^{2+}$, and M_xO_y clusters in zeolite channels.

The actual location of exchanged extraframework transition metal-containing species depends on several factors such as the charge of the metal ions, the loading of the metal, the exchange method, zeolite morphology, framework Si/Al ratio, and the sample preparation conditions (Figure 1.3). Monovalent cations usually occupy zeolitic rings containing a singly negatively-charged lattice $[AlO_2]^-$ unit. Their distribution depends only slightly on the local framework configurations of the zeolite and the relative location of lattice Al ions. However, for bivalent and multivalent cations, the situation is much more complicated. In principle, at low loading and for low-silica zeolites where almost all cationic sites contain two or more Al ions, the transition metal ions prefer to occupy the exchange sites where they can form a maximal number of direct coordination bonds with the lattice oxygen atoms. The negatively-charged framework oxygen atoms of $[AlO_2]^-$ tetrahedra are preferentially coordinated to the cations than those of the neutral $[SiO_2]$ tetrahedra. This leads to site distortions of the local zeolite structure, and the cations are not located exactly in the center of the zeolitic rings. At high loading, cations can also be present at energetically less favorable sites with fewer coordinations to the lattice oxygen atoms. In this case, however, the structural properties of the introduced cationic species may be much more complicated. Because of the inability of the zeolite matrix to provide sufficient stabilization for the isolated exchangeable cations they can transform to various species including mononuclear, binuclear, and oligonuclear cationic and neutral complexes

that may coexist in the system. It is extremely difficult to distinguish between them using most of the conventional experimental characterization techniques that provide with averaged signals over all configurations present in the actual microporous materials. For high silica zeolite, such as mordenite and ZSM-5, oxygen and hydroxyl bridged multinuclear cationic species or neutral clusters may be formed preferentially, because in such materials the possibility of direct charge-compensation of mononuclear bivalent cation with two Al centers coexisting in the first coordination sphere is low. Moreover, for such complexes it has been proposed that their location and stability in silica-rich zeolite is mostly determined by the favorable coordination environment of the metal ions, while the direct interaction with the negative lattice oxygen atoms is less important.

Generally speaking, the distribution of the extraframework cations depends on the structural properties of the zeolites and the chemistry of the transition metal ions themselves. The fundamental knowledge of the locations and structures of active metal complexes in zeolites is of particular interest for the development of novel transition metal-exchanged zeolite catalysts with high selectivity and activity for specific chemical transformations. However, due to a rather low concentration, high dispersion, and heterogenous nature of transition metal species presented in the zeolite pores, it is still a big challenge to obtain reliable information on their structural and electronic properties.

1.3. C–H activation and O₂ evolution: from nature to zeolite

The academic research and applications of transition metal-exchanged zeolites have been driven in last decades by their promising reactivity in a wide range of chemical processes related to the fields of environmental and green chemistry. The use of such materials containing only abundant elements as active and selective catalysis is expected to play an important role in the current global efforts in reducing toxic waste streams and energy consumption. Among all the applications reported for these systems, mild selective oxidation of hydrocarbons is of great interest and is recognized as one of the grand challenges for catalysis. This is because of the necessity to develop more sustainable and energy-efficient routes for functionalization of very inert C–H bonds in hydrocarbon feedstocks. The simplest hydrocarbon, methane, is the most difficult one to oxidize selectively. The C–H bond energy in methane is equal to 436 kJ/mol. A number of approaches that employ C–H activation as the key step have been explored and developed for the conversion of hydrocarbon to useful chemicals and fuels [10]. The current industrial strategies normally employ indirect multistep reforming which is energy consuming, and lacks selectivity. In principle, the procedure of direct oxidation of C–H bond can proceed with a much higher efficiency. However, the development of the respective processes is hampered by that fact that under the conditions when the low reactive C–H bonds are being activated, the typically more reactive desired products are also consumed before they are recovered from the reactor [11, 12].

Another application of cation-exchanged zeolites is related to the removal of pollutants

from industrial waste streams. A representative example is N₂O (nitrous oxide) that is emitted during the production of nitric and adipic acids. This compound is recognized as one of the major sources of nitrogen oxides (NO_x) depleting the ozone layer in the stratosphere and the third greenhouse gas following CO₂ and CH₄. Therefore, the direct catalytic decomposition of N₂O into N₂ and O₂ is considered as one of the most convenient and economical ways to reduce its negative environmental impact.

Nature had a longer time than chemists and appeared to be more successful so far in developing a system capable of promoting the processes described above. Methanotrophic bacteria are capable of oxidizing methane as their sole source of carbon and energy. The reaction is initiated by an enzymatic system called methane monooxygenase (MMO) through selective oxidation of the stable C–H bond of methane under ambient conditions. Two types of MMO have been isolated from methanotrophs: soluble methane monooxygenase (sMMO) and particulate methane monooxygenase (pMMO). For pMMO, it has been evidenced that one of the copper clusters present in its complex structure is the active site for methane hydroxylation and the other one acts as an electron carrier [13]. The active site of sMMO contains a non-heme diiron Fe₂O₂ diamond core structure, in which iron is present in a formal IV valent state [14]. In contrast to pMMO, sMMO is able to promote oxidation of a wide variety of hydrocarbon substrates besides methane and therefore, has attracted much more attention from researchers both in academia and industry [15].

Besides their ability to activate methane, these enzymes are also highly active in O₂ activation to form specific active oxygen species that are actually responsible for the functionalization of strong C–H bonds in hydrocarbons. It is therefore important to consider how O₂ can be activated or formed in nature. A very related reaction, evolution of molecular oxygen, is one of the key fundamental process on Earth that is catalyzed by enzyme photosystem II (PSII) upon water splitting driven by the sunlight. The active site of oxygen evolving complex (OEC) inside the PSII is an inorganic metal oxidic Mn₃Ca–oxo cubane cluster with a dangler Mn ion attached [16]. The mechanism of O₂ evolution has been described by the ingenious five-step *S*-state Kok cycle proposed in 1970 [17]. The reaction cycle is driven by the absorption of four photons in a sequence from the dark-stable most reduced *S*₀ to the most oxidized *S*₄ electronic state, then O–O bond is formed and O₂ is released in the *S*₄ → *S*₀ transition by oxidation of two water molecules [18, 19]. Although the *S*-states cycle is well established, the structure, valence charges and the chemical function of the catalytic Mn cluster in the different *S*-state have been intensively debated and a complete understanding of this subject is still far from being achieved. The biggest challenge is related to the least known *S*₄ state even though several Mn-oxo and peroxide containing intermediates have been proposed to be crucial for the formation of the O–O bond and generation of molecular oxygen [18, 20, 21].

Whereas the successful application of the enzymatic catalysis for methane activation on an industrial scale is associated with a number of serious problems, chemical insights

gathered from enzymological studies could guide further development of next generations of artificial model catalysts. In the branch of homogeneous catalysis, both organometallic and coordination chemists have attempted to understand or even reproduce the reactivity of enzymes by studying homogeneous transition metal complexes [22, 23]. For the direct oxidation conversion of methane to methanol derivatives, partial success has been achieved using platinum complexes derived from the bidiazine ligand [24]. Since then, a large number of second- and third-row transition metal complexes have been studied for their reactivity towards activation of various hydrocarbon substrates [25-27]. Furthermore, biologically important metal ions, for example, Fe, Cu, Mn, and analogues have been employed by coordination chemist. For O₂ evolution, Mn-, Ru-, Co-, and other metal-based supramolecular systems have been developed to mimic the natural PSII process [28-31]. In any case, there are three common requirements needed to be met for the development of an effective homogeneous metal catalyst for this process: coordinative unsaturation, electronic unsaturation, and adjustable oxidation state of the metal centers for providing the accessibility to the reactants and for accommodating of the electrons from ligands [32, 33].

The zeolite framework can also be viewed as a ligand that stabilizes the exchanged transition metal cations. With its crystalline and robust character, the zeolite framework has an ability to accommodate various catalytic species located in the well-defined chemical environment. The microporous channels and nanosized cages of zeolites also ensure good accessibility of the active centers and can impose specific confinement on the adsorbed reagents beneficial for their subsequent chemical activation. Furthermore, specific crystalline structures of zeolites are helpful to improve our understanding of how the structure of solid ligands influences the properties of the catalytic species and reaction mechanism. The fundamental insights generated this way have a potential to form a basis for further rational design of heterogeneous catalytic systems with tailored properties towards selective transformation of particular substrates to the desired chemicals. The shape selectivity of zeolite is also regarded as one of their key properties to improve the reaction selectivity. Based on these considerations, transition metal-exchanged zeolites can be viewed as the closest and best-defined heterogeneous counterparts of homogeneous and enzymatic systems [34, 35]. It has been widely reported that transition metal-exchanged zeolites show high catalytic activities towards several important reactions which find close analogues in the oxidation reactions promoted by homogeneous catalysts and enzymes.

Despite many studies have been carried out related to these topics and impressive progress that has been achieved so far, both the homogeneous and heterogeneous systems have suffered from similar disadvantages, such as low selectivity, catalyst instability, and high temperature and pressure requirement. On the other hand, the exact structures of the active sites and the reaction mechanism are still ambiguous and under hot debate. Whereas the analogy with homogeneous and enzymatic complexes is clearly apparent, in the case of zeolitic catalysts, the encapsulated transition metal-containing cationic species have their own specific structural properties. It is a great challenge to understand their catalytic

properties at the molecular level.

It is important to note that the reactions involving the activation or the formation of molecular O₂ are best promoted by the systems capable of an easy spin-crossing between two different electronic states in the course of the reaction. For organometallic complexes, reactions involving such a spin crossing transition are regarded as a fundamental concept and have been described in literature [36-39]. The reactions involving transitions between different electronic states can provide a lower energy path compared to the difficult process involving a single electronic configuration. It is expected that these proposal can be extended onto transition metal-exchanged zeolite system. Thus, the question of the preferred ground state electronic structure of intrazeolitic metal-containing complexes and its change along the reaction coordinate is of crucial importance for understanding the nature of active sites and chemical reactivity of these systems.

1.4. Structure features of ZSM-5 zeolite

The catalytic properties of extraframework transition metal-containing species are strongly influenced by the particular topologies and the microporous environment of zeolites. In this thesis, the iron and copper exchanged ZSM-5 zeolites have been the main focus of the investigation. ZSM-5 is one of the most widely used zeolites in industrial applications. ZSM-5 zeolites modified with iron (Fe/ZSM-5) and copper (Cu/ZSM-5) have been shown to be highly active systems for several important chemical processes that can readily be catalyzed by enzymes. It was thus proposed that these systems can be viewed as solid analogues of enzymatic catalysts with some specific sites present in their micropores that mimicking structural and electronic properties of the active components of the biocatalysts.

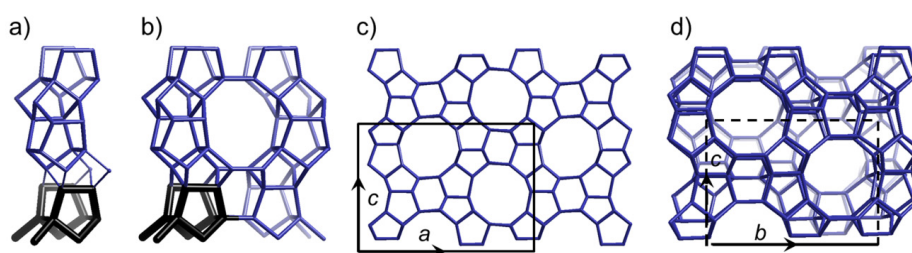


Figure 1.4. MFI structure: a) secondary building block and chains viewed along *a* axis; b) left- and right-hand chains formed by blocks; c) Layer formed from linked chains; d) periodic ZSM-5 structure.

ZSM-5 (Zeolite Socony Mobil – 5) zeolite has been originally reported by Argauer and Landelt in 1972. This material is an important member of the so-called pentasil family and is characterized by an MFI framework type. It is a representative type of high silica zeolites with a chemical formula of Na_{*n*}Al_{*n*}Si_{96-*n*}O₁₉₂·16H₂O. The ratio of Si/Al can be

adjusted in the range from 12 to infinity. The unit cell is orthorhombic with *Pnma* symmetry ($a = 20.07 \text{ \AA}$, $b = 19.92 \text{ \AA}$, and $c = 13.42 \text{ \AA}$) [40].

The secondary building block of ZSM-5 framework is a pentasil unit containing 12 T atoms consisting of two 5-1 units shown in bold in Figure 1.4a. These blocks can be linked to form left- and right-handed chains (Figure 1.4b), which can then be interconnected to form layers (Figure 1.4c). Neighboring chains in these layers are actually mirror images of each other. Finally, a periodic MFI crystal structure is formed by connecting these layers together (Figure 1.4d).

ZSM-5 is a highly porous material which has an effective three-dimensional channel system defined by ten-membered ring openings throughout its structure. The first type is a straight channel running parallel to the *b*-axis of the unit cell, along (010) direction (Figure 1.4c). The estimated pore size of the straight channels is $5.3 \times 5.6 \text{ \AA}$ with elliptical shape in the cross section. The second type is sinusoidal channel perpendicular to the straight one along (100) direction with an opening of $5.1 \times 5.5 \text{ \AA}$ (Figure 1.4d). The dimension of intersection between the two channels is ca. 9 \AA [3].

ZSM-5 may show different behavior depending on the type of molecules introduced into its pores because of these peculiarities of its channel system. For example, diffusion, adsorption/desorption, reaction rate, and formation of reaction intermediates and final products may vary to a great extent depending on the size and shape of the interacting molecules. As a result, ZSM-5 has found application in petroleum refining as a catalyst because it shows a good shape-selectivity properties.

1.5. Computational methods

In the past two decades both experiment and computational approaches have been extensively used to reveal the nature of the reactive species in zeolites and to create a molecular-level picture of the reaction mechanisms. Through computations one can obtain very detailed information about chemical systems that is not readily available from experiments. This is especially true for such properties as geometry and electronic structure of catalytic sites in heterogeneous catalysts, the overall mechanism, and the nature of elementary steps within a catalytic cycle. All these issues can be investigated at a high level of details by using electronic structure methods on representative model systems. Such methods are in the heart of quantum chemistry.

Quantum chemistry is a branch of theoretical chemistry, which uses quantum mechanics to answer such chemical questions as the structural and electronic properties of materials, provide insight into the mechanisms of chemical reactions etc. In order to do this, one has to solve the Schrödinger equation for the system concerned

$$i\hbar \frac{\partial \Psi(\mathbf{r}, t)}{\partial t} = \hat{H} \Psi(\mathbf{r}, t)$$

where Ψ is the time-dependent wave function of the system, r is the coordinates of particles, and $\hat{H} = -\frac{\hbar^2}{2m}\nabla^2 + V(\mathbf{r})$ is the Hamiltonian operator, which is comprised of the kinetic and potential energy operators. In principle, if the Schrödinger equation is solved, one can obtain the wave function that then allows deriving all properties of a chemical system. For the most concerned systems, usually the potential energy is time independent. Therefore, we can use $\Psi(\mathbf{r},t) = \psi(\mathbf{r})f(t)$ to separate variables and get simplified time-independent Schrödinger equation as $\hat{H}\psi(\mathbf{r}) = E\psi(\mathbf{r})$, where E is the energy eigenvalue. Furthermore, as the mass of nucleus is much greater than that of electrons, each time the nucleus position changed, the electron will always reach to equilibrium very quickly. Thus, we use Born-Oppenheimer approximation to separate the electronic Schrödinger equation from the nuclear one for fixed nuclear positions. However, only hydrogen-like ion can be solved analytically. For many-body systems the main task for quantum chemistry is to solve the electronic Schrödinger equation approximately using different kinds of numerical methods [41].

Hartree-Fock (HF) method is one approach which assumes that each electron could be considered to be present within a mean field of other $N-1$ electrons, and the one-electron wave function is approximated by a linear combination of atomic orbitals, so that the set of equations are solved by iterative algorithm, which is called the self-consistent field (SCF) method. HF method has a great advantage that it is an *ab initio* method, i.e. it can be solved with a high numerical precision without using any experimental parameters.

However, a major deficiency of HF method is that it neglects electron correlation. The energy error between HF and the exact solution of electronic Schrödinger equation is called correlation energy. Although the correlation energy takes commonly very small percentage of the total energy, the error is important since the general chemical reaction energy is also at this magnitude. The resulting inaccuracy can lead to serious errors in the calculated energies, geometries, and other important properties.

A number of approaches to treat the electronic correlation have been developed so far. The associated computational methodologies are generally called post-Hartree-Fock methods (post-HF). These include for example Configuration Interaction (CI) [42], Møller-Plesset perturbation theory (MPn) [43], and Coupled Cluster (CC) [44]. CI method uses a variational wave function with a linear combination of Slater determinants, and is very accurate to handle the electronic correlation, but is limited to small systems for the immense calculation costs. Møller-Plesset perturbation theory adds multi-order perturbation to the HF Hamiltonian to treat the electronic correlation. MPn means the n^{th} order perturbation, and the CPU cost increases rapidly with increasing the order. MP2 is a cost-effective method that allows recovering $\sim 60\%$ of correlation energy. The shortcoming of MPn is the lack of variational principle to ensure the calculated energy always higher or equal to the real energy. Coupled cluster method constructs multi-electron wavefunctions using the exponential cluster operator to account for electron correlation. Despite their high

accuracy, post-HF methods are extremely demanding in terms of computational power. Therefore, their application is limited to only very small chemical systems.

Density functional theory (DFT) represents another approach to solve the electronic structure problems. It allows reducing the multi-body problem with $3N$ variables to only three spatial variables, and therefore becomes very attractive especially for studying large systems [45]. DFT is based on two fundamental Hohenberg-Kohn theorems:

- 1) The ground state energy is a unique functional of the electron density $\rho(\mathbf{r})$.
- 2) The electron density $\rho(\mathbf{r})$ obtained by minimization of the energy of the overall functional $E[\rho(\mathbf{r})]$ is the true electron density of a system.

Theorem 1 has proved that all the ground state properties of a multi-body system such as energy and wave function are uniquely determined by the electron density $\rho(\mathbf{r})$, which is a function of only three spatial variables. Theorem 2 provides an expression of the energy by variational principle as $E[\rho(\mathbf{r})] = E_{known}[\rho(\mathbf{r})] + E_{xc}[\rho(\mathbf{r})]$, where the functional is split into two parts. $E_{known}[\rho(\mathbf{r})] = T[\rho(\mathbf{r})] + U[\rho(\mathbf{r})]$ is a collection of terms held in a simple analytical form including the kinetic energy and the potential energy, and $E_{xc}[\rho(\mathbf{r})]$ is the exchange correlation functional, which is defined to include all the effects that are not included in the $E_{known}[\rho(\mathbf{r})]$ term.

Furthermore, the non-interacting single electron kinetic energy functional $T_s[\rho(\mathbf{r})]$ is used in place of $T[\rho(\mathbf{r})]$, and all the differences are again included in the $E_{xc}[\rho(\mathbf{r})]$. The density functional was composed by the N-electron wave function as $\rho(\mathbf{r}) = \sum_{i=1}^N |\phi_i(\mathbf{r})|^2$, so that the set of working equations named Kohn-Sham equations are derived as

$$\left(-\frac{\hbar^2}{2m} \nabla^2 + V_{KS}[\rho(\mathbf{r})] \right) \phi_i(\mathbf{r}) = E_i \phi_i(\mathbf{r})$$

where $V_{KS}[\rho(\mathbf{r})] \equiv V(\mathbf{r}) + V_{Coul}[\rho(\mathbf{r})] + V_{xc}[\rho(\mathbf{r})] = V(\mathbf{r}) + \int d\mathbf{r}' \frac{\rho(\mathbf{r}')}{|\mathbf{r} - \mathbf{r}'|} + \frac{\delta E_{xc}[\rho(\mathbf{r})]}{\delta \rho(\mathbf{r})}$ is named

Kohn-Sham potential including the interaction between an electron and the collection of atomic nuclei, $V(\mathbf{r})$, the Coulomb repulsion between the electron and the total electron density in the system, $V_{Coul}[\rho(\mathbf{r})]$ (also called the Hartree potential), and the exchange correlation functional, $V_{xc}[\rho(\mathbf{r})]$. Thus, the Kohn-Sham equations have a set of formally exact equations and can be solved iteratively [46]. However, the exact expression of the

exchange correlation functional is unknown. A number of approximations have to be made to solve the problem, such as local density approximation (LDA) [47], generalized gradient approximation (GGA) [48, 49], and other more sophisticated methods.

LDA simply assumes that each electron's exchange correlation energy at a given position is equivalent to that in a homogeneous electron gas at the same position. Thus, the exchange correlation potential of LDA is defined as $V_{xc}^{LDA}(\mathbf{r}) = V_{xc}^{electron\ gas}[\rho(\mathbf{r})]$, and has been used successfully for predicting bulk properties of solid materials, in which the valence electron density varies slowly. While for chemical reactions and many properties of molecules, LDA always overestimates bond energies since the electron density at the chemical bond is not generally uniform.

GGA improved LDA to describe the electron density by including the gradient of electron density on the spatial variation as $V_{xc}^{GGA}(\mathbf{r}) = V_{xc}[\rho(\mathbf{r}), \nabla\rho(\mathbf{r})]$. In this case the exchange correlation energy is the functional of both the density and its gradient. Many types of GGA functional have been developed such as Perdew-Wang 91 (PW91) functional [50] and Perdew-Burke-Ernzerhof (PBE) functional [51]. Though GGA is very popular in computational chemistry for its cost-effectiveness, there are still some drawbacks like the well-known underestimation of band gap in semiconductor and insulators, the inaccurate description of van der Waals attraction.

Further approximations beyond GGA have been developed to improve the computational results compared with LDA and GGA. Perdew has classified DFT methods by using Biblical account of "Jacob's ladder" [52]. The ground of Jacob's ladder is the Hartree theory that neglects all the exchange correlation parts in Kohn-Sham equation. The first rung of Jacob's ladder is LDA in which the electron density is included, the second rung is GGA in which additional gradient of electron density is embodied. The third rung is called meta-GGA, which includes additional information of the second derivative of the electron density. The fourth rung is a hybrid method that is also called hyper-GGA, which contains a mixture of the exact exchange and a GGA exchange. The widely used hyper-GGA in quantum chemistry calculations is B3LYP functional [53]. With the level of rung increasing, more information of exchange correlation functional is embraced, and the topmost of Jacob ladder is to reach the exact exchange correlation functional. Thus, Jacob ladder leads DFT to the "Heaven" of chemical accuracy. However, in practice a higher level method does not always mean a higher accuracy, but usually causes more computational demands. Therefore, one has to always find a reasonable compromise between the accuracy and the computational demands suitable for a particular chemical problem.

DFT has been widely used in quantum chemistry, especially in calculating the electronic properties and structural properties for relatively large systems [54]. As discussed above, both HF method and DFT method give their own approaches to solve the Schrödinger equation. However, in practice we need basis set whether to construct the wave functions

in HF or to construct the electron density in DFT. A basis set is a set of functions which are used to represent create molecular orbitals. Theoretically, any set of infinite number of functions can be combined to represent the true electronic structure or electron density. But in practice only finite number of such functions is used as basis set due to computational limitations. This further introduces errors in calculations. The choice for a certain basis set strongly depends on the type of the problem, the simulation model, the solution method selected, and the accuracy required when the so-called cluster model is employed to represent a chemical system. Basis sets based on Slater-type orbitals (STO) and Gaussian-type orbitals (GTO) are usually used. These basis sets decay exponentially with distance from the nuclei. They are very suitable to construct atomic orbitals. Therefore, these localized basis sets are commonly used for molecular systems. While for solids where models involve periodic boundary conditions to mimic “infinite” bulk systems, plane wave basis sets are often used under a specific cutoff energies for certain calculations, because they formally are components of Bloch wave function in Bloch theorem [55]. Bloch theorem has proven that $\psi(\mathbf{r})$, the solutions of the Schrödinger equation, have the same periodicity as the potential and follow an equation of $\psi(\mathbf{r} + \mathbf{R}_n) = e^{ik \cdot \mathbf{R}_n} \psi(\mathbf{r})$, where R_n is a periodic function especially concerned with the crystal symmetry, and k is the wave vector in reciprocal space. Based on Bloch theorem, the Schrödinger equation for periodic system can be solved efficiently and numerically by selected k samplings in the reduced reciprocal space i.e. the irreducible Brillouin zone.

In addition, the basis sets are not necessary to construct the full electron potentials since most of the core electrons in atoms are not changed during chemical processes. In practice, the core part is usually replaced by a smoothed density to match important criterions of the true one in order to reduce basis sets sizes and computational burdens. This is named effective core potential or pseudopotential method. The widely used methods including norm-conserving pseudopotentials, ultrasoft pseudopotentials (USPP), and projector-augmented-wave (PAW) method [56].

For chemical reactions, *ab initio* methods can be applied not only to investigate the thermodynamic properties like enthalpy, entropy, and free energies associated with the reaction intermediates or (semi) stable states. They can also be effectively used to study kinetics of chemical reaction by finding saddle points on the potential energy surface and therefore computing reaction activation energies. Based on transition state (TS) theory, elementary reaction pathway searching can be achieved by several algorithms, and the transition states as well as reaction barriers are therefore obtained. In principle, if the potential energy surface (PES) for a certain system is acquired, all the thermodynamic and kinetic information will be achieved. However, for systems even containing more than three atoms, the construction of a complete PES is unpractical. In practice, there are several algorithms for searching transition states. They are based on force analysis of atoms and could be categorized into mainly two types. One is the so-called “surface walking” which only needs a guess TS structure and then the optimization leads to a saddle

point based on the local force and curvature information, such as the dimer method [57]. The advantage of “surface walking” methods is that only a guess state is needed and the calculation cost is compatible to that of a structural relaxation. However, the searched saddle point formed need to be checked to correspond to a certain TS of the reaction. The other is the so-called “chain-of-states” which needs a series of structures between reaction initial state (IS) and final state (FS), such as the climbing image nudged elastic band method (CI-NEB) [58, 59]. These states are connected via a chain of structures, which are optimized mutually with neighbor states by specified potentials. The advantage of “chain-of-states” methods is that a reaction pathway is obtained to ensure the correct TS of the specified reaction.

The aim of this thesis is to understand the chemical properties and reaction mechanisms of species incorporated in zeolite matrix. Both the local structure of active site and the entire confinement of zeolite framework are considered. The calculations are accomplished by using the VASP code [60], which can be run on high performance computing platforms to get an approximate solution of the electronic structure problem for such large systems as zeolites. The interactions between electrons and ions chosen in this thesis are described using PAW method, and the electron orbital is expressed in plane wave basis sets, and the generalized gradient approximation PBE exchange and correlation functional is employed to describe the exchange and correlation energies.

1.6. Scope of this thesis

This thesis aims at developing a fundamental understanding of the factors that control structure and reactivity of extraframework cationic species in high-silica zeolites. The main focus of this work is on high-silica ZSM-5 zeolites modified with iron and copper. These systems are known to exhibit unique catalytic properties in selective oxidation reactions. Nevertheless, there is a lack of fundamental understanding of the factors controlling chemical reactivity of these catalysts. The main goal of this thesis is to obtain an insight into the structures of intrazeolitic iron and copper species as well as into mechanism of chemical transformations which they promote by periodic DFT calculations.

One of the main challenges in zeolite science is to determine the chemical state and location of extraframework transition metal-containing complexes in high-silica zeolite matrixes. By performing a comprehensive analysis of ZSM-5 structures confining various iron-containing cationic species, in **Chapter 2** an attempt is made to correlate between the structures of extraframework complexes, the geometry of the zeolitic cation site as well as local distribution of Al atoms in the framework. The potential reaction paths for the interconversion of different intrazeolitic species upon the high-temperature catalyst activation are investigated. The concept of self-organization of oxygenated and hydroxylated cations in high-silica zeolites is discussed. These results are used to propose a route for controlling the structural properties of the dominant species in cation-exchanged high-silica zeolites.

The state of cations in zeolites determines the reactivity of the actual catalyst. In **Chapter 3**, the reactivity towards selective oxidation of C–H bond of benzene is studied over selected mononuclear and binuclear iron-containing species. The specific locations of them in ZSM-5 are considered according to the stability study. An attempt is made to understand the cationic structure and zeolitic topology dependences of various potential active species towards benzene to phenol oxidation reaction in Fe/ZSM-5. The preferred catalytic pathway and the catalytic deactivation mechanism over oxygenated iron complexes are discussed.

Chapter 4 reports the catalytic properties of extraframework iron-containing species in ZSM-5 for direct N₂O decomposition and O₂ evolution. The reactivity and mechanisms over both mononuclear and binuclear sites are investigated and compared by DFT calculations. In this case, special attention is devoted to the spin-crossing effects of intermediates on reaction mechanism. The DFT results obtained are used to further identify the rate limited step, apparent activation barrier and reaction order as a function of temperature. It will be shown that such understanding is helpful for unraveling the fundamental factors that control reactivity of iron species in high-silica zeolites.

The relationship between the properties of extraframework complexes in ZSM-5 zeolites modified with copper and their reactivity in direct methane oxidation to methanol is studied in **Chapter 5**. In contrast to earlier proposals on the key role of binuclear cationic Cu sites, the possibilities for formation of alternative intrazeolitic Cu complexes with a higher degree of nuclearity are explored. The reactivity of potential multinuclear cationic copper-containing species towards homolytic C–H bond activation and the subsequent several possible reaction destinations of the confined mobile CH₃ radical in zeolite channel are investigated. The influences of several low-lying electronic ground states and the higher mobility of extraframework oxygen in Cu clusters with nuclearity higher than 2 on the rebound of the activated species and desorption of molecular methanol will be discussed.

References

- [1] A.F. Cronstedt. *Kungliga Svenska Vetenskapsakademiens Handlingar, Stockholm* 17 (1756) 120-123.
- [2] W. Löwenstein. *Am. Mineral* 39 (1954) 92.
- [3] I.Z. Association. *Database of Zeolite Structures*.
- [4] R.R. Xu, W.Q. Pang, J.H. Yu, Q.S. Huo, J.S. Chen. *Chemistry of zeolites and related porous materials* (2007).
- [5] A. Corma. *Chem. Rev.* 97 (1997) 2373-2419.
- [6] J. Weitkamp. *Solid State Ion.* 131 (2000) 175-188.
- [7] M. Hartmann, L. Kevan. *Chem. Rev.* 99 (1999) 635-663.
- [8] T. Frising, P. Leflaive. *Microporous Mesoporous Mat.* 114 (2008) 27-63.
- [9] R.A. Schoonheydt. *Chem. Soc. Rev.* 39 (2010) 5051-5066.
- [10] J.H. Lunsford. *Catal. Today* 63 (2000) 165-174.
- [11] C. Hammond, S. Conrad, I. Hermans. *Chemsuschem* 5 (2012) 1668-1686.
- [12] H. Schwarz. *Angew. Chem. Int. Edit.* 50 (2011) 10096-10115.
- [13] R.A. Himes, K.D. Karlin. *Curr. Opin. Chem. Biol.* 13 (2009) 119-131.
- [14] L.J. Shu, J.C. Nesheim, K. Kauffmann, E. Munck, J.D. Lipscomb, L. Que. *Science* 275 (1997) 515-518.

- [15] M. Merckx, D.A. Kopp, M.H. Sazinsky, J.L. Blazyk, J. Muller, S.J. Lippard. *Angew. Chem. Int. Edit.* 40 (2001) 2782-2807.
- [16] K.N. Ferreira, T.M. Iverson, K. Maghlaoui, J. Barber, S. Iwata. *Science* 303 (2004) 1831-1838.
- [17] B. Kok, B. Forbush, M. McGloin. *Photochem. Photobiol.* 11 (1970) 457-475.
- [18] M. Haumann, P. Liebisch, C. Muller, M. Barra, M. Grabolle, H. Dau. *Science* 310 (2005) 1019-1021.
- [19] H. Dau, M. Haumann. *Biochim. Biophys. Acta* 1767 (2007) 472-483.
- [20] P.E.M. Siegbahn. *Acc. Chem. Res.* 42 (2009) 1871-1880.
- [21] G.W. Brudvig. *Philos. Trans. R. Soc. B* 363 (2008) 1211-1218.
- [22] R. Mayilmurugan, H. Stoeckli-Evans, E. Suresh, M. Palaniandavar. *Dalton Trans.* (2009) 5101-5114.
- [23] A. Burkhardt, E.T. Spielberg, H. Goerls, W. Plass. *Inorg. Chem.* 47 (2008) 2485-2493.
- [24] R.A. Periana, D.J. Taube, S. Gamble, H. Taube, T. Satoh, H. Fujii. *Science* 280 (1998) 560-564.
- [25] B.A. Arndtsen, R.G. Bergman, T.A. Mobley, T.H. Peterson. *Acc. Chem. Res.* 28 (1995) 154-162.
- [26] R.A. Periana, G. Bhalla, W.J. Tenn, K.J.H. Young, X.Y. Liu, O. Mironov, C.J. Jones, V.R. Ziatdinov. *J. Mol. Catal. A* 220 (2004) 7-25.
- [27] J.A. Labinger, J.E. Bercaw. *Nature* 417 (2002) 507-514.
- [28] M.W. Kanan, Y. Surendranath, D.G. Nocera. *Chem. Soc. Rev.* 38 (2009) 109-114.
- [29] V. Artero, M. Chavarot-Kerlidou, M. Fontecave. *Angew. Chem. Int. Edit.* 50 (2011) 7238-7266.
- [30] L.C. Sun, L. Hammarstrom, B. Akermark, S. Styring. *Chem. Soc. Rev.* 30 (2001) 36-49.
- [31] K. Meelich, C.M. Zaleski, V.L. Pecoraro. *Philos. Trans. R. Soc. B* 363 (2008) 1271-1279.
- [32] T.A. Betley, Y. Surendranath, M.V. Childress, G.E. Alliger, R. Fu, C.C. Cummins, D.G. Nocera. *Philos. Trans. R. Soc. B* 363 (2008) 1293-1303.
- [33] R.H. Crabtree. *J. Chem. Soc., Dalton Trans.* (2001) 2437-2450.
- [34] A. Zecchina, M. Rivallan, G. Berlier, C. Lamberti, G. Ricchiardi. *Phys. Chem. Chem. Phys.* 9 (2007) 3483-3499.
- [35] P. Vanelderden, J. Vancauwenbergh, B.F. Sels, R.A. Schoonheydt. *Coord. Chem. Rev.* 257 (2013) 483-494.
- [36] H. Hirao, D. Kumar, L. Que, S. Shaik. *J. Am. Chem. Soc.* 128 (2006) 8590-8606.
- [37] P. Schroder, S. Shaik, H. Schwarz. *Acc. Chem. Res.* 33 (2000) 139-145.
- [38] P. Belanzoni, L. Bernasconi, E.J. Baerends. *J. Phys. Chem. A* 113 (2009) 11926-11937.
- [39] E.V. Kudrik, O. Safonova, P. Glatzel, J.C. Swarbrick, L.X. Alvarez, A.B. Sorokin, P. Afanasiev. *Appl. Catal. B* 113 (2012) 43-51.
- [40] D.H. Olson, G.T. Kokotailo, S.L. Lawton, W.M. Meier. *J. Phys. Chem.* 85 (1981) 2238-2243.
- [41] D.J. Griffiths. *Introduction to Quantum Mechanics, 2nd Edition* (2005).
- [42] J.A. Pople, M. Head-Gordon, K. Raghavachari. *J. Chem. Phys.* 87 (1987) 5967-5985.
- [43] C. Moller, M.S. Plesset. *Phys. Rev.* 46 (1934) 618-672.
- [44] J.A. Pople, R. Krishnan, H.B. Schlegel, J.S. Binkley. *Int. J. Quant. Chem.* 14 (1978) 545-560.
- [45] W. Koch, M.C. Holthausen. *A Chemist's Guide to Density Functional Theory* (2001).
- [46] W. Kohn, L. Sham. *Phys. Rev. A* 140 (1965) 1133-1138.
- [47] U. Von Barth, L. Hedin. *J. Phys. C: Solid State Phys.* 5 (1972) 1629-1640.
- [48] D.C. Langreth, J.P. Perdew. *Phys. Rev. B* 21 (1980) 5469-5493.
- [49] J.P. Perdew. *Physica. B* 172 (1991) 1-2.
- [50] J.P. Perdew, J.A. Chevary, S.H. Vosko, K.A. Jackson, M.R. Pederson, D.J. Singh, C. Fiolhais. *Phys. Rev. B* 46 (1992) 6671-6687.
- [51] J.P. Perdew, K. Burke, M. Ernzerhof. *Phys. Rev. Lett.* 77 (1996) 3865-3868.
- [52] J.P. Perdew, A. Ruzsinszky, J.M. Tao, V.N. Staroverov, G.E. Scuseria, G.I. Csonka. *J. Chem. Phys.* 123 (2005) 062201.
- [53] A.D. Becke. *Phys. Rev. A* 38 (1988) 3098-3100.
- [54] D.S. Sholl, J.A. Steckel. *Density Functional Theory: A Practical Introduction* (2009).
- [55] P.E. Blöchl. *Phys. Rev. B* 50 (1994) 17953-17979.
- [56] M. Marsman, G. Kresse. *J. Chem. Phys.* 125 (2006) 104101.
- [57] H. Graeme, J. Hannes. *J. Chem. Phys.* 111 (1999) 7010-7022.
- [58] G. Henkelman, B.P. Uberuaga, H. Jonsson. *J. Chem. Phys.* 113 (2000) 9901-9903.
- [59] G. Henkelman, H. Jonsson. *J. Chem. Phys.* 113 (2000) 9978-9985.
- [60] <http://cms.mpi.univie.ac.at/vasp/Welcome.html>.

CHAPTER 2

STABILITY OF EXTRAFRAMEWORK IRON-CONTAINING COMPLEXES IN ZSM-5 ZEOLITE

*The stability of isolated, oxygenated, and hydroxylated iron complexes in Fe/ZSM-5 is studied by periodic DFT calculations. The reaction paths for the interconversion of various potential iron-containing complexes confined in the zeolite matrix are discussed. It is demonstrated that Mononuclear iron(III) cations can only be stabilized at very specific exchange sites of ZSM-5 zeolite. However, the distribution of mononuclear $[\text{FeO}]^+$ species depends only slightly on the specific local zeolite environment. Nevertheless, in realistic systems the mononuclear species $[\text{FeO}]^+$ cannot be formed. Irrespective of their location inside the zeolite matrix, such species show a strong tendency towards self-organization into binuclear oxygen-bridged $[\text{Fe}(\mu\text{-O})_2\text{Fe}]^{2+}$ complexes. For all binuclear complexes considered, a notable preference for the location at the larger eight-membered ring γ -site in the sinusoidal channel is observed. Using *ab initio* thermodynamic analysis of the stability of different Fe complexes in ZSM-5 it is demonstrated that two distinct extraframework cationic complexes can be present in the Fe/ZSM-5 catalyst, namely, $[\text{Fe}^{\text{III}}(\mu\text{-O})_2\text{Fe}^{\text{III}}]^{2+}$ and $[\text{Fe}^{\text{II}}(\mu\text{-O})\text{Fe}^{\text{II}}]^{2+}$. The $[\text{Fe}^{\text{II}}(\mu\text{-O})\text{Fe}^{\text{II}}]^{2+}$ complexes containing bivalent iron centers are mainly present in the Fe/ZSM-5 catalyst activated at low oxygen chemical potential and H_2O -free conditions, whereas the formation of its Fe^{3+} -containing counterpart $[\text{Fe}^{\text{III}}(\mu\text{-O})_2\text{Fe}^{\text{III}}]^{2+}$ is favored upon the high-temperature calcination in an O_2 -rich environment.*

2.1. Introduction

ZSM-5 zeolites modified with iron (Fe/ZSM-5) demonstrate uniquely catalytic performance in several important chemical reactions such as catalytic decomposition of N_2O [1-6], selective catalytic reduction (SCR) of NO_x [7-10], oxidative dehydrogenation of alkanes [11], and direct hydroxylation of benzene to phenol and methane to methanol [12-18]. The catalytic properties and nature of iron species in Fe/ZSM-5 catalysts have been extensively studied by experimental as well as theoretical approaches [19-21]. Nowadays, it is generally accepted that the reactivity of Fe/ZSM-5 catalysts is directly related to the presence of specific extraframework iron-containing cationic species in the micropores of ZSM-5 zeolite [17, 22]. Nevertheless, the nature of the active sites for the different reactions that are catalyzed by Fe/ZSM-5 is still under debate. Identifying which particular structure is responsible for the catalytic reactions represents one of the major challenges in our understanding of the origin of the unique catalytic properties of Fe/ZSM-5.

A complicating factor in the study of Fe/ZSM-5 zeolite catalysts is the heterogeneous distribution of Fe species ranging from isolated Fe^{2+} and Fe^{3+} cations and cationic oligonuclear Fe complexes up to large agglomerates of iron oxides. The exact speciation will obviously depend on such parameters as the Fe loading, the method of iron introduction, and the history of the sample (calcination, reduction, etc.). The preferred method to introduce iron for obtaining active oxidation catalysts is to include Fe cations in the synthesis gel of ZSM-5 zeolite. In this way, Fe^{3+} ions are atomically dispersed in the final crystalline zeolite. To make these zeolites catalytically active, part of the iron is extracted from lattice positions by hydrothermal treatment, resulting in the formation of small oxygenated iron nanoclusters confined within the zeolite pores next to isolated cations [23, 24]. For instance, the formation of Fe_2O_3 , Fe_3O_4 , and Fe_4O_4 has been reported [19, 25]. Alternatively, cationic Fe complexes can also be introduced in extraframework positions of ZSM-5 zeolite by postsynthetic modification methods, such as chemical vapor deposition, solid-state ion exchange, and ion exchange in aqueous solutions. After subsequent high-temperature activation, the modified material contains a range of different iron-containing species ranging from iron oxide particles on the external surface to neutral iron oxide nanoparticles or charge-compensating cationic inside the zeolite micropores. It has been shown using in situ Raman spectroscopy that the deactivation and regeneration of active sites for catalytic N_2O decomposition in Fe/ZSM-5 prepared by solid-state ion exchange with $FeCl_3$ are directly related to the transformations of dehydroxylated binuclear Fe sites inside the zeolite voids [26-29]. The interconversion of sites active for N_2O decomposition has also been followed by high-temperature calcination and protolysis treatments [30].

The oxidation state and structural properties of the iron-containing species are influenced by the overall Fe loading in the catalyst and its activation procedure. Lobree and co-workers investigated the state of intrazeolitic iron as a function of Fe loading and the

postsynthetic thermochemical activation conditions [31]. It was shown that at exchange levels below $\text{Fe}/\text{Al} = 0.56$ Fe substitutes Brønsted acidic protons on a one-to-one basis. For $\text{Fe}/\text{Al} \leq 0.19$, most of the Fe is present as Fe^{3+} , while at higher values of Fe/Al , a mixture of Fe^{3+} and Fe^{2+} is present. Similar trends were derived from electronic paramagnetic resonance (EPR) [32] and extended X-ray absorption fine structure (EXAFS) [19] studies. Nevertheless, the nuclearity of iron in the intrazeolitic complexes is difficult to ascertain by experiment. Choi et al. reported that the structure of Fe/ZSM-5 prepared by solid-state ion exchange ($\text{Fe}/\text{Al} < 1.0$) is most adequately described as either $[\text{Fe}(\text{O})_2]^+$ or $[\text{Fe}(\text{OH})_2]^+$ [21, 33]. However, recent theoretical studies suggest that the mononuclear metal-containing complexes with terminal oxygen or hydroxyl ligand generally exhibit a strong tendency to self-organize into binuclear structures [34]. Iron loadings as high as $\text{Fe}/\text{Al} = 1$ were first reported by Sachtler and co-workers [2, 7, 8]. Subsequent EXAFS studies by Battiston et al. [35-38] and Marturano et al. [25, 39] evidenced the presence of diferric oxo/hydroxyl-bridged clusters as well as small iron oxide clusters in such a zeolite. It is very difficult to obtain a model system in this way, and mostly a very heterogeneous distribution of Fe in the zeolite is obtained [40, 41].

Also, theoretical studies have not been able to unequivocally identify the speciation of Fe in the zeolite micropores of Fe/ZSM-5. Initially, Yoshizawa et al. proposed bare Fe^+ and $[\text{FeO}]^+$ as the active site for N_2O decomposition, benzene, and methane oxidation [42, 43]. The proposal of bare Fe^+ ions in zeolites is not supported by experiment. Both mononuclear Fe^{2+} [44-46] and $[\text{FeO}]^+$ [47] and binuclear $[\text{Fe}(\mu\text{-O})\text{Fe}]^{2+}$ [48], $[\text{HOFe}(\mu\text{-O})\text{FeOH}]^{2+}$ [49], and $[\text{Fe}(\mu\text{-O})_2\text{Fe}]^{2+}$, have been considered by van Santen and co-workers. The reactivity of such complexes in the selective benzene to phenol has also been evaluated. On the other hand, Heyden and Hansen et al. also proposed several alternative mononuclear [24, 50] and binuclear [51, 52] iron-containing dehydrated and hydrated complexes as the most abundant surface species in Fe/ZSM-5. In their studies, they mainly focused on exploring the mechanism of N_2O decomposition under different reaction conditions. Benco et al. investigated the stability of isolated Fe^{2+} in ferrierite [53]. It has been reported that significant rearrangements of the zeolitic local framework due to accommodation of Fe^{2+} can only be detected from theoretical studies but not from X-ray diffraction experiments [54]. The diamond core geometry ($[\text{Fe}(\mu\text{-O})(\mu\text{-OH})\text{Fe}]^+$) has also been proposed as a potential active site by Kiwi-Minsker and co-workers [55-57]. They argued that cationic complexes with a single positive charge should dominate in zeolites with high Si/Al ratio.

To make a significant step forward in our understanding of the nature, distribution, and interconversion chemistry of Fe as cationic species in ZSM-5, we carried out a density functional theory study of mono- and binuclear oxygenated and hydroxylated iron complexes embedded in a periodic of ZSM-5. A starting point in our discussion will be how the Fe species can interconvert and how this depends on the density and distribution of Al in the zeolite framework. A thermodynamic analysis will be performed to identify the Fe speciation as a function of the pretreatment conditions of the Fe/ZSM-5 zeolite.

2.2. Computational details

All calculations were performed with the generalized gradient approximation PBE exchange and correlation functional [58] using the Vienna *ab initio* Simulation Package (VASP) [59-62]. The projected augmented waves (PAW) method was used to describe electron–ion interactions [63, 64]. Brillouin zone sampling was restricted to the Γ point. The energy cutoff was set to 400 eV. The cell parameters were optimized for the all-silica MFI orthorhombic structure (Si₉₆O₁₉₂) [65]. The parameters after optimization of volume and shape were as follows: $a = 20.119$ Å, $b = 19.767$ Å, and $c = 13.161$ Å, which are in a good agreement with the experimental X-ray diffraction (XRD) data ($a = 20.090$ Å, $b = 19.738$ Å, and $c = 13.142$ Å) [66]. Full geometry optimizations were performed with fixed optimized cell parameters using a conjugated gradient algorithm. Convergence was assumed to be reached when the forces on each atom were below 0.05 eV Å⁻¹. A modest Gaussian smearing was applied to band occupations around the Fermi level, and the total energies were extrapolated to $\sigma \rightarrow 0$. By replacing two of the 96-unit cell silicon atoms by two Al atoms, the ZSM-5 lattice with Si/Al ratio of 47 was obtained. In the case of mononuclear iron-containing species, a single-framework Al atom was introduced in the unit cell (Si/Al = 95). For multinuclear species and to study their interconversion, all of the complexes are accommodated in the eight-membered ring of the sinusoidal channel at the charge compensating sites at T7 and T12 sites or at two T11 sites in the adjacent six-membered rings of the straight channel. The structural details of the zeolite models will be more extensively discussed below. The electronic configuration of Fe²⁺ at ground-state is $S = 4/2$. Both the sextet ($S = 5/2$) and quartet ($S = 3/2$) of the mononuclear iron-oxo complex were considered, whereas we only considered the highest spin state for binuclear and multinuclear cases. Test calculations demonstrate that such configuration usually correspond to the electronic ground state of the confined binuclear complexes.

2.3. Results

2.3.1. Location and stability of isolate Fe²⁺ and [FeO]²⁺ in ZSM-5

With the goal to determine the most stable location of extraframework mononuclear Fe²⁺ and [FeO]²⁺ in the zeolite micropores, we considered a large number of models with different locations for the Al³⁺ substitutions in the zeolite framework. The α - and β - sites represent a six-membered ring (6MR) in the straight channel and a deformed 6MR at the intersection of straight and sinusoidal channels, respectively [67]. In our investigations, we additionally considered a 6MR site that is located at the intersection of the straight and sinusoidal channels (δ - site, Figure 2.1). The T atom arrangement of this δ - site differs from that of the α - site in that the bridging connection between opposite sides of the 6MR contains two T atoms in the former and one in the latter. Further sites considered are in the double five-membered rings (D5MRs), which are part of the zeolite walls. These sites have been investigated before as cation exchange sites for stabilization of Zn [68], Ga [69], and Fe [56, 57] as mononuclear exchangeable cations and also as oxygenated complexes.

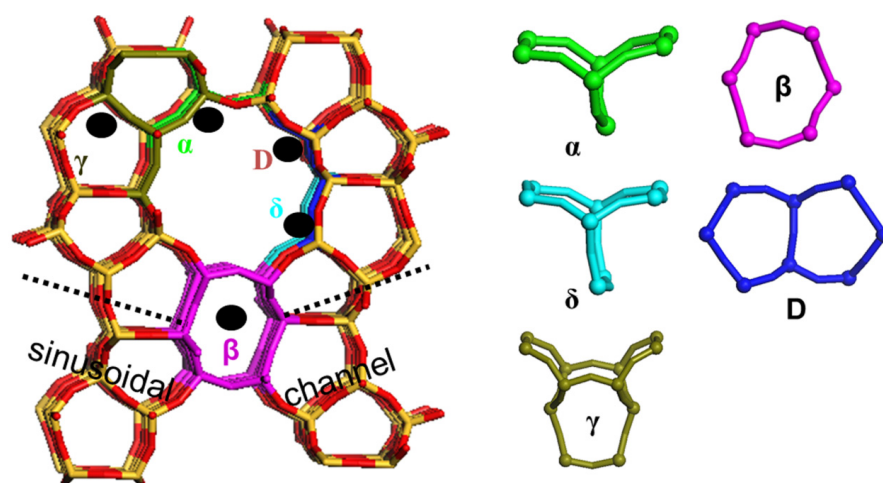


Figure 2.1. The structure of ZSM-5 zeolite and the selected cationic sites considered for the stabilization of extraframework iron-containing species.

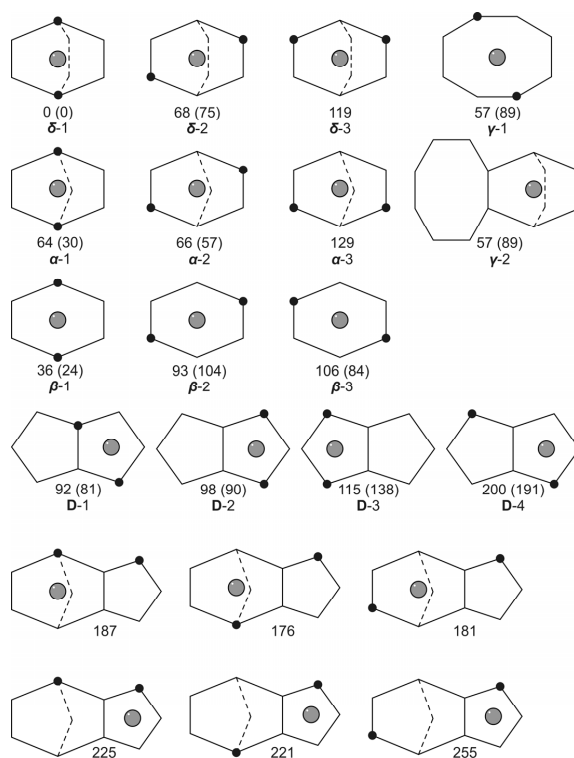


Figure 2.2. Schematic representation of different cation sites of ZSM-5 with two lattice Al atoms (black spheres) and a single Fe ion (grey sphere). Relative stability (kJ/mol) of Fe^{2+} and $[\text{FeO}]^{2+}$ (values in brackets) species are given with respect to the δ -1 configuration.

Table 2.1. Calculated Fe–O bond lengths and relative stabilities of different configurations of Fe²⁺/ZSM-5.^a

Configuration type of site	T sites of Al/Si	Fe–O bond lengths	Fe–O(avg)	Relative Stability
δ- site				
δ -1	T11,T11	2.033, 2.034, 2.034, 2.036	2.034	0
δ -2	T12,T7_diag ^c	1.926, 1.954, 2.081, 2.767	2.182	68
δ -3	T12,T7_ASA ^d	1.994, 2.019, 2.118, 2.146	2.069	119
β- site				
β -1	T4,T10	2.003, 2.019, 2.029, 2.050	2.025	36
β -2	T1,T7	2.010, 2.078, 2.188, 2.158, 2.423	2.171	93
β -3	T5, T11	1.917, 2.006, 2.170, 2.216	2,077	106
α- site				
α -1	T1,T7	2.007, 2.129, 2.132, 2.376, 2.123 ^b	2.153	64
α -2	T2,T11	2.040, 2.060, 2.117, 2.269, 2.185 ^b	2.134	66
α -3	T2,T5	1.977, 2.013, 2.165, 2.252 ^b	2.102	129
D5MR				
D-1	T3,T9	1.952, 1.977, 2.090, 2.110	2.032	92
D-2	T2,T9	1.970, 2.028, 2.035, 2.120	2.038	98
D-3	T12,T5	2.016, 2.161, 2.163, 2.331	2.168	115
D-4	T12,T9	1.932, 2.010, 2.085, 2.145	2.043	200
γ- site				
γ -1	T7,T12_Fe@8MR	2.001, 2.061, 2.073, 2.118	2.063	57
γ -2	T7,T12_Fe@6MR	1.969, 2.095, 2.143, 2.178	2.096	178
α-5MR				
	T7,T12_Fe@6MR	1.986, 2.121, 2.254, 2.120 ^b	2.265	187
	T7,T12_Fe@5MR	2.014, 2.024, 2.063, 2.158	2.065	225
	T1,T12_Fe@6MR	2.064, 2.098, 2.108, 2.498, 2.130 ^b	2.180	176
	T1,T12_Fe@5MR	2.004, 2.055, 2.062, 2.112	2.058	221
	T2,T12_Fe@6MR	2.025, 2.133, 2.219, 2.257, 2.140 ^b	2.155	181
	T2,T12_Fe@5MR	2.032, 2.049, 2.055, 2.136	2.068	255

^a Interatomic distances (<2.5 Å) are given in angstroms and relative stabilities are in kJ/mol.

^b Fe–O bond lengths between Fe²⁺ and bridging oxygen of α - site.

^c Configuration contains a chain sequence –Al–Si–Si–Al–.

^d Configuration contains a chain sequence –Al–Si–Al–.

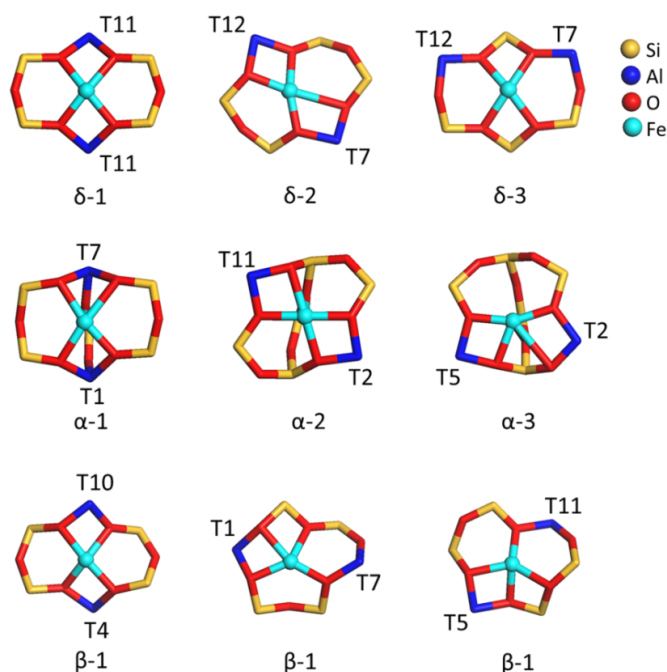


Figure 2.3. Optimized structures of Fe²⁺ stabilized at 6MR cationic sites in ZSM-5.

Finally, we included an adsorption site close to the eight-membered ring (8MR) moiety at the wall of the sinusoidal channel composed of two interconnected 5MR (γ - site). For each of these sites, we considered different configurations of the framework substitutions. Selected geometrical parameters and relative stabilities of Fe²⁺ at different local configurations of ZSM-5 are summarized in Table 2.1. The corresponding relevant portions of the optimized zeolite models containing Fe²⁺ are displayed in Figures 2.2 and 2.3.

For each of the three 6MR models three different configurations of the framework substitutions are compared. The most stable configuration is the one involving Fe²⁺ located in a δ - site (δ -1) with the framework Al atoms at two T11 positions, resulting in a symmetric distribution of the charge-compensating anionic sites over the zeolite 6MR (Figure 2.3, top panel). As a result, the ferrous ion is bonded through four equivalent bonds with the zeolite lattice. The four Fe–O_F (O_F represents framework oxygen) have similar bond lengths close to 2.034 Å. The perturbations of the zeolite lattice in this case are smaller when compared to the less stable sites.

When Fe²⁺ is located at the α - site with a similar distribution of the Al atoms, an additional bond between the cation and one of the oxygen anions below the 6MR is formed (Figure 2.3, middle panel). Despite the higher coordination number of the resulting distorted square-pyramidal configuration, this configuration is less favorable by 64 kJ/mol as compared to Fe²⁺ at the δ -1 site. The difference is due to the more substantial deformations of the zeolite framework resulting from the coordination of Fe²⁺ to the α -1

site and the lower flexibility of this portion of the zeolite lattice. As a result, the average Fe–O_F distance is approximately 0.12 Å longer compared to Fe²⁺ at the δ-1 site (Table 1).

The δ-2 and α-2 configurations involve Al substitutions at the opposite corners of the 6MRs (Figures 2.2 and 2.3). These structures exhibit comparable stabilities in the presence of Fe²⁺ to that of the α-1 configuration and likewise result in substantial local deformations of the zeolite lattice upon introduction of the cation (Table 2.1). Similar to δ-1, Fe²⁺ forms four Fe–O_F bonds at the δ-2 site, but they are not uniform. One of the Fe–O_F bonds is much longer (2.767 Å) than the others. The average Fe–O_F bond length is 0.15 Å longer compared to that in the configuration δ-1. In addition, strong local deformation of the zeolite framework is observed for both δ-2 and α-2 configurations.

The least stable of the α- and δ- site configurations involve the framework Al atoms at next-nearest positions within the 6MR (Figure 2.2 and 2.3). This is mainly caused by the coordination of Fe²⁺ to two oxygen anions of [AlO₂][−] sites instead of four in the configurations discussed above. The coordination of Fe²⁺ is completed by less basic [SiO₂] sites. For the δ-3 configuration, this results in a lower stability by 119 kJ/mol as compared to the δ-1 configuration. In this case, the deformations of the zeolite framework are minor and the average Fe–O bond length is 2.069 Å. In the α-3 configuration the strongly asymmetric location of the framework Al ions results in a decrease of the Fe–O_F coordination to four and substantial structural deformations. The energies of the α-3 and δ-3 configurations are comparable. Fe²⁺ interacts more strongly with the basic [AlO₂][−] units of the α-3 configuration, which partially compensates for the substantial energy losses due to lattice deformation.

The trends in stability of Fe²⁺ upon coordination to the β- site are similar. The most stable site is the one providing a relatively symmetric coordination environment (β-1 configuration) with the Al substitutions at T4 and T10 positions. This site is the second most stable configuration among the models considered here. It is only 36 kJ/mol less stable than the δ-1 configuration. The average Fe–O_F bond length is 2.025 Å. The β-2 and β-3 configurations result in substantial deformation of the zeolite lattice and are therefore less stable by 93 and 106 kJ/mol, respectively. The β-2 configuration with Al placed at T1 and T7 positions results in five Fe–O_F bonds that allow a slightly better stabilization of Fe²⁺ as compared to the β-3 configuration having four Fe–O_F bonds.

We have also considered the stabilization of Fe²⁺ within double five-membered ring structures of ZSM-5 (D5MR, D1-D4 configurations, Figure 2.2, Table 2.1). Four different framework Al distributions were considered. When the positive charge of the Fe²⁺ cation is compensated through a direct coordination bond with two anionic [AlO₂][−] framework sites, the relative stabilities of the resulting D-1, D-2, and D-3 configurations are 92, 98, and 115 kJ/mol, respectively (Figure 2.2). The lower stabilities of these configurations as compared to that of the 6MR sites are due to the higher rigidity of this part of the zeolite framework. The least stable configuration (200 kJ/mol) is found when one of the two

Table 2.2. Calculated Fe–O bond lengths and relative energies of $[\text{FeO}]^{2+}/\text{ZSM-5}$.^a

type of site	Configuration locations of Al	Fe–O bond lengths	Fe–O _F ^b	Fe–O _{EF} ^c	Relative Stability
δ- site					
δ -1	T11,T11	2.032, 2.034, 2.042, 2.044	2.038	1.618	0
δ -2	T12,T7_diag ^d	1.914, 1.933, 2.096	1.981	1.619	75
α- site					
α -1	T1,T7	2.018, 2.108, 2.138, 2.253, 2.137 ^e	2.131	1.629	30
α -2	T2,T11	2.076, 2.088, 2.103, 2.169, 2.236 ^e	2.134	1.623	57
β- site					
β -1	T4,T10	2.004, 2.032, 2.048, 2.057	2.035	1.629	24
β -2	T1,T7	1.990, 2.120, 2.147, 2.265, 2.462	2.197	1.619	104
β -3	T5, T11	1.996, 2.020, 2.052, 2.105	2.043	1.630	84
γ- site					
γ -1	T12, T7_Fe@8MR	1.954, 1.966, 2.095, 2.162	2.044	1.633	89
D5MRs					
D-1	T3,T9	1.957, 1.978, 2.089, 2.113	2.034	1.619	81
D-2	T2,T9	1.972, 2.034, 2.036, 2.131	2.043	1.619	90
D-3	T12,T5	1.912, 2.023, 2.053, 2.201	2.047	1.632	138
D-4	T12,T9	1.907, 2.052, 2.074, 2.139	2.043	1.620	191

^a Interatomic distances (<2.5 Å) are given in angstroms and relative stabilities are in kJ/mol.^b Average distances between the Fe center and framework O atoms.^c Fe–O bond length in the extraframework $[\text{FeO}]^{2+}$ species.^d Interatomic distance between Fe^{2+} and the framework bridging oxygen of the α - site.^e Lattice configuration contains a sequence –Al–Si–Al–.

charge-compensating $[\text{AlO}_2]^-$ lattice anions does not directly interact with the exchangeable cation (configuration D-4).

A further configuration is constructed by placing Al atoms at T7 and T12 positions within an 8MR unit. In this case, we compared two possible locations of Fe^{2+} , i.e. within the 8MR (γ -1) or in the neighboring 6MR, which is a δ - site (γ -2) (Figure 2.2). The former structure is more stable by ~ 120 kJ/mol than the γ -2 configuration. This resembles the energy differences found for different Al distributions in D5MRs. The stability of the extraframework Fe^{2+} cation critically depends on the possibility of direct charge compensation. The relative energy of the configuration γ -1 as compared to that of δ -1 is 57 kJ/mol. This is comparable to the value computed for the α -1 configuration. Thus, the 8MR site can also be considered a favorable candidate for the location of Fe^{2+} .

For completeness we considered additional Fe/ZSM-5 configurations involving the stabilization of Fe^{2+} at 5MR or 6MR with the two charge-compensating $[\text{AlO}_2]^-$ sites occupying lattice positions in adjacent zeolite rings (Figure 2.2, bottom panels). In these cases, Fe^{2+} was placed in the vicinity of one of the $[\text{AlO}_2]^-$ units, whereas the other negative framework site was located at a larger distance where it did not directly interact with the extraframework cation. The calculations predict very low stability for such configurations (Table 2.1, α -5MRs).

The hydroxylation of benzene to phenol involves the prior dissociation of nitrous oxide to produce an extraframework electrophilic oxygen atom (O_{EF}). To evaluate the role of the local zeolite environment, we computed the stability of $[\text{FeO}]^{2+}$ located at a number of favorable configurations for Fe^{2+} (δ -1, δ -2, α -1, α -2, β -1, β -2, β -3, γ -1). Despite their earlier established lower stability to accommodate Fe^{2+} , we also consider the D5MRs sites, because these sites are often employed in cluster simulations. The relative energies of the different locations of $[\text{FeO}]^{2+}$ and the corresponding optimized Fe–O bond lengths are collected in Table 2.2. Similar to Fe^{2+} , the δ -1 configuration is the most favorable location for $[\text{FeO}]^{2+}$. Configurations β -1 and α -1 result in somewhat lower stability by 24 and 30 kJ/mol, respectively, while $[\text{FeO}]^{2+}$ at D5MRs units represent the least favorable configurations.

In summary, both Fe^{2+} and $[\text{FeO}]^{2+}$ are preferentially located at the α - and δ - sites in the main channel and at the β - site at the intersection of the straight and sinusoidal channels. The most stable location of Fe^{2+} and $[\text{FeO}]^{2+}$ in ZSM-5 zeolite is the symmetric configuration formed by Fe^{2+} in the 6MR with two $[\text{AlO}_2]^-$ units at the T11 lattice positions at the intersection of the straight and sinusoidal channel. Configurations of somewhat lower stability involve the 6MR at the α - and β - sites. Fe^{2+} at the 8MR of the sinusoidal channel is moderately stable. Locations of Fe^{2+} within 5MR sites or involving indirect charge compensation are generally much less stable. The location of Fe^{2+} strongly depends on the possibility to form direct bonds between Fe^{2+} and framework oxygen atoms of the aluminum-occupied oxygen tetrahedra. The flexibility of the local framework environment is a further factor contributing to the stability of a particular configuration.

The preferred location of Fe^{2+} in δ -, α -, and β - 6MRs sites are in agreement with the experimental findings for Co^{2+} and Cu^+ ions in ZSM-5 [67, 70]. The preference for the presence of isolated Fe^{2+} at 6MR sites is in line with the previous theoretical results on the stabilities of Fe^{2+} in ferrierite, Zn^{2+} in mordenite and Cu^+ in ZSM-5 [71-73].

2.3.2. Location and stability of mononuclear $[\text{FeO}]^+$ in ZSM-5

Mononuclear $[\text{FeO}]^+$ ions containing trivalent iron are often proposed to dominate in high-silica ZSM-5 zeolites modified with iron. In general, one does not expect a preference for occupation of specific anionic exchange sites for $[\text{FeO}]^+$. To investigate the influence of the local zeolite environment on the stability of $[\text{FeO}]^+$ extraframework species and to determine their most stable locations in ZSM-5 voids, we employed a strategy similar to that employed in our previous work on Fe^{2+} sites in ZSM-5 zeolite. The stability of a series of $[\text{FeO}]^+/\text{ZSM-5}$ models differing in the location of framework Al was investigated. Here we employ the same notation for different ZSM-5 cation sites as in our previous study. The selected five distinguishable cation sites are schematically shown in Figure 2.1. Each of the sites contained a single lattice Al necessary to compensate for the positive charge of the extraframework $[\text{FeO}]^+$ species. Because our previous results indicate only a small energy difference between different spin states for the $[\text{FeO}]^+$ cations, both high ($S = 5/2$) and low spin states ($S = 3/2$) of iron were considered. Optimized local structures of selected representative examples of $[\text{FeO}]^+/\text{ZSM-5}$ together with their relative stabilities are shown in Figure 2.4. Important geometric parameters and relative stabilities of all configurations investigated are summarized in Table 2.3.

For all configurations, the $S = 5/2$ state corresponds to the electronic ground state configuration. Nevertheless, the computed energy differences between the low and high spin states are small. One can see from Table 2.3 that in the case of $S = 5/2$ the most stable configuration of $[\text{FeO}]^+$ is at the δ - site 6MR with the $[\text{AlO}_2]^-$ unit at T11. An alternative configuration $[\text{FeO}]^+$ at δ -T12 is 27 kJ/mol less stable. The coordination of $[\text{FeO}]^+$ at β - and γ - sites is only 13 and 15 kJ/mol less favorable, respectively. When Al substitutes framework Si at T1 or T7 lattice positions, the α - site can also provide favorable coordination to $[\text{FeO}]^+$. The relative energies of the corresponding configurations of $[\text{FeO}]^+$ at α -T1 and $[\text{FeO}]^+$ at α -T7 are 23 and 19 kJ/mol. The alternative Al sitting within the α site leads to much less stable structures with relative energies exceeding 50 kJ/mol as compared to the most stable δ -T11 configuration. The least stable configuration ($\Delta E^{5/2} = 66$ kJ/mol) occurs when $[\text{FeO}]^+$ coordinates at the α - site with the anionic $[\text{AlO}_2]^-$ center at the T2 lattice position. $[\text{FeO}]^+$ sitting at the smaller D site 5MR is also unfavorable ($\Delta E^{5/2} = 54$ kJ/mol). It is important to note that the energy difference between the least and most stable configurations is substantially smaller compared to the difference observed for isolated Fe^{2+} ions. This is in line with the expected lower dependency of the stability of $[\text{FeO}]^+$ on the local zeolite environment. For the most stable $[\text{FeO}]^+$ at δ -T11 configuration, the low spin state ($S = 3/2$) is 23 kJ/mol less stable than the $S = 5/2$ state. In the other cases, the energies of low spin electronic states are nearly equal to those of the high spin state. The

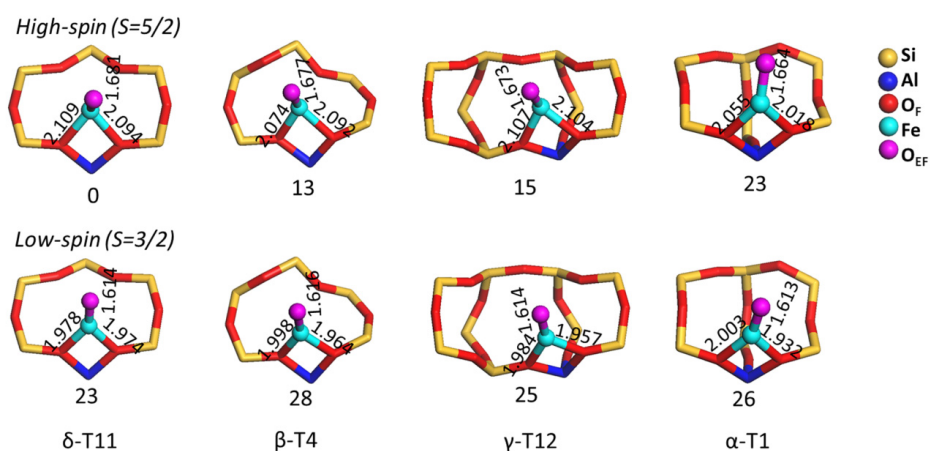


Figure 2.4. Local geometries and relative energies (kJ/mol) of $[\text{FeO}]^+$ complex stabilized at selected zeolitic cation sites (Si/Al = 95).

Table 2.3. Relative stabilities (ΔE^a , kJ mol $^{-1}$) and selected interatomic distances ($r(\text{Fe}-\text{O})$, Å) of mononuclear $[\text{FeO}]^+$ cations in different electronic configurations located at different cation sites of ZSM-5 with Si/Al ratio of 95.

Location	$S = 3/2$		$S = 5/2$		$\Delta E^{5/2}$	$\Delta E^{(S^{3/2}-S^{5/2})}$
	$\text{Fe}-\text{O}_F^b$	$\text{Fe}-\text{O}_{\text{EF}}^c$	$\text{Fe}-\text{O}_F^b$	$\text{Fe}-\text{O}_{\text{EF}}^c$		
α - site						
T1 ^d	2.003, 1.932	1.613	2.055, 2.018	1.664	23	3
T7	1.950, 1.961	1.613	2.018, 2.035	1.663	19	-1
T2	1.981, 2.046	1.611	2.204, 2.118	1.680	66	16
T5	1.980, 1.981	1.614	2.071, 2.063	1.665	52	3
T8	2.018, 1.948	1.613	2.134, 2.122	1.671	54	13
T11	1.965, 1.988	1.616	2.138, 2.080	1.665	50	-1
δ - site						
T11	1.978, 1.974	1.614	2.109, 2.094	1.681	0	23
T12	1.996, 2.016	1.614	2.232, 2.078	1.672	32	14
γ - site						
T12	1.957, 1.984	1.614	2.104, 2.107	1.673	15	10
D- site						
T12	1.964, 2.022	1.612	2.112, 2.078	1.663	54	-1
β - site						
T4	1.998, 1.964	1.616	2.074, 2.092	1.677	13	15

^a Relative stabilities for configurations of high spin state ($\Delta E^{5/2}$), and energy difference between high and low spin state ($\Delta E^{(S^{3/2}-S^{5/2})}$) for each configuration.

^b Interatomic distance between Fe and framework oxygen (O_F) atoms.

^c Interatomic distance between the extraframework iron and oxygen (O_{EF}) atoms.

^d Crystallographic lattice positions of Al substitution.

respective energy differences ($\Delta E(S^{3/2}-S^{5/2})$) are in the range of 0-30 kJ/mol (Table 2.3).

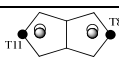
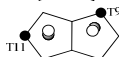
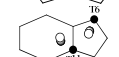
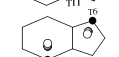
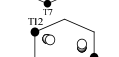
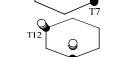

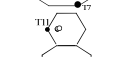
Independently from the type of anionic exchange site and spin state, Fe centers in $[\text{FeO}]^+$ form trigonal complexes with 2-fold coordination to the framework oxygen atoms (O_F) of the anionic $[\text{AlO}_2]^-$ moiety of the zeolite and one bond with the extraframework oxygen atom (O_{EF}) (Figure 2.4). The length of the $\text{Fe}-\text{O}_{\text{EF}}$ bond in the low spin state is about 1.62 Å, and that in the high spin state complexes is *ca.* 1.68 Å. The bond lengths to the framework oxygens ($\text{Fe}-\text{O}_F$) are also somewhat longer in the high spin state than in the low spin state configurations (Table 2.3). In the high spin state ($S = 5/2$), the total spin on the Fe center is $S = 4 \mu_B$, and the total spin on terminal O_{EF} is $S = 1 \mu_B$. In the case of the low-spin complexes, the spin component is localized solely on the iron center. This implies that in the $S = 5/2$ state the $[\text{FeO}]^+$ complex can be best described as the $[\text{Fe}^{2+}-\text{O}^-]^+$ species, whereas in the $S = 3/2$ state it is $[\text{Fe}^{3+}-\text{O}^{2-}]^+$ species.

In summary, $[\text{FeO}]^+$ is preferentially located at δ - site 6MR in the main channel charge compensating the $[\text{AlO}_2]^-$ unit at T11 lattice position. Configurations of somewhat lower stability involve the 6MR at β - site and 8MR at γ - site, with Al at T4 and T12 lattice positions, respectively. Locations within the α - site 6MR are also possible with Al at T1 or T7 lattice T sites. However, $[\text{FeO}]^+$ in double 5MRs (D site) are less stable. $[\text{FeO}]^+$ species in δ - site 6MR with Al at T12 position is only moderately stable. For other Al distributions within α - site 6MR the relative stabilities are notably lower than those with Al at T1 and T7 positions. We conclude that the stability of $[\text{FeO}]^+$ species in ZSM-5 only slightly depends on the local framework configurations of zeolite and the distribution of lattice Al ions.

2.3.3. Self-organization of $[\text{FeO}]^+$ and stability of binuclear $[\text{Fe}_2\text{O}_2]^{2+}$ sites

Table 2.4 lists the stabilities of two $[\text{FeO}]^+$ ions coexisting within a single ZSM-5 unit cell with a Si/Al ratio of 47. Similar to the case of the isolated $[\text{FeO}]^+$, the stability of two $[\text{FeO}]^+$ ions is only slightly influenced by the structural details of the local zeolite environment. The coordination of two $[\text{FeO}]^+$ within a double 5MR site leads to the least stable configuration, which is only 69 kJ/mol less favorable than the stabilization of two isolated mononuclear cations within the γ - site containing two lattice Al ions. Note that such species may undergo self-organization into binuclear complexes driven by the excessive basicity of the terminal oxygen ligands and the Lewis acidity of the cationic centers. As a result, oxygen-bridged structures can be formed with chemical properties and catalytic reactivity different from their mononuclear counterparts. Figure 2.5 shows three selected ZSM-5 models containing binuclear $[\text{FeO}]_2^{2+}$ structures with a distinctly different distribution of framework Al. In model I, the Al ions are placed at T8 and T11 crystallographic sites in the double 5MRs located within the straight channel. In the case of model II, two Al atoms are placed at the T6 site of the 5MR and T7 site of the adjacent 6MR of the straight channel. The Al atoms in model III are located in the T7 and T12 sites of the 8MR within the sinusoidal channel. The distance between two Al atoms is 8.18 Å, 7.46 Å, and 8.42 Å, respectively, for models I, II, and III.

Table 2.4. Relative stabilities (kJ/mol) of two $[\text{FeO}]^+$ complexes and the products of their self-organization into binuclear species in ZSM-5 (Si/Al = 47). $E1$ and $E2$ (kJ/mol) correspond to the reaction energies of: $2x[\text{FeO}]^+ \rightarrow [\text{FeOFeO}]^{2+}$ and $[\text{OFe}(\mu\text{-O})\text{Fe}]^{2+} \rightarrow [\text{Fe}(\mu\text{-O})_2\text{Fe}]^{2+}$. Black spheres: Al atoms, light grey and white spheres: Fe and O_F atoms.

Locations	Relative stabilities			Reaction energy		$r(\text{Al-Al})$ /Å
	$2x[\text{FeO}]^+$	$[\text{OFe}(\mu\text{-O})\text{Fe}]^{2+}$	$[\text{Fe}(\mu\text{-O})_2\text{Fe}]^{2+}$	$E1$	$E2$	
	39	124	56	-105	-101	8.181
	69	90	121	-169	-3	7.464
	—	55	64	—	-24	4.748
	33	101	55	-122	-79	7.457
	—	62	79	—	-16	6.566
	—	28	29	—	-32	5.057
	0	0	0	-190	-33	5.432
	16	98	102	-107	-29	8.422

Initially, noninteracting $[\text{FeO}]^+$ species have geometries similar to those observed for the isolated ions discussed in the previous section. For all three models, the self-organization of the mononuclear $[\text{FeO}]^+$ into dimeric $[\text{OFe}(\mu\text{-O})\text{Fe}]^{2+}$ is strongly favored. The calculated reaction energies for the assembly process equal -105, -122, and -107 kJ/mol, respectively, for models I, II, and III. The structural details of the resulting binuclear $[\text{OFe}(\mu\text{-O})\text{Fe}]^{2+}$ species strongly depend on the position within the zeolite (Figure 2.5). In the case of model I, after the aggregation, one of the two iron centers is 4-fold coordinated with three O_F atoms (two of them are from negative charge compensating $[\text{AlO}_2]^-$ site and one from a vicinal neutral $[\text{SiO}_2]$ site, $r(\text{Fe}-\text{O}_\text{F}) = 2.03\text{-}2.24$ Å) and with one bridged O_EF ($r(\text{Fe}-\text{O}_\text{EF}) = 1.82$ Å). The other Fe is 3-fold coordinated with one framework anionic oxygen ($r(\text{Fe}-\text{O}_\text{F}) = 1.94$ Å), one bridged O_EF ($r(\text{Fe}-\text{O}_\text{EF}) = 1.72$ Å), and one terminal oxygen ligand ($r(\text{Fe}-\text{O}_\text{EF}) = 1.60$ Å). For model II, both iron centers are 3-fold coordinated. One of them is bound to two negatively charged O_F atoms and one bridged O_EF atom, and the other one is coordinated by one anionic O_F and two O_EF atoms. The complex is characterized by $\text{Fe}-\text{O}_\text{F}$ distances of 1.94-2.06 Å and by a notably shorter bond between the bridged oxygen and iron centers ($r(\text{Fe}-\text{O}_\text{EF}) = 1.76$ Å). The distance between the iron and the terminal oxygen ligand equals 1.63 Å. In model III, each iron center coordinates two O_F atoms ($r(\text{Fe}-\text{O}_\text{F}) = 1.97\text{-}2.13$ Å) and they share the bridged O_EF with each other ($r(\text{Fe}-\text{O}_\text{EF}) = 1.78$ Å). The bond length between Fe and the terminal oxygen is 1.63 Å. Only one of the iron centers is directly stabilized by the charge-compensating lattice Al site. The other one coordinates to the neutral silicon-occupied oxygen tetrahedron, while the anionic $[\text{AlO}_2]^-$ lattice moiety is

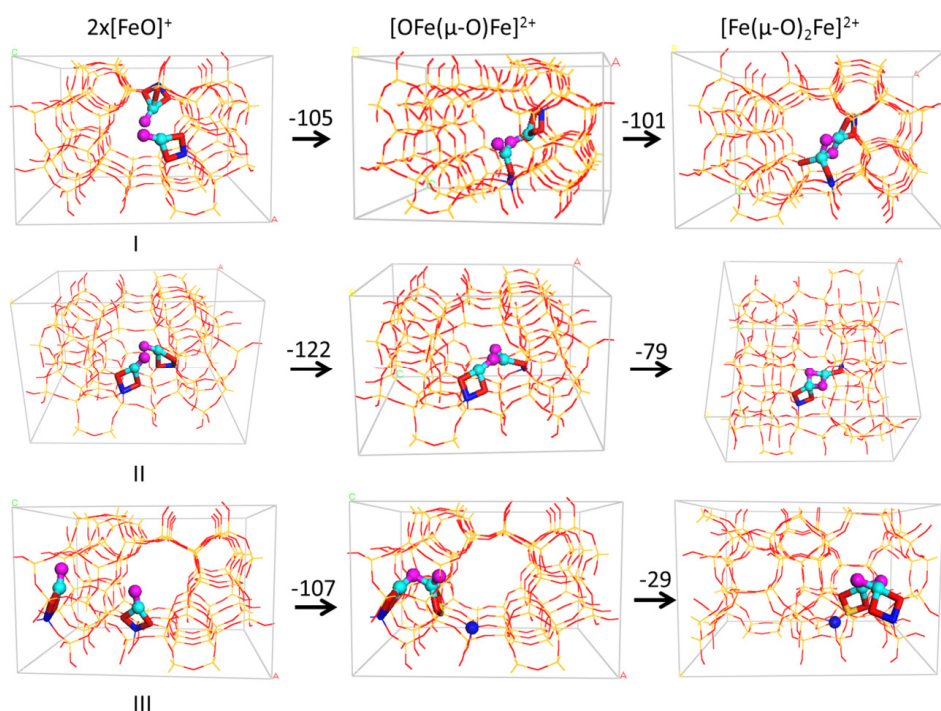


Figure 2.5. Self-organization of $[\text{FeO}]^+$ cations in MFI zeolite (Si/Al = 47). The numbers above the arrows are reaction energies (kJ/mol) of the corresponding transformation.

located in adjacent δ - site 6MR. Despite the lack of a counterion in the first coordination sphere of the metal center, the calculated reaction energy for the self-organization of $[\text{FeO}]^+$ in model III is comparable to the reaction energies for models I and II.

Further stabilization of the extraframework species is achieved by the formation of the $[\text{Fe}(\mu\text{-O})_2\text{Fe}]^{2+}$ cation. This additionally lowers the total energies by -101, -79, and -29 kJ/mol for models I, II, and III, respectively. This process is associated with the formation of an almost perfect tetrahedral environment of both iron centers. In model I, the $[\text{Fe}(\mu\text{-O})_2\text{Fe}]^{2+}$ complex has a perfect square-planar shape. Compared to this, the geometry of the $[\text{Fe}(\mu\text{-O})_2\text{Fe}]^{2+}$ complex in model II is slightly distorted. For model III, the positions of the O_{EF} atoms substantially deviate from the plane of the complex, and the extraframework cation has a strongly distorted boat shape. The low exothermicity of the formation of $[\text{Fe}(\mu\text{-O})_2\text{Fe}]^{2+}$ and its strong geometrical distortions when stabilized in model III are due to the presence of a single negative compensated site in the first coordination sphere of the cationic species and the resulting rather unfavorable indirect charge compensation of the extraframework cationic complex with the second distant lattice anionic center. In all three cases, the $\text{Fe}-\text{O}_{\text{F}}$ distances are in the range of 1.99-2.24 Å, while the $\text{Fe}-\text{O}_{\text{EF}}$ bond lengths are equal to 1.72-1.92 Å.

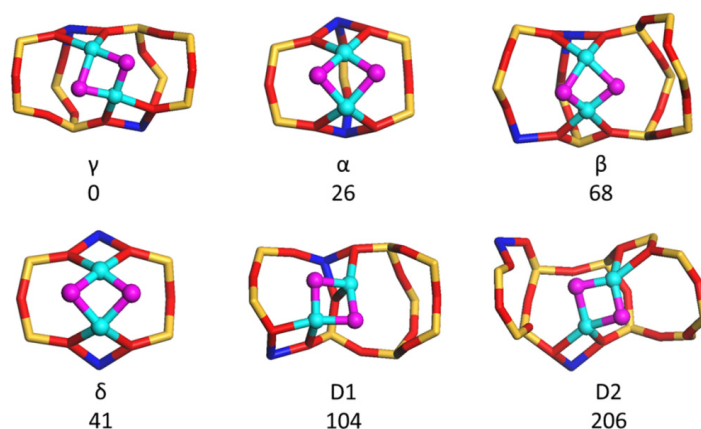


Figure 2.6. Local optimized geometries and relative energies (kJ/mol) of the $[\text{Fe}(\mu\text{-O})_2\text{Fe}]^{2+}$ binuclear complex stabilized at different cation sites of ZSM-5 (Si/Al = 47).

Table 2.5. Relative stabilities (ΔE , kJ/mol) and selected optimized interatomic distances (r , Å) for $[\text{Fe}(\mu\text{-O})_2\text{Fe}]^{2+}$ extraframework species located at different cation sites of ZSM-5 zeolite (Si/Al = 47).

Locations	$r(\text{Fe-O}_F)$	$r(\text{Fe-O}_{\text{EF}})$	$r(\text{Fe-Fe})$	ΔE
γ	2.051, 2.075, 2.003, 1.996	1.722, 1.782, 1.853, 1.956	2.384	0
α	1.973, 1.973, 2.043, 2.130	1.737, 1.762, 1.888, 1.957	2.370	26
δ	1.987, 1.990, 2.082, 2.086	1.746, 1.750, 1.912, 1.918	2.328	41
β	1.987, 1.990, 2.082, 2.086	1.746, 1.750, 1.912, 1.918	2.441	68
D1	2.048, 2.084, 2.084, 2.120	1.769, 1.806, 1.826, 1.857	2.323	104
D2	2.046, 2.103, 2.167, 2.196	1.705, 1.743, 1.914, 1.946	2.561	206

A number of alternative dual-site $[\text{FeO}]^+$ configurations were also considered. The relative stabilities of different models considered are summarized in Table 2.4. One can see that for all investigated configurations the self-organization of isolated $[\text{FeO}]^+$ species is always strongly favored thermodynamically. When the distance between the lattice Al atoms is below 6.57 Å, the isolated $[\text{FeO}]^+$ spontaneously self-organizes into binuclear $[\text{OFe}(\mu\text{-O})\text{Fe}]^{2+}$ clusters already upon the geometry optimization. For both isolated dual $[\text{FeO}]^+$ and binuclear complexes, the most favorable location is the γ - site with two framework Al atoms at T7 and T12 lattice sites. We also investigated the possibility of the formation of alternative $\mu\text{-}(\eta^2\text{:}\eta^2)\text{-peroxo}$ or $\mu\text{-}1,2\text{-peroxo}$ diiron cations. It is found that such structures are much less stable than the bis($\mu\text{-oxo}$) diiron cations discussed above. The $[\text{Fe}(\mu\text{-O})_2\text{Fe}]^{2+}$ configuration is always preferred thermodynamically.

Figure 2.6 shows local structures of the representative $[\text{Fe}(\mu\text{-O})_2\text{Fe}]^{2+}$ complex stabilized at selected cation sites of ZSM-5. In all configurations, the iron centers adopt a distorted square-planar coordination environment. The preferred location of the binuclear complex is the γ - site. The stabilization of the $[\text{Fe}(\mu\text{-O})_2\text{Fe}]^{2+}$ cation at the α - site is less favorable by 26 kJ/mol, while that at the δ - site is by 41 kJ/mol less stable than in the most stable

configuration. Due to the limited space available at the β - site for the accommodation of a rather bulky $[\text{Fe}(\mu\text{-O})_2\text{Fe}]^{2+}$ cation, two of the four Fe-O_F coordination bonds are formed with the anionic O_F atoms from the neighboring β - site. The relative stability of such a configuration is 68 kJ/mol. The coordination of $[\text{Fe}(\mu\text{-O})_2\text{Fe}]^{2+}$ at the D1 site is 104 kJ/mol less favorable than that at the γ - site, despite the presence of two $[\text{AlO}_2]^-$ units within a single zeolite ring. When two $[\text{AlO}_2]^-$ units are located in different 5MRs (D2 site), the binuclear site can interact directly with one of them. One of the two iron atoms is coordinated to a neutral framework $[\text{SiO}_2]$ unit from the neighboring 6MR. Thus, D2 site is the least stable position for $[\text{Fe}(\mu\text{-O})_2\text{Fe}]^{2+}$. The Fe-O_F bond length in all configurations ranges from 1.97 to 2.20 Å, and the Fe-O_{EF} distances range from 1.70 to 1.96 Å. The optimized interatomic distances for the structures considered are collected in Table 2.5.

These findings demonstrate the importance of the formation of a favorable coordination environment for the stability of extraframework cations in high-silica zeolites. Mononuclear oxygenated cationic Fe complexes in high-silica zeolites tend to self-organize into binuclear complexes. Similar findings have been previously reported by us for zeolites modified with Ga, Zn, Al, and Cu [34, 74, 75]. Thus, the process of self-organization is a general phenomenon. It is driven by the stabilization of undercoordinated metal centers and excessively basic terminal oxygen ligands via the formation of oxygen-bridged complexes. In some cases, the presence of multiple-charged binuclear oxygenated metal complexes in zeolites does not necessarily require the immediate proximity of an equivalent number of negative framework charges.

2.3.4. Stability of binuclear $[\text{Fe}^{\text{II}}(\mu\text{-O})\text{Fe}^{\text{II}}]^{2+}$ in ZSM-5

Previously, alternative Fe(II)-containing oxygen-bridged binuclear $[\text{Fe}(\mu\text{-O})\text{Fe}]^{2+}$ complexes have been widely proposed as the sites responsible for the high catalytic activity of Fe/ZSM-5 in the deNO_x process [26, 48, 51]. Therefore, the stability of this complex has also been investigated in this study. Figure 2.7 displays the local optimized structures of $[\text{Fe}(\mu\text{-O})\text{Fe}]^{2+}$ complexes located at six different cation sites of ZSM-5. In all configurations, both iron centers are 3-fold coordinated by two O_F atoms and bridged by a single O_{EF} atom. An exceptional situation occurs, however, for the D1 site, in which one of the two Fe is bound to O_F atoms from the adjacent 6MR. The coordination of the binuclear complex to the γ - site represents the most stable configuration when lattice Al ions are present at the T7 and T12 positions. The α , β , and δ configurations are less stable than γ by about 20 kJ/mol. The least efficient stabilization of the $[\text{Fe}(\mu\text{-O})\text{Fe}]^{2+}$ complex occurs by location at the double 5MR sites (D1 and D2 sites). The relative stabilities of these two configurations are 93 and 132 kJ/mol, respectively. Depending on the zeolite model, the coordination of the iron centers with the lattice (Fe-O_F) ranges from 1.99 to 2.506 Å, while the bonding between Fe and O_{EF} atoms is rather uniform for all configurations. The respective $r(\text{Fe-O}_{EF})$ equals 1.79-1.80 Å (Table 2.6).

Similar to other binuclear clusters, the preferred location of the binuclear cluster is the γ -site with Al substitutions at T7 and T12 positions. The coordination of these species at the

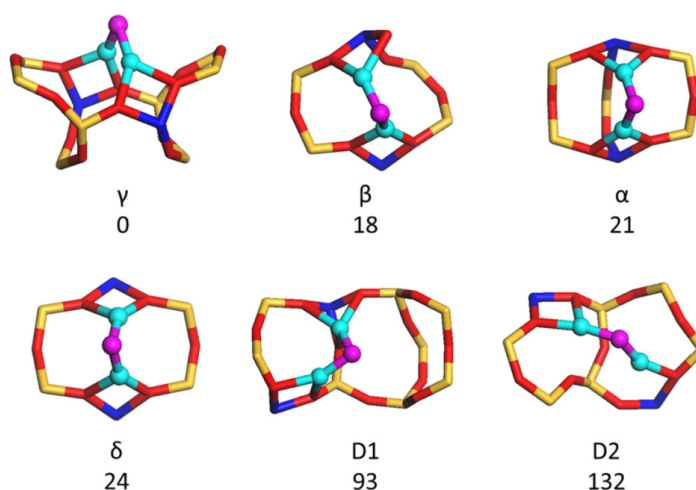


Figure 2.7. Local optimized geometries and relative energies (kJ/mol) of the $[\text{Fe}(\mu\text{-O})\text{Fe}]^{2+}$ complexes stabilized at different cation sites in ZSM-5 (Si/Al = 47).

Table 2.6. Relative stabilities (ΔE , kJ/mol) and selected optimized interatomic distances (r , Å) for $[\text{Fe}(\mu\text{-O})\text{Fe}]^{2+}$ extraframework species located at different cation sites of ZSM-5 zeolite (Si/Al = 47).

Locations	Fe–O _F	Fe–O _{EF}	Fe–Fe	ΔE
γ	2.018, 2.058, 2.244, 2.506	1.794, 1.795	2.447	0
β	2.018, 2.041, 2.073, 2.084	1.791, 1.800	2.403	18
α	1.989, 1.991, 2.056, 2.098	1.793, 1.798	2.395	21
δ	2.007, 2.009, 2.070, 2.076,	1.799, 1.799	2.337	24
D1	2.068, 2.098, 2.188, 2.194, 2.281	1.794, 1.807	2.415	93
D2	1.968, 2.026, 2.274, 2.444	1.791, 1.804	3.011	132

alternative α -, β -, and δ - sites is only slightly less favorable, suggesting that all of them can efficiently stabilize the $[\text{Fe}(\mu\text{-O})\text{Fe}]^{2+}$ species. The location of the cationic complexes at the double 5MRs located within the straight channel of ZSM-5 is much less favorable, probably because of the lower flexibility of the respective zeolitic cation sites.

2.3.5. Interconversion of different iron containing sites in ZSM-5

The computational results presented so far demonstrate that the mononuclear oxygenated iron species tend to self-organize into binuclear complexes. Nevertheless, a range of different multinuclear species can potentially be present in the zeolite, and the question of the dominant iron-containing complexes in the activated Fe/ZSM-5 catalyst remains open. To address this question, we performed a systematic thermodynamic analysis of the interconversion of different iron-containing species confined in the pores of ZSM-5.

As a starting point, we selected a neutral cubane type cluster $[\text{Fe}_4\text{O}_6]$ stabilized in ZSM-5 voids (Figure 2.8). The nanocluster contains two 3-fold coordinated and two 4-fold

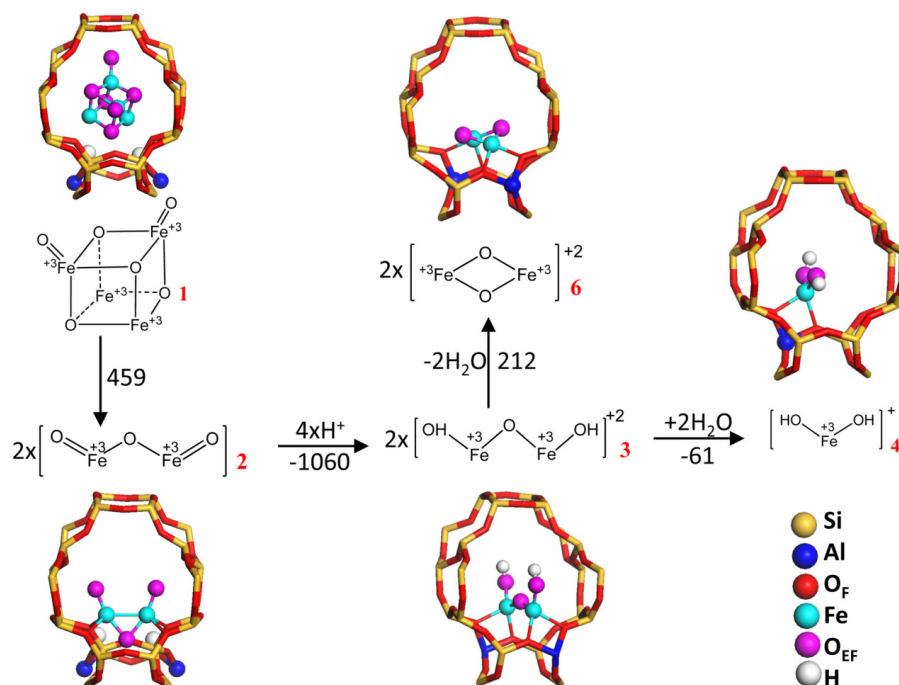


Figure 2.8. Direct decomposition of confined $[\text{Fe}^{\text{III}}_4\text{O}_6]$ iron oxide cluster and the optimized structures of the involved potential intermediate complexes. Reaction energies are given in kJ/mol.

coordinated Fe(III) ions and is stabilized in the sinusoidal channel at the 8MR site adjacent to the straight channel. In the starting model, two Al ions are placed at the T11 lattice positions, adjacent to the δ - site 6MR. The resulting negative charge is compensated by protons giving rise to two Brønsted acid sites at the δ - site.

The direct decomposition of the neutral nanocluster can lead to the formation of two neutral $[\text{OFe}(\mu\text{-O})\text{FeO}]$ binuclear complexes. This proposed reaction is thermodynamically strongly unfavorable ($\Delta E = 459$ kJ/mol) and will, therefore, only take place at very high temperatures. However, once this step occurs, the subsequent protonation of $[\text{OFe}(\mu\text{-O})\text{FeO}]$ by zeolitic Brønsted sites is strongly exothermic (-530 kJ/mol per site) and leads to the formation of the hydroxylated $[\text{HOFe}(\mu\text{-O})\text{FeOH}]^{2+}$ species charge-compensated by two anionic $[\text{AlO}_2]^-$ lattice sites. Such structures have previously been proposed for Fe/ZSM-5 at low temperature in the presence of water [28, 49, 52]. This hydroxylated complex can be further hydrolyzed upon reaction with H_2O resulting in two $[\text{Fe}(\text{OH})_2]^+$ species. This step is endothermic ($\Delta E = 30$ kJ/mol per binuclear site). Alternatively, $[\text{HOFe}(\mu\text{-O})\text{FeOH}]^{2+}$ can be dehydrated resulting in the binuclear $[\text{Fe}(\mu\text{-O})_2\text{Fe}]$ species. Because this process is associated with a substantial distortion of the

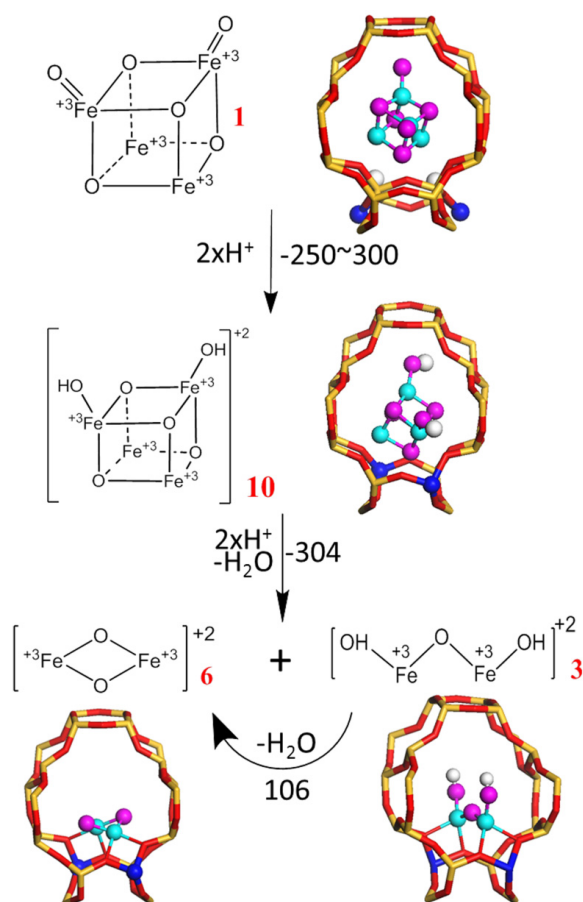


Figure 2.9. Proton-assisted transformations of $[\text{Fe}^{\text{III}}_4\text{O}_6]$ iron oxide precursor in ZSM-5 zeolite. Reaction energies are given in kJ/mol.

favorable coordination environment, it is thermodynamically unfavorable ($\Delta E = 106$ kJ/mol).

Besides the direct decomposition, the initial $[\text{Fe}_4\text{O}_6]$ nanocluster can also be protonated by zeolitic Brønsted acid sites. The corresponding chemical transformations and associated reaction energies are summarized in Figure 2.9. The initial protonation step is strongly exothermic ($\Delta E = -250$ kJ/mol) and involves the protonation of the terminal oxo ligands resulting in the cationic $[\text{Fe}_4\text{O}_4(\text{OH})_2]^{2+}$ cluster. This species can then undergo a proton-assisted decomposition and dehydration reactions resulting in binuclear $[\text{HOFe}(\mu\text{-O})\text{FeOH}]^{2+}$ and $[\text{Fe}(\mu\text{-O})_2\text{Fe}]^{2+}$ complexes ($\Delta E = -304$ kJ/mol), which can be interconverted by release or uptake of a water molecule.

One should note that the reaction paths considered so far do not involve the change of the oxidation state of Fe centers, which remain in their original +3 state. However, at high

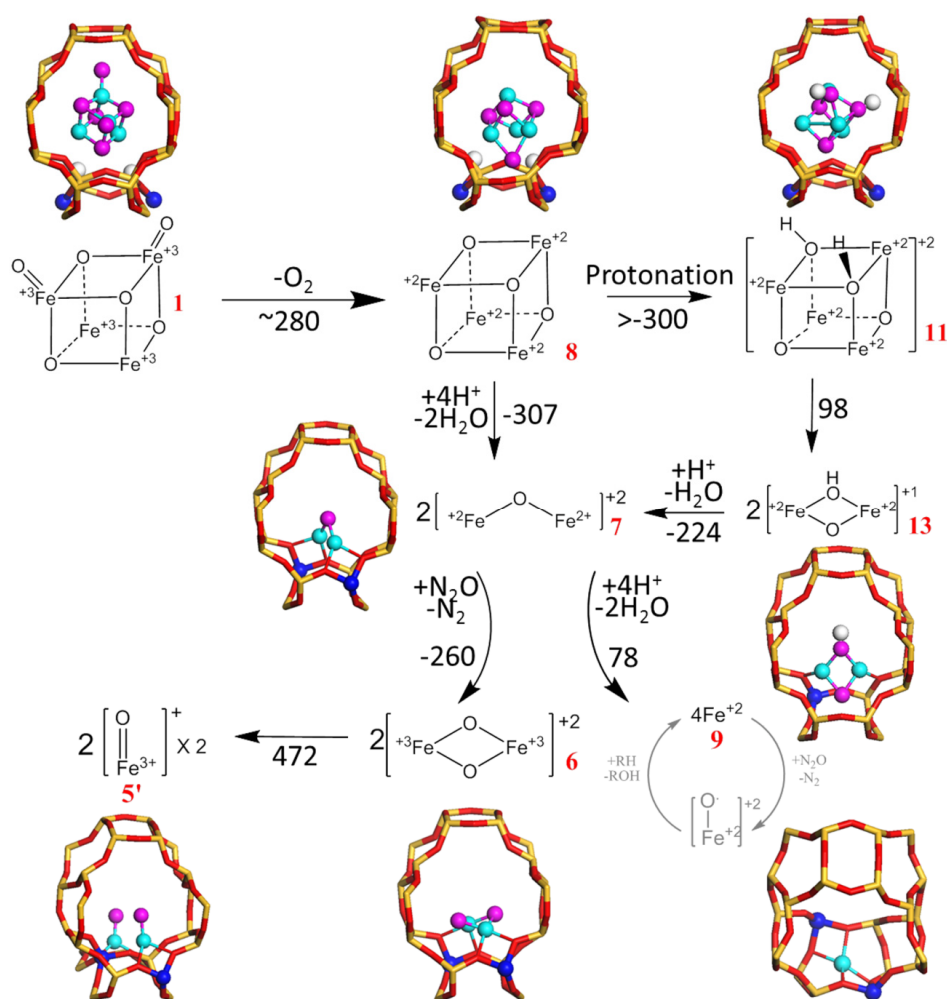


Figure 2.10. Autoreduction and subsequent transformations of $[\text{Fe}^{\text{III}}_4\text{O}_6]$ iron oxide cluster in ZSM-5 zeolite. Reaction energies are given in kJ/mol.

temperature, oxygenated iron clusters can autoreduce, resulting in the formation of Fe^{2+} -containing species. Figure 2.10 shows the reaction paths involving the autoreduction of the neutral cubic $[\text{Fe}^{\text{III}}_4\text{O}_6]$ nanoclusters to the $[\text{Fe}^{\text{II}}_4\text{O}_4]$ complex at the initial stage of the reaction. This process is strongly endothermic, and the reaction energy is around 280 kJ/mol. Note that this reaction will be entropy driven by the release of O_2 . It is preferred at high temperature. The reduced $[\text{Fe}^{\text{II}}_4\text{O}_4]$ complex can either be protonated resulting in $[\text{Fe}_4\text{O}_2(\text{OH})_2]^{2+}$ cationic species ($\Delta E > -300$ kJ/mol) or undergo a proton-assisted decomposition and dehydration toward binuclear $[\text{Fe}(\mu\text{-O})\text{Fe}]^{2+}$ ($\Delta E = -307$ kJ/mol). The former path leads to formation of two $[\text{Fe}(\mu\text{-O})(\mu\text{-OH})\text{Fe}]^+$ complexes with a moderate reaction energy ($\Delta E = 98$ kJ/mol). $[\text{Fe}(\mu\text{-O})(\mu\text{-OH})\text{Fe}]^+$ has been proposed as the active site for N_2O decomposition by Kiwi-Minsker and co-workers [76]. It has been assumed that

such species are formed predominantly at the cationic sites containing isolated lattice Al sites. When a second anionic center is available in the vicinity of this hydro-oxo cation, it can be protonated resulting in the elimination of water and formation of the more stable $[\text{Fe}(\mu\text{-O})\text{Fe}]^{2+}$ complex ($\Delta E = -112$ kJ/mol per species). This scheme suggests that the $[\text{Fe}(\mu\text{-O})\text{Fe}]^{2+}$ binuclear cations dominate in Fe/ZSM-5 catalysts activated at high temperature.

The isolated Fe^{2+} active site can be obtained by further decomposition of the binuclear $[\text{Fe}(\mu\text{-O})\text{Fe}]^{2+}$ species. Isolated Fe^{2+} has been widely proposed to be responsible for the generation of α -oxygen upon decomposition of nitrous oxide and subsequent oxidation of hydrocarbon molecules. However, the concentration of such sites is usually very low. The calculated reaction energy for the decomposition of $[\text{Fe}(\mu\text{-O})\text{Fe}]^{2+}$ to two Fe^{2+} and H_2O involving two additional zeolitic protons is only slightly positive ($\Delta E = 78$ kJ/mol), when the coordination of Fe^{2+} is considered for the specific γ - site. Nevertheless, one should note that such a process requires the presence of four proximate and optimally arranged lattice Al ions. It may be expected that such centers are very minor in ZSM-5, which may explain the relatively low concentration of isolated Fe^{2+} ions in Fe/ZSM-5.

The Fe^{2+} and Fe^{3+} -containing intrazeolitic complexes can be interconverted by the reaction of $[\text{Fe}(\mu\text{-O})\text{Fe}]^{2+}$ with N_2O . This oxidation process is exothermic and leads to $[\text{Fe}(\mu\text{-O})_2\text{Fe}]^{2+}$. We propose that this interconversion plays a key role in the catalytic N_2O decomposition reaction. Further decomposition of the binuclear $[\text{Fe}(\mu\text{-O})_2\text{Fe}]^{2+}$ site into mononuclear oxygenated iron complexes is strongly unfavorable ($\Delta E = 236$ kJ/mol per binuclear site).

The stability of the initial neutral $[\text{Fe}^{\text{III}}_4\text{O}_6]$ and $[\text{Fe}^{\text{II}}_4\text{O}_4]$ depends only slightly on the local zeolite environment. As shown in Figure 2.11, both clusters can be stabilized within the sinusoidal or straight channels of ZSM-5 zeolite with Brønsted acid sites sufficiently separated from the oxidic clusters. The energy differences between these different configurations are negligible. For $[\text{Fe}^{\text{III}}_4\text{O}_6]$, the location in the straight channel is 24 kJ/mol more stable than that in the sinusoidal γ - site. After oxidation, the mobility of the $[\text{Fe}^{\text{II}}_4\text{O}_4]$ complex increases. In this case the preference for the stabilization at the γ - site is only 7 kJ/mol. We expect that these clusters are readily protonated when they are close to zeolitic Brønsted acid sites. The resulting cationic species (i.e., $[\text{Fe}^{\text{III}}_4\text{O}_4(\text{OH})_2]^{2+}$ and $[\text{Fe}^{\text{II}}_4\text{O}_2(\text{OH})_2]^{2+}$) are particularly sensitive to the location of lattice anions and the type of the stabilizing zeolite site. Figure 2.12 shows that the intermediate $[\text{Fe}^{\text{III}}_4\text{O}_4(\text{OH})_2]^{2+}$ species can be only efficiently stabilized at the γ - site containing two Al centers. The stability of the charge-alternating structures formed when the two Al sites are placed within the δ - site 6MR is 190 kJ/mol lower. A similar situation is realized in the case of the $[\text{Fe}^{\text{II}}_4\text{O}_2(\text{OH})_2]^{2+}$ cationic complex, for which the stabilization at the γ - site is 100 kJ/mol more favorable than within the alternative charge-alternating configuration. Furthermore, in this case the stability of the cationic hydroxylated cluster is strongly influenced by its relative orientation within the zeolite pore. The ability of the cluster to form hydrogen

Stability of extraframework iron-containing complexes in ZSM-5 zeolite

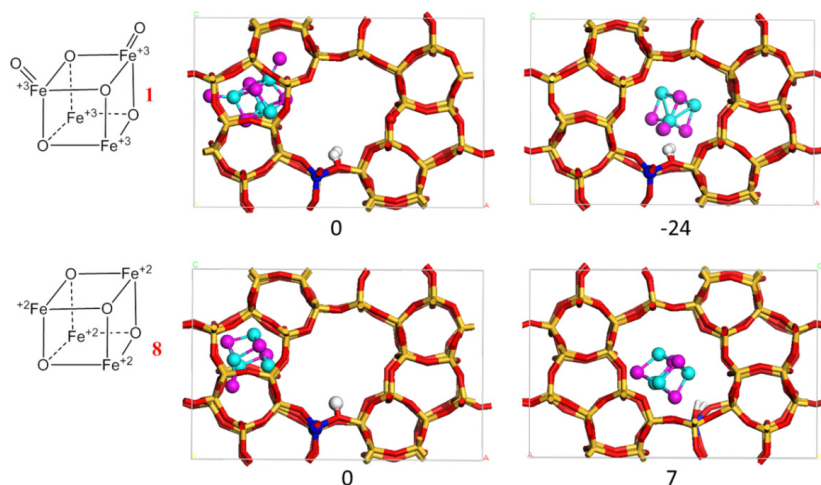


Figure 2.11. Influence of local zeolite environment on the relative stability of neutral cubic $[\text{Fe}^{\text{III}}_4\text{O}_6]$ and $[\text{Fe}^{\text{II}}_4\text{O}_4]$ iron oxide precursors within ZSM-5 pores. The protons and the associated two framework Al atoms are located within the δ site 6MR. All energies are given in kJ/mo.

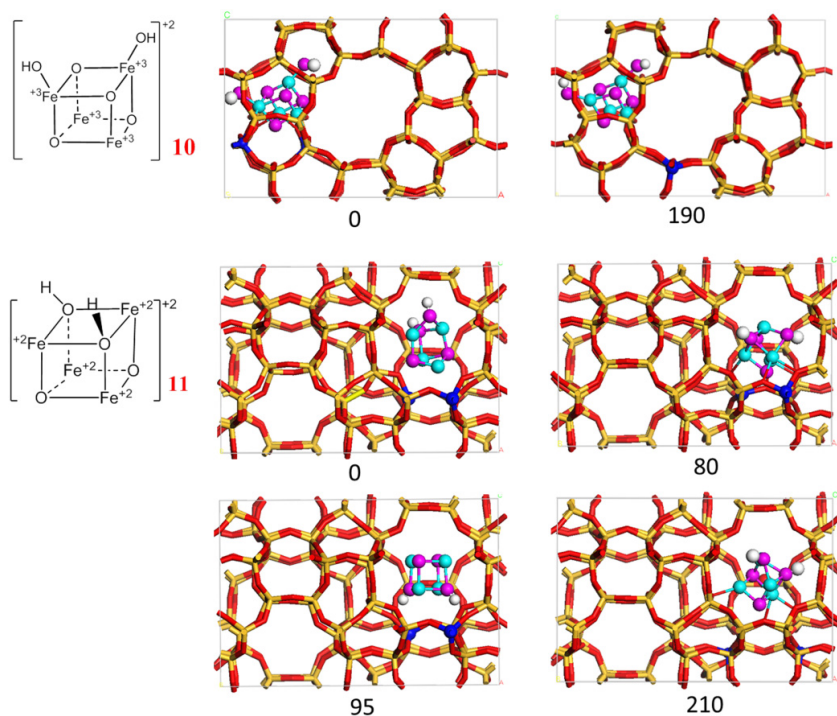


Figure 2.12. Influence of local zeolite environment on the relative stability of protonated cationic $[\text{Fe}^{\text{III}}_4\text{O}_4(\text{OH})_2]$ and $[\text{Fe}_4\text{O}_2(\text{OH})_2]^{2+}$ clusters in ZSM-5. All energies are given in kJ/mol.

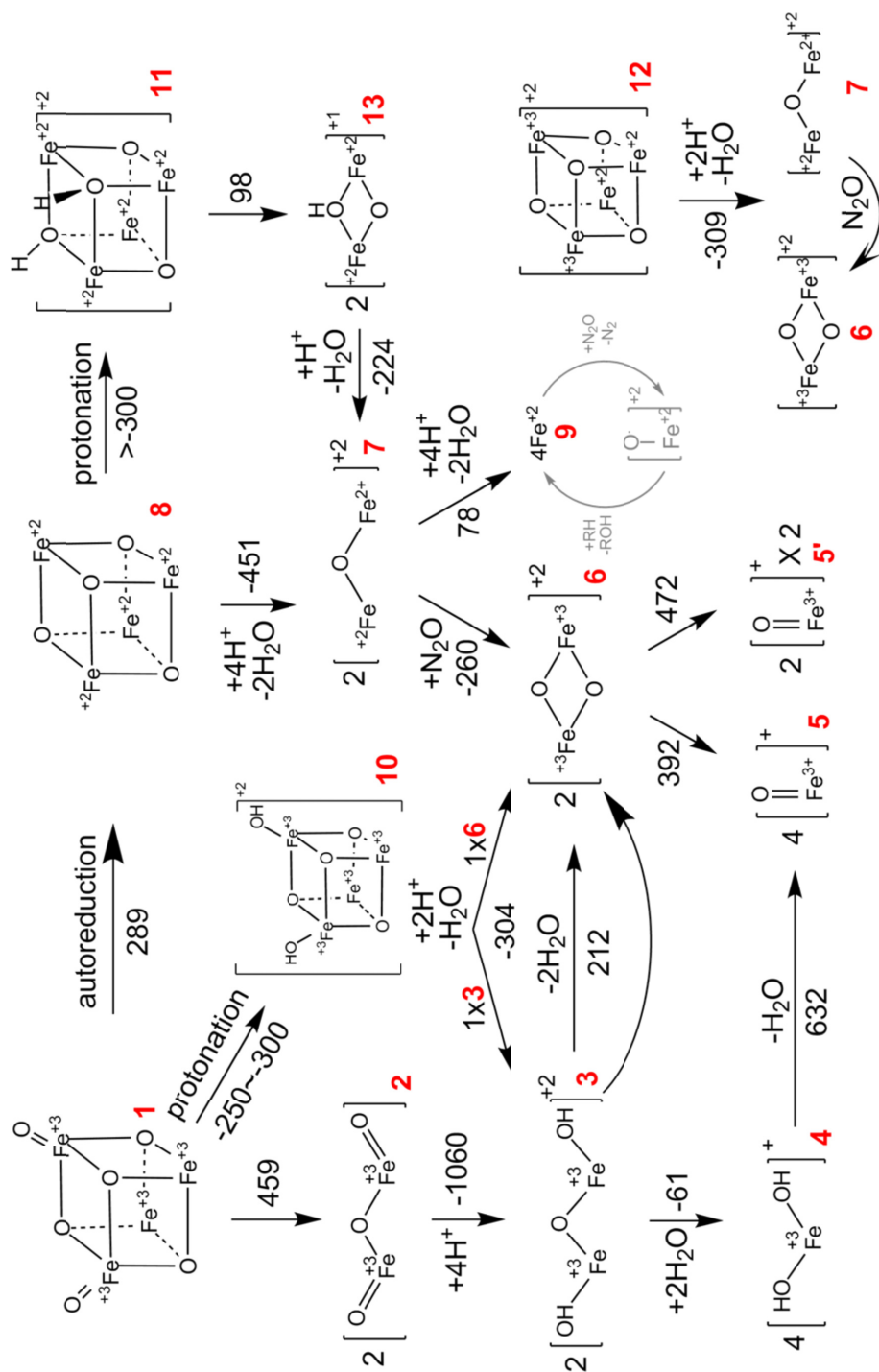


Figure 2.13. Reaction paths for interconversion of iron-containing complexes confined in ZSM-5 zeolite. Reaction energies are given in kJ/mol.

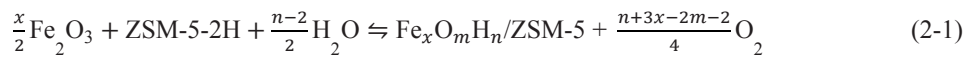
bonds between the terminal OH groups and the zeolite lattice alters its relative stability by up to 95 kJ/mol.

Thus, several possible interconversion paths for the iron-containing species in ZSM-5 zeolite can be proposed based on the present results of DFT calculations. The reactions involve Brønsted acid sites, water and oxygen as reagents or reaction products. To compare the overall stabilities of the different iron sites and to clarify the preferred transformation path, the whole interconversion cycle is summarized in Figure 2.13. Under the assumption that the cubic $[\text{Fe}^{\text{III}}_4\text{O}_6]$ iron-oxo complex cluster, which resembles iron oxide, could be present as the starting species in the micropores of ZSM-5, there are three possible conversion paths whose importance will depend on the conditions of treatment. The direct decomposition of the four-nuclear cluster toward neutral neutral binuclear $[\text{OFe}(\mu\text{-O})\text{FeO}]$ is much less favorable than the alternative protonation and autoreduction mechanisms. The preference for one of the two latter paths is due to the direct availability of zeolitic acid sites in the immediate vicinity of the confined oxidic cluster. Indeed, at high temperatures under oxygen-free conditions, this cluster will undergo autoreduction resulting in the formation of Fe(II)-containing $[\text{Fe}_4\text{O}_4]$ neutral species which have a higher mobility within the zeolite channels. Subsequent protonation of this complex followed by water release leads to the stable binuclear $[\text{Fe}(\mu\text{-O})\text{Fe}]^{2+}$ complexes. The strong endothermicity of the autoreduction process is consistent with the experimental requirement of high-temperature pretreatment to obtain intrazeolitic Fe^{2+} ions [40]. One should note that further conversion of such binuclear species to isolated Fe^{2+} sites can only take place when specific cationic sites with symmetrically distributed lattice Al are available.

The alternative direct protonation of the initial oxidic cluster initiates a path ultimately resulting in the formation of binuclear $[\text{Fe}(\mu\text{-O})_2\text{Fe}]^{2+}$ complexes. In the presence of water, these can be hydrolyzed toward hydroxylated $[\text{HOFe}(\mu\text{-O})\text{FeOH}]^{2+}$ clusters. The formation of mononuclear Fe(III) sites is generally unfavorable.

2.3.6. *Ab initio* thermodynamic analysis

To account for the effect of temperature as well as the presence of H_2O and O_2 upon the catalyst activation on the stability of different extraframework iron complexes in Fe/ZSM-5, a statistical thermodynamic approach is used. We consider the equilibrium reaction



The corresponding reaction energy is then defined as

$$\Delta E = E_{\text{Fe}_x\text{O}_m\text{H}_n/\text{ZSM-5}} + \frac{n+3x-2m-2}{4}E_{\text{O}_2} - \frac{n-2}{2}E_{\text{H}_2\text{O}} - \frac{x}{2}E_{\text{Fe}_2\text{O}_3} - E_{\text{ZSM-5-2H}} \quad (2-2)$$

$E_{\text{Fe}_x\text{O}_m\text{H}_n/\text{ZSM-5}}$ is the total energy of the iron-containing ZSM-5 model with a given composition and structure; $E_{\text{ZSM-5-2H}}$ is the energy of the H-form of ZSM-5 with two Al

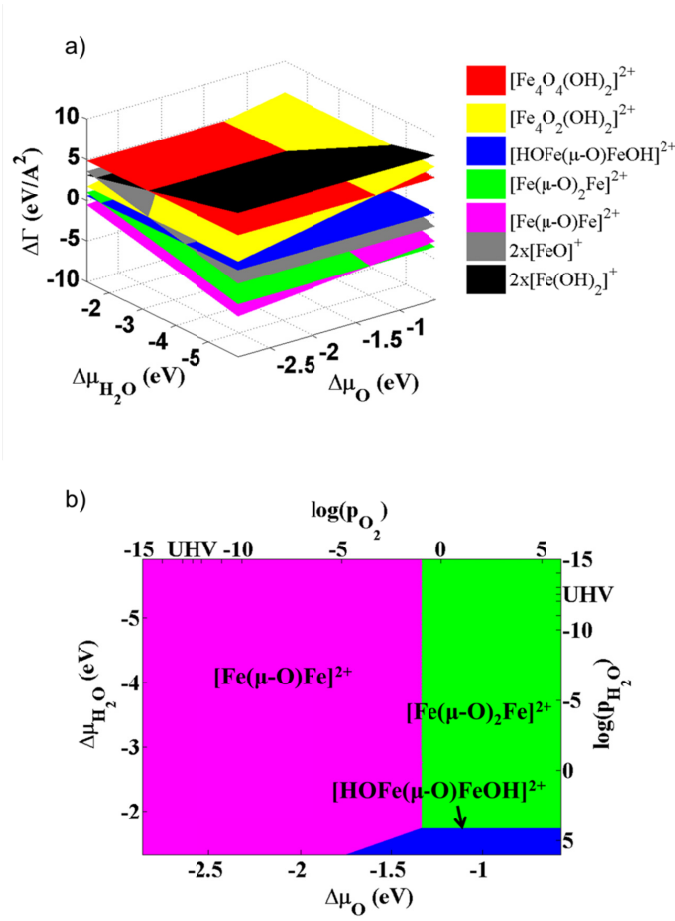


Figure 2.14. (a) Free energy of formation of $\text{Fe}_x\text{O}_m\text{H}_n$ in ZSM-5 ($\Delta\Gamma$), cf. Eq. (2-3), as a function of oxygen chemical potential ($\Delta\mu_{\text{O}}$) and water chemical potential ($\Delta\mu_{\text{H}_2\text{O}}$). (b) $\Delta\mu_{\text{O}}$ and $\Delta\mu_{\text{H}_2\text{O}}$ are translated into pressure scales at $T = 1100$ K.

substituted at T7 and T12 sites of 8MR; and $E_{\text{Fe}_2\text{O}_3}$, E_{O_2} , and $E_{\text{H}_2\text{O}}$ correspond to the computed total energies of bulk $\alpha\text{-Fe}_2\text{O}_3$, gaseous water, and oxygen molecules, respectively. The factor x denotes the number of Fe atoms in the unit cell of the $\text{Fe}_x\text{O}_m\text{H}_n/\text{ZSM-5}$ system. We consider x equal to 0.5, 1, or 2 depending on the specific structure of iron-containing species in the unit cell. The accompanying change in the free energy $\Delta\Gamma$ is given by

$$\Delta\Gamma(T, P) = \frac{1}{A} \left[\Delta E + \frac{n+3x-2m-2}{4} \Delta\mu_{\text{O}} - \frac{n-2}{2} \Delta\mu_{\text{H}_2\text{O}} \right] \quad (2-3)$$

where A is the area of the unit cell. The chemical potential differences, $\Delta\mu_i$, are defined as

$$\Delta\mu_{\text{O}}(T, p) = \frac{1}{2} \left[\Delta\mu_{\text{O}_2}(T, p^0) + RT \ln \left(\frac{p_{\text{O}_2}}{p^0} \right) \right] \quad (2-4)$$

$$\Delta\mu_{H_2O}(T, p) = \Delta\mu_{H_2O}(T, p^0) + RT \ln \left(\frac{p_{H_2O}}{p^0} \right) \quad (2-5)$$

The formation of the particular intrazeolitic iron complexes is controlled by the conditions of catalyst activation (partial pressures of H₂O and O₂ as well as the activation temperature, Figure 2.14). At high temperatures (1100 K), the completely dehydroxylated binuclear iron complexes will dominate. Binuclear Fe(II) clusters are preferred when the catalyst activation is performed under water-free conditions with low partial pressure of O₂ or in vacuum. Under oxidizing conditions, binuclear Fe(III) species are the dominant structures in Fe/ZSM-5.

2.4. Discussion

The main result of the comparison of the stability of ferrous ions at cation exchange sites of the ZSM-5 is their high stability at 6MR units. The most stable configuration is Fe²⁺ at the δ -1 site, involving a symmetric coordination environment of Fe²⁺ to four framework oxygen anions, each coordinating to one Al T atom. When the Al substitutions are placed at different framework positions of the δ - site in such way that the symmetry of the negative framework charge is broken, the zeolite lattice becomes distorted. Obviously, these configurations are less preferred for Fe²⁺. Similar but more pronounced distortions were found for Fe²⁺ at the α - and β - sites of ZSM-5. These distortions are driven by the tendency of the more basic oxygen ions of the anionic [AlO₂]⁻ units to form direct interactions with the extraframework cation and may lead to destabilization of Fe²⁺ adsorption by values up to 120 kJ/mol. For the case when the cation charge is compensated by only one Al³⁺ in the direct coordination environment (with the other [AlO₂]⁻ in an adjacent zeolite ring), the system is also substantially destabilized (+200 kJ/mol). The preference of the location of Fe²⁺ at the 6MR in the ZSM-5 lattice is in good agreement with the findings of Benco et al., who investigated the location of Fe²⁺ in ferrierite [71]. The stabilization within smaller 5MR units of the ZSM-5 lattice is less favorable, mainly due to inability to form a square-planar coordination environment of iron as is the case for the 6MR units. The high flexibility of the 8MR allows lattice oxygen to efficiently shield the exchangeable Fe²⁺ cations resulting in their relatively high stability at the γ -1 site.

The stability of Fe²⁺ strongly depends on the flexibility of the zeolitic site to which it coordinates and the distribution of the charge-compensating Al substitutions in the zeolite lattice. The preferred location of isolated Fe²⁺ involves six-membered rings with a symmetric distribution of framework Al atoms within the same ring. When these requirements are not met, iron will be present as isolated [FeO]⁺ and oxygen/hydroxy-bridged binuclear Fe²⁺ and Fe³⁺ complexes.

For the distributions of mononuclear [FeO]⁺ in the zeolite matrix, our results indicate that the local zeolitic configurations have a slight influence on it. It is understandable since this kind of species only needs one charge-compensating Al site around. It is different from the situation of bivalent Fe²⁺ cations or other multinuclear cationic complexes, which need two

or more negative $[\text{AlO}_2]^-$ unit spontaneously concurrent nearby. Furthermore, the 3-fold coordination of $[\text{FeO}]^+$ anchored on two framework negative oxygen atoms is also easy to approach in the zeolite. From this point of consideration, $[\text{FeO}]^+$ species should be easily present in high Si/Al zeolite. However, our further exploration demonstrated that these $[\text{FeO}]^+$ species strongly tend to aggregate into cluster particles because of the rather low coordination unsaturation and high instability of terminal oxygen atoms and iron centers. The self-organization is highly favorable despite their stabilization by neutral Si sites but not negative Al sites. This phenomenon is expected to be a general process for extraframework transition metal cations in zeolite [34] and can explain most of the experiment observation that, after high-temperature pretreatment, iron oxide clusters are usually detectable regardless the preparation method.

Although many theoretical researchers chose the cluster model of double five-membered rings as the location stabilizing the iron active site [44, 51, 56], the stability investigation of both mononuclear Fe^{2+} and binuclear $[\text{Fe}(\mu\text{-O})\text{Fe}]^{2+}$ and $[\text{Fe}(\mu\text{-O})_2\text{Fe}]^{2+}$ by periodic DFT calculation shows these species are more stable over an eight-membered ring in the sinusoidal channel. Double 5MRs are not stable for both cases. The other positions, such as α , β , and δ sites, are also possible candidates. According to the normal principle of the less stable the active sites, the more reactive over them, 5MRs could probably be the preferred reaction site. However, our previous stability study on $[\text{FeO}]^{2+}$ formed after α -oxygen generation again indicated 5MRs are the least stable position compared to others. It implies for theoretical investigations using cluster model, one should be cautious about choosing the locations of cationic sites. Furthermore, the dispersion interaction between hydrocarbon adsorbates and the zeolitic wall also significantly influences the reaction profile. Therefore, periodic DFT or QM/MM calculations including integrated zeolitic environment are necessary to get more accurate results.

Due to the diversity of the iron-containing species in Fe/ZSM-5, it is reasonable to use theoretical methods as a complement to experimental methods to get a clear view of what types of Fe sites might be present dominantly under specific conditions and the mechanism by which this process occurs. In the experiment, the as-synthesized catalysts are normally activated by calcination in vacuum, air, or O_2 at temperatures around 500-600 °C [77-80]. Accompanying this process, the iron species are migrating from framework to extraframework positions (for Fe sources added at the stage of synthesis zeolite), autoreduced from Fe^{3+} into the Fe^{2+} state (for Fe sources introduced by postsynthetic modification methods, such as CVD and iron-exchange), and undergo structural reconstruction. The activity of catalysts for specific reactions changes remarkably after further 700-900 °C high-temperature [81-83] or steaming [30, 40, 84] treatments, which means high-temperature and steaming treatments can additionally affect the distribution and even the nature of the Fe species in Fe/ZSM-5. On the basis of our results, it is shown that both autoreduction and decomposition of multinuclear Fe_xO_y nanoparticles need to overcome quite high reaction barriers. Only under high-temperature treatment multinuclear iron oxide nanoparticles are transformed into smaller binuclear sites. Protolysis of

Brønsted acid sites can intensively change the distribution of various iron-containing species from neutral multinuclear Fe_xO_y nanoclusters into hydroxylated $\text{Fe}_x\text{O}_y\text{H}_z$ cationic nanocomplexes, binuclear $[\text{HOFe}(\mu\text{-O})\text{FeOH}]^{2+}$, $[\text{Fe}(\mu\text{-O})\text{Fe}]^{2+}$, or $[\text{Fe}(\mu\text{-O})_2\text{Fe}]^{2+}$ complexes. Moreover, high-temperature steaming treatment will dramatically disturb the balance and lead to further intensifying diversification of intrazeolitic iron-containing species. This is consistent with the experimental observation that high-temperature steamed catalysts exhibit better catalytic activity for both N_2O decomposition and benzene oxidation reactions. Concerning the decrease of activity for N_2O decomposition upon exposure of the catalyst to water vapor at low temperature and reversible transformation [30], it could be due to the formation of inactive hydroxylated Fe^{3+} species $[\text{OHFe}(\mu\text{-O})\text{FeOH}]^{2+}$ and $[\text{Fe}(\text{OH})_2]^{2+}$.

2.5. Conclusion

The stability of mononuclear Fe^{2+} and oxygenated iron cations, their self-organization into binuclear species, and the preferred location of the resulting binuclear cationic Fe complexes in ZSM-5 zeolite are investigated by periodic DFT calculations. The energies are used to construct a reaction scheme describing the interconversion of different Fe complexes in zeolite voids upon the thermochemical activation of Fe/ZSM-5 catalyst. The stability of Fe^{2+} strongly depends on the flexibility of the zeolitic site to which it coordinates and the distribution of the charge-compensating Al substitutions in the zeolite lattice. The preferred location of isolated Fe^{2+} involves six-membered rings with a symmetric distribution of framework Al atoms within the same ring. The distribution of $[\text{FeO}]^+$ cations in zeolite depends only slightly on the local configurations of the zeolite cationic sites. Such species are unstable and tend to self-organize into binuclear cationic clusters. This process is driven by the stabilization of undercoordinated metal centers and excessively basic terminal oxygen via the formation of oxygen-bridged complexes. The resulting binuclear species can be effectively stabilized at a large variety of different zeolitic sites. Although the coordination of $[\text{Fe}(\mu\text{-O})\text{Fe}]^{2+}$ and $[\text{Fe}(\mu\text{-O})_2\text{Fe}]^{2+}$ cations at the 8MR γ site within the sinusoidal channel is thermodynamically preferred, configurations with comparable stability can be formed also at α , δ , and β 6MRs.

The various iron-containing species and their relative stabilities were used in a reaction scheme involving their interconversion involving H_2O , O_2 , and zeolitic protons as further reactants. An initial neutral Fe_4O_x cluster will readily decompose into binuclear species through protonation over Brønsted acid sites. Subsequent transformations of the hydroxylated binuclear complexes proceed via hydrolysis to isolated oxygenated or hydroxylated mononuclear species or via dehydration to oxygen-bridged $[\text{Fe}(\mu\text{-O})\text{Fe}]^{2+}$ species. The latter path is preferred. An *ab initio* thermodynamic analysis of the stability of different iron-containing structures with respect to the composition of the gas phase during catalyst activation was performed. $[\text{Fe}(\mu\text{-O})\text{Fe}]^{2+}$ is the most stable species under reducing conditions, whereas this complex is oxidized into a $[\text{Fe}(\mu\text{-O})_2\text{Fe}]^{2+}$ binuclear cluster in the presence of oxygen. All other potential Fe complexes are very unstable under the catalyst

activation conditions. Only at high temperature the formation of Fe²⁺ ions and binuclear complexes will occur, in keeping with experimental studies.

References

- [1] V.I. Sobolev, G.I. Panov, A.S. Kharitonov, V.N. Romannikov, A.M. Volodin, K.G. Ione. *J. Catal.* 139 (1993) 435-443.
- [2] H.Y. Chen, W.M.H. Sachtler. *Catal. Today* 42 (1998) 73-83.
- [3] E.M. El-Malki, R.A. van Santen, W.M.H. Sachtler. *Microporous Mesoporous Mater.* 35-6 (2000) 235-244.
- [4] J. Perez-Ramirez, F. Kapteijn, G. Mul, J.A. Moulijn. *Chem. Commun.* (2001) 693-694.
- [5] J. Perez-Ramirez, F. Kapteijn, G. Mul, J.A. Moulijn. *Appl. Catal. B* 35 (2002) 227-234.
- [6] B.R. Wood, J.A. Reimer, A.G. Bell. *J. Catal.* 209 (2002) 151-158.
- [7] T.V. Voskoboinikov, H.Y. Chen, W.M.H. Sachtler. *Appl. Catal. B* 19 (1998) 279-287.
- [8] H.Y. Chen, T. Voskoboinikov, W.M.H. Sachtler. *J. Catal.* 180 (1998) 171-183.
- [9] Q. Sun, Z.X. Gao, H.Y. Chen, W.M.H. Sachtler. *J. Catal.* 201 (2001) 89-99.
- [10] B. Wichterlova. *Top. Catal.* 28 (2004) 131-140.
- [11] J. Perez-Ramirez, A. Gallardo-Llamas. *J. Phys. Chem. B* 109 (2005) 20529-20538.
- [12] G.I. Panov, V.I. Sobolev, A.S. Kharitonov. *J. Mol. Catal.* 61 (1990) 85-97.
- [13] G.I. Panov, G.A. Sheveleva, A.S. Kharitonov, V.N. Romannikov, L.A. Vostrikova. *Appl. Catal., A* 82 (1992) 31-36.
- [14] V.I. Sobolev, A.S. Kharitonov, Y.A. Paukshtis, G.I. Panov. *J. Mol. Catal.* 84 (1993) 117-124.
- [15] K.A. Dubkov, V.I. Sobolev, E.P. Talsi, M.A. Rodkin, N.H. Watkins, A.A. Shteinman, G.I. Panov. *J. Mol. Catal. A* 123 (1997) 155-161.
- [16] V.I. Sobolev, K.A. Dubkov, E.A. Paukshtis, L.V. Pirutko, M.A. Rodkin, A.S. Kharitonov, G.I. Panov. *Appl. Catal., A* 141 (1996) 185-192.
- [17] G.I. Panov. *CATTECH* 4 (2000) 18-31.
- [18] K.A. Dubkov, N.S. Ovanesyan, A.A. Shteinman, E.V. Starokon, G.I. Panov. *J. Catal.* 207 (2002) 341-352.
- [19] R. Joyner, M. Stockenhuber. *J. Phys. Chem. B* 103 (1999) 5963-5976.
- [20] P. Kubanek, B. Wichterlova, Z. Sobalik. *J. Catal.* 211 (2002) 109-118.
- [21] S.H. Choi, B.R. Wood, J.A. Ryder, A.T. Bell. *J. Phys. Chem. B* 107 (2003) 11843-11851.
- [22] A. Ribera, I. Arends, S. de Vries, J. Perez-Ramirez, R.A. Sheldon. *J. Catal.* 195 (2000) 287-297.
- [23] E.J.M. Hensen, Q. Zhu, R.A.J. Janssen, P. Magusin, P.J. Kooyman, R.A. van Santen. *J. Catal.* 233 (2005) 123-135.
- [24] A. Heyden, B. Peters, A.T. Bell, F.J. Keil. *J. Phys. Chem. B* 109 (2005) 1857-1873.
- [25] P. Marturano, L. Drozdova, G.D. Pirngruber, A. Kogelbauer, R. Prins. *Phys. Chem. Chem. Phys.* 3 (2001) 5585-5595.
- [26] H. Xia, K. Sun, Z. Feng, W.X. Li, C. Li. *J. Phys. Chem. C* 112 (2008) 9001-9005.
- [27] H.A. Xia, K.Q. Sun, Z.M. Liu, Z.C. Feng, P.L. Ying, C. Li. *J. Catal.* 270 (2010) 103-109.
- [28] H. Xia, K. Sun, Z. Feng, C. Li. *J. Phys. Chem. C* 115 (2010) 542-548.
- [29] H.A. Xia, S.D. Fleischman, C. Li, S.L. Scott. *J. Phys. Chem. Lett.* 2 (2011) 190-195.
- [30] Q. Zhu, E.J.M. Hensen, B.L. Mojet, J. van Wolput, R.A. van Santen. *Chem. Commun.* (2002) 1232-1233.
- [31] L.J. Lobree, I.-C. Hwang, J.A. Reimer, A.T. Bell. *J. Catal.* 186 (1999) 242-253.
- [32] A.V. Kucherov, M. Shelef. *J. Catal.* 195 (2000) 106-112.
- [33] S.H. Choi, B.R. Wood, A.T. Bell, M.T. Janicke, K.C. Ott. *J. Phys. Chem. B* 108 (2004) 8970-8975.
- [34] E.A. Pidko, E.J.M. Hensen, R.A. van Santen. *Proc. R. Soc. A* 468 (2012) 2070-2086.
- [35] A.A. Battiston, J.H. Bitter, D.C. Koningsberger. *Catal. Lett.* 66 (2000) 75-79.
- [36] A.A. Battiston, J.H. Bitter, F.M.F. de Groot, A.R. Overweg, O. Stephan, J.A. van Bokhoven, P.J. Kooyman, C. van der Spek, G. Vankó, D.C. Koningsberger. *J. Catal.* 213 (2003) 251-271.
- [37] A.A. Battiston, J.H. Bitter, W.M. Heijboer, F.M.F. de Groot, D.C. Koningsberger. *J. Catal.* 215 (2003) 279-293.
- [38] A.A. Battiston, J.H. Bitter, D.C. Koningsberger. *J. Catal.* 218 (2003) 163-177.
- [39] P. Marturano, L. Drozdov, A. Kogelbauer, R. Prins. *J. Catal.* 192 (2000) 236-247.
- [40] E.J.M. Hensen, Q. Zhu, M.M.R.M. Hendrix, A.R. Overweg, P.J. Kooyman, M.V. Sychev, R.A. van Santen. *J. Catal.* 221 (2004) 560-574.
- [41] Q. Zhu, R.M. van Teeffelen, R.A. van Santen, E.J.M. Hensen. *J. Catal.* 221 (2004) 575-583.

- [42] K. Yoshizawa, T. Yumura, Y. Shiota, T. Yamabe. *Bull. Chem. Soc. Jpn.* 73 (2000) 29-36.
- [43] K. Yoshizawa, Y. Shiota, T. Yumura, T. Yamabe. *J. Phys. Chem. B* 104 (2000) 734-740.
- [44] M.F. Fellah, R.A. van Santen, I. Onal. *J. Phys. Chem. C* 113 (2009) 15307-15313.
- [45] N.A. Kachurovskaya, G.M. Zhidomirov, E.J.M. Hensen, R.A. van Santen. *Catal. Lett.* 86 (2003) 25-31.
- [46] N.A. Kachurovskaya, G.M. Zhidomirov, R.A. van Santen. *J. Phys. Chem. B* 108 (2004) 5944-5950.
- [47] M.F. Fellah, I. Onal, R.A. van Santen. *J. Phys. Chem. C* 114 (2010) 12580-12589.
- [48] M.F. Fellah, E.A. Pidko, R.A. van Santen, I. Onal. *J. Phys. Chem. C* 115 (2011) 9668-9680.
- [49] A.L. Yakovlev, G.M. Zhidomirov, R.A. van Santen. *J. Phys. Chem. B* 105 (2001) 12297-12302.
- [50] A. Heyden, N. Hansen, A.T. Bell, F.J. Keil. *J. Phys. Chem. B* 110 (2006) 17096-17114.
- [51] N. Hansen, A. Heyden, A.T. Bell, F.J. Keil. *J. Phys. Chem. C* 111 (2007) 2092-2101.
- [52] N. Hansen, A. Heyden, A.T. Bell, F.J. Keil. *J. Catal.* 248 (2007) 213-225.
- [53] L. Benco, T. Bucko, R. Grybos, J. Hafner, Z. Sobalik, J. Dedecek, S. Sklenak, J. Hrusak. *J. Phys. Chem. C* 111 (2007) 9393-9402.
- [54] S. Sklenak, P.C. Andrikopoulos, B. Boekfa, B. Jansang, J. Novakova, L. Benco, T. Bucko, J. Hafner, J. Dedecek, Z. Sobalik. *J. Catal.* 272 (2010) 262-274.
- [55] L. Kiwi-Minsker, D.A. Bulushev, A. Renken. *J. Catal.* 219 (2003) 273-285.
- [56] H. Guesmi, D. Berthomieu, L. Kiwi-Minsker. *J. Phys. Chem. C* 112 (2008) 20319-20328.
- [57] H. Guesmi, D. Berthomieu, B. Bromley, B. Coq, L. Kiwi-Minsker. *Phys. Chem. Chem. Phys.* 12 (2010) 2873-2878.
- [58] J.P. Perdew, K. Burke, M. Ernzerhof. *Phys. Rev. Lett.* 77 (1996) 3865-3868.
- [59] G. Kresse, J. Hafner. *Phys. Rev. B* 48 (1993) 13115-13118.
- [60] G. Kresse, J. Hafner. *Phys. Rev. B* 49 (1994) 14251-14269.
- [61] G. Kresse, J. Furthmuller. *Comput. Mater. Sci.* 6 (1996) 15-50.
- [62] G. Kresse, J. Furthmuller. *Phys. Rev. B* 54 (1996) 11169-11186.
- [63] P.E. Blochl. *Phys. Rev. B* 50 (1994) 17953-17979.
- [64] G. Kresse, D. Joubert. *Phys. Rev. B* 59 (1999) 1758-1775.
- [65] H. van. *Acta Crystallographica Section B* 46 (1990) 731-735.
- [66] *Database of Zeolite Structures* <http://www.iza-structure.org/databases/>.
- [67] J. Dedecek, D. Kaucky, B. Wichterlova. *Microporous Mesoporous Mater.* 35-6 (2000) 483-494.
- [68] E.A. Pidko, R.A. van Santen. *J. Phys. Chem. C* 111 (2007) 2643-2655.
- [69] E.A. Pidko, E.J.M. Hensen, R.A. van Santen. *J. Physical Chem. C* 111 (2007) 13068-13075.
- [70] J. Dedecek, B. Wichterlova. *Phys. Chem. Chem. Phys.* 1 (1999) 629-637.
- [71] L. Benco, T. Bucko, R. Grybos, J. Hafner, Z. Sobalik, J. Dedecek, J. Hrusak. *J. Phys. Chem. C* 111 (2006) 586-595.
- [72] L. Benco, T. Bucko, J. Hafner, H. Toulhoat. *J. Phys. Chem. B* 109 (2005) 20361-20369.
- [73] D. Nachtigallova, P. Nachtigall, M. Sierka, J. Sauer. *Phys. Chem. Chem. Phys.* 1 (1999) 2019-2026.
- [74] E.A. Pidko, R.A. van Santen, E.J.M. Hensen. *Phys Chem Chem Phys* 11 (2009) 2893-2902.
- [75] E.A. Pidko, E.J.M. Hensen, G.M. Zhidomirov, R.A. van Santen. *J. Catal.* 255 (2008) 139-143.
- [76] L. Kiwi-Minsker, D.A. Bulushev, A. Renken. *Catal. Today* 91-2 (2004) 165-170.
- [77] H.-Y. Chen, W.M.H. Sachtler. *Catal. Today* 42 (1998) 73-83.
- [78] M. Yoshida, T. Nobukawa, S.I. Ito, K. Tomishige, K. Kunimori. *J. Catal.* 223 (2004) 454-464.
- [79] E.M. El-Malki, R.A. van Santen, W.M.H. Sachtler. *J. Catal.* 196 (2000) 212-223.
- [80] G.I. Panov, E.V. Starokon, L.V. Pirutko, E.A. Paukshtis, V.N. Parmon. *J. Catal.* 254 (2008) 110-120.
- [81] K. Sun, H. Xia, Z. Feng, R. van Santen, E. Hensen, C. Li. *J. Catal.* 254 (2008) 383-396.
- [82] P.K. Roy, R. Prins, G.D. Pirngruber. *Appl. Catal. B* 80 (2008) 226-236.
- [83] D.A. Bulushev, P.M. Prechtel, A. Renken, L. Kiwi-Minsker. *Ind. Eng. Chem. Res.* 46 (2007) 4178-4185.
- [84] Q. Zhu, B.L. Mojet, R.A.J. Janssen, E.J.M. Hensen, J. van Grondelle, P. Magusin, R.A. van Santen. *Catal. Lett.* 81 (2002) 205-210.



CHAPTER 3

DIRECT BENZENE OXIDATION TO PHENOL IN Fe/ZSM-5: A COMPREHENSIVE PERIODIC DFT STUDY

The reactivity of isolated extraframework Fe^{2+} ions and oxygenated/hydroxylated mono- and binuclear iron complexes in ZSM-5 zeolite in the benzene to phenol oxidation were studied by periodic DFT calculations. The reactivity of isolated Fe^{2+} does not depend on the local coordination environment around iron, whereas the steric constraints imposed by the zeolite lattice are important for the overall catalytic reactivity. $[FeO]^+$, $[HOFe(\mu-O)FeOH]^{2+}$, $[Fe(\mu-O)_2Fe]^{2+}$, and $[Fe(\mu-O)Fe]^{2+}$ extraframework complexes are also potential sites for benzene activation. The reaction is however not catalytic in these cases because the vacant active site cannot be regenerated. The presence of basic extraframework O ligands in these complexes favors phenol dissociation resulting in the formation of stable grafted phenolate species, and ultimately, to the deactivation of the oxygenated iron complexes.

3.1. Introduction

The Fe/ZSM-5 catalyst can oxidize methane to methanol and benzene to phenol, but only the latter reaction can be carried out in a catalytic manner so far [1-6]. There is quite some data in support of isolated Fe^{2+} ions as the active site for benzene oxidation, whereas dispersed oligonuclear and most likely binuclear Fe complexes form the active sites for catalytic N_2O decomposition [7-28]. It has also been proposed that extraframework Al and Ga species may play a role in the active sites for benzene oxidation [2, 28-31]. The role of isolated Fe^{3+} and binuclear complexes in benzene oxidation is unclear. Due to the relatively heterogeneous nature of extraframework Fe species, the low concentrations of Fe^{2+} and, accordingly, the difficulty in determining the nuclearity of the Fe species in Fe/ZSM-5, a clear assignment of the active site for benzene oxidation remains moot [32-35].

In such case, computational modeling can assist in predicting the stability and reactivity of various Fe sites at different locations of the zeolite lattice. So far, most studies have employed cluster models. Bell et al. reported on the reaction mechanism of N_2O decomposition on different (de)hydrated mononuclear Fe sites in Fe/ZSM-5 [36-39]. Different binuclear Fe complexes have also been proposed before by several groups for N_2O decomposition. Binuclear Fe sites may form upon the self-organization of oxygenated or hydroxylated mononuclear Fe ions. The reactivity of binuclear $[\text{HO}-\text{Fe}(\mu\text{-O})\text{Fe}-\text{OH}]^{2+}$ and $[\text{Fe}(\mu\text{-O})\text{Fe}]^{2+}$ complexes for catalytic N_2O decomposition has been discussed in the literature [40-42]. An alternative diamond core $[\text{Fe}(\mu\text{-OH})\text{Fe}]^+$ complex was proposed by Kiwi-Minsker and co-workers [43-47]. A peroxide $[\text{Fe}(\mu\text{-OO})(\mu\text{-O})\text{Fe}]^{2+}$ bridged on the binuclear sites generated during the catalytic N_2O decomposition was also proposed [19]. Recently, Sklenak et al. investigated the reactivity for N_2O dissociation over two Fe^{2+} cations placed in two adjacent six-membered rings of Fe/ferrierite, Fe/ZSM-5, and Fe/Beta [48]. These authors concluded that the proximity of two Fe^{2+} ions at a distance of 7.4 Å in ferrierite is essential to explain its superior catalytic activity. In the case of beta and ZSM-5 zeolites the probability of the formation of such a specific configuration was predicted to be very low.

The first computational study on the reaction mechanism for benzene to phenol oxidation using a cluster model representing Fe/ZSM-5 was carried out by Yoshizawa et al [49]. An isolated $[\text{FeO}]^+$ ion was used as the active site. As a model of Fe^{2+} in ZSM-5, the group of van Santen considered the ferrous ion at the α position of ferrierite to compute the potential energy diagram of the selective benzene oxidation [50]. Isolated Fe^+ , Fe^{2+} , and $[\text{FeO}]^+$ ions were considered as the active sites for N_2O dissociation and benzene oxidation by Fellah et al [51-53].

Despite substantial experimental and theoretical effort aimed at identifying the active site in Fe/ZSM-5 catalysts, the role of the different intrazeolitic iron sites in catalytic benzene to phenol oxidation as well as the actual mechanism of the catalytic reaction are still under debate. In Chapter 2 we already gave a comprehensive discussion about the distribution of

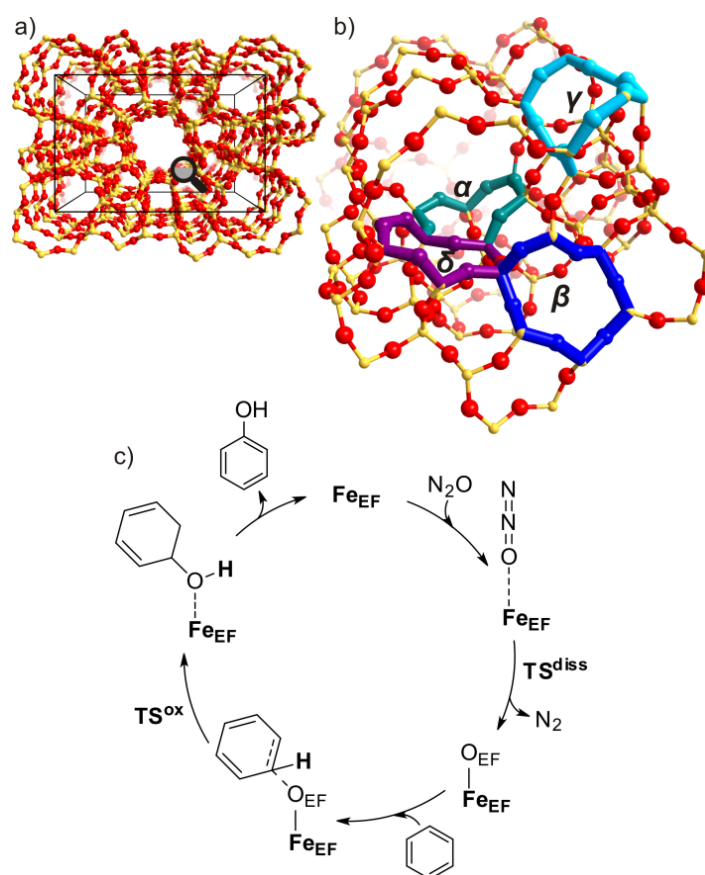


Figure 3.1. The structure of ZSM-5 zeolite (a) and the relative location of selected cation sites in it (b). Part (c) depicts a catalytic cycle for benzene to phenol oxidation with N_2O over extraframework iron (Fe_{EF}) sites.

various mononuclear and binuclear iron-containing species. Herein we present a further investigation of the catalytic oxidation of benzene to phenol over the preferred location of isolated Fe^{2+} in ZSM-5 zeolite (Figure 3.1(a) & (b)). To have a basis of comparison we also included FeO^+ (ferric ion) and a number of oxo/hydroxyl-bridged binuclear complexes in our study. The reaction mechanism for benzene oxidation to phenol considered over extraframework iron species (Fe_{EF}) is schematically shown in Figure 3.1(c). It involves (i) the adsorption and dissociation of N_2O , (ii) the adsorption and oxidation of benzene and (iii) the desorption of phenol. Following the proposal by Fellah et al. [53], we also considered the possibility of formation of grafted phenolate complexes. The majority of works on this subject have employed clusters that represent part of the zeolite framework. Two recent studies of Sklenak et al. [48] and Benco et al. [54] have employed periodic boundary conditions for the study of N_2O decomposition by Fe^{2+} in ferrierite zeolite. Such studies are lacking for Fe/ZSM-5 with a more complex unit cell composition. Currently,

calculations involving the complete unit cell of MFI zeolite are becoming accessible [55-58]. This presents an interesting possibility to determine the preferred location of the suspected active sites and to investigate the influence of the zeolitic micropores on their reactivity and ultimately to create a molecular picture of the role of different iron species in Fe/ZSM-5 catalyst in transformations of benzene to phenol.

3.2. Computational details

Quantum chemical calculations were performed using density functional theory (DFT) as implemented in the Vienna *ab initio* Simulation Package (VASP) [59-62]. The projected augmented waves (PAW) method with spin polarized calculations was used to describe electron-ion interactions [63, 64]. For the exchange and correlation energies the PBE form of the generalized gradient approximation was employed [65]. Brillouin zone-sampling was restricted to the Γ point [66]. The energy cut-off was set to 400 eV. Full geometry optimization was performed with fixed optimized cell parameters using a conjugated gradient algorithm. Convergence was assumed, when the energy change was smaller than 10^{-4} eV between two ionic steps. A modest Gaussian smearing was applied to band occupations around the Fermi level and the total energies were extrapolated to $\sigma \rightarrow 0$. In the first step, the cell parameters were optimized for the all-silica MFI orthorhombic structure ($\text{Si}_{96}\text{O}_{192}$) [67]. The parameters after optimization of volume and shape were as follows: $a = 20.119$, $b = 19.767$, and $c = 13.161$ Å, which corresponds very well to the experimental XRD data of $a = 20.090$ Å, $b = 19.738$ Å, and $c = 13.142$ Å [68]. By replacing two of the 96 unit-cell silicon atoms by two Al atoms, a ZSM-5 lattice with a Si/Al ratio of 47 was obtained. In the case of $[\text{FeO}]^+$ species a single framework Al atom was introduced in the unit cell (Si/Al = 95). The negative charge of the resulting anionic sites was compensated by extraframework iron cations. Mononuclear Fe^{2+} and $[\text{FeO}]^+$ as well as binuclear $[\text{Fe}(\mu\text{-O})\text{Fe}]^{2+}$, $[\text{Fe}(\mu\text{-O})_2\text{Fe}]^{2+}$, and $[\text{HOFe}(\mu\text{-O})\text{FeOH}]^{2+}$ extraframework complexes were considered as charge-compensating species. All calculations were performed with a fixed spin multiplicity corresponding to the most stable configuration of the initial iron complex. The lowest energy electronic configuration for Fe^{2+} is $S = 4/2$. For the dimeric $[\text{Fe}(\mu\text{-O})\text{Fe}]^{2+}$, $[\text{Fe}(\mu\text{-O})_2\text{Fe}]^{2+}$, and $[\text{HOFe}(\mu\text{-O})\text{FeOH}]^{2+}$ complexes the ferromagnetic $S = 8/2$ state was found to be the most stable. It should be noted that in the case of binuclear Fe^{III} clusters the high-spin states $S = 6/2$, $S = 8/2$, and $S = 10/2$ do not differ much in energy. The spin state has previously been shown to only have a minor influence on the reaction mechanism [41]. To confirm this, the reactivity of the mononuclear $\text{Fe}^{\text{III}}\text{O}^+$ species were compared for the most stable $S = 5/2$ and the less stable $S = 3/2$ states.

The nudged elastic band method (NEB) with improved tangent estimate was used to determine the minimum energy path and to locate the transition-state structures [69]. The maximum energy geometries obtained with the NEB method were further optimized using a quasi-Newton algorithm. In this step only the extraframework atoms were relaxed. Frequency analysis of the stationary points was performed by means of the finite difference

method as implemented in VASP. Small displacements (0.02 Å) were used to estimate the numerical Hessian matrix. The transition states were confirmed by the presence of a single imaginary frequency corresponding to the reaction path.

The energetics as computed with DFT was further corrected for dispersion interactions by adding the contributions from van der Waals bonds between the confined hydrocarbon species and the zeolitic matrix. These interactions were estimated by computing an additional interatomic Lennard-Jones potential for the DFT-optimized structures as defined in the consistent valence force field (CVFF) [70, 71] with the approach as proposed by Demuth et al. [72] and Vos et al. [73] using the GULP program [74]. The consistent valence force field (CVFF) is known to accurately describe trends involving dispersive interactions of hydrocarbons in zeolite pores [75, 76]. This methodology has recently been successfully employed for the description of the zeolite-catalyzed hydrocarbon conversion [57, 58]. For all structures including the local minima and transition states two subsystems were defined within the DFT-optimized periodic system, representing the hydrocarbon moiety and the zeolite. The vdW interaction between these subunits represents the vdW stabilization of the confined hydrocarbon species. Previous studies have shown that the addition of the empirical corrections to the results obtained at the PBE level results in both thermodynamic and kinetic parameters that are very close to those obtained at the higher *ab initio* level [77].

3.3. Results

3.3.1. Reaction mechanism of benzene oxidation on Fe^{2+} and $[\text{FeO}]^+$ in ZSM-5

We computed the reaction energy diagrams based on the following reaction mechanism (Figure 3.1(c)) for the oxidation of benzene to phenol with N_2O . First, N_2O molecule adsorbs physically on Fe^{2+} followed by its dissociation, resulting in $[\text{FeO}]^{2+}$ and gaseous N_2 . Subsequently, benzene interacts with the extraframework oxygen atom, resulting in the formation of a pre-activated adsorbed complex, which is the precursor for the subsequent oxidation step. After oxidation, the catalytic cycle closes by desorption of phenol from the coordination complex with Fe^{2+} . We considered benzene oxidation starting from Fe^{2+} located at δ -1, α -1, and β -1 site (Figure 3.1(b)). As the oxidation state of the active Fe centers in Fe/ZSM-5 catalysts has not been unequivocally established, we also included mononuclear Fe^{3+} species in our calculations. Similar to previous experimental [36, 78] and theoretical [53, 79, 80] studies, we considered $[\text{FeO}]^+$ as the active complex and carried out comparable calculations of reaction energy diagrams for $[\text{FeO}]^+$ stabilized at the δ -1 site containing one Al substitution at the T11 lattice position (Figure 3.1(b)). The consideration of a single cation site in this case is justified by the weak influence of the local zeolite environment on the geometrical properties and reactivity of the monovalent $[\text{FeO}]^+$ species [53, 79-81].

The reaction energy diagram for the oxidation of benzene to phenol by nitrous oxide catalyzed by Fe^{2+} at the δ -1 site is shown in Figure 3.2. The local optimized geometries of

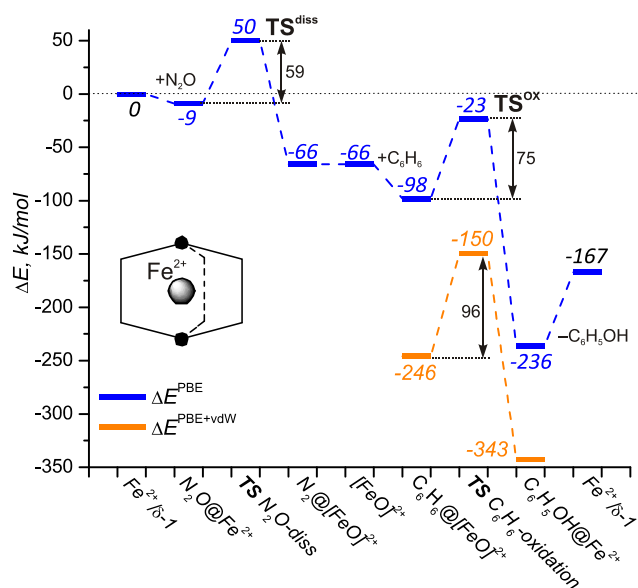


Figure 3.2. Reaction energy diagram for benzene oxidation to phenol by N_2O on mononuclear Fe^{2+} at the δ -1 site of ZSM-5.

all reaction intermediates and transition states are shown in Figure 3.3. Adsorption of N_2O is slightly exothermic with $\Delta E_{\text{ads}} = -9$ kJ/mol. Subsequent dissociation of the N–O bond and the formation of $[\text{FeO}]^{2+}$ and N_2 is thermodynamically favored ($\Delta E = -57$ kJ/mol). The main entropic contribution to the reaction free energy in this case is due to the rather small entropy difference between the gas-phase N_2O and N_2 (estimated $T\Delta S = 15$ kJ/mol at $T = 623$ K). Thus, the free reaction energies should be quite close to the reaction enthalpies. Accordingly, this implies that the oxidation reaction of Fe^{2+} by N_2O will go to completion under the typical conditions employed for titration of Fe^{2+} sites in Fe/ZSM-5 [13, 28].

N_2O dissociates with an activation barrier of only 59 kJ/mol. This value is close to the experimental value of 70 kJ/mol [82] and is somewhat lower than the value of 83 kJ/mol computed using a cluster model representing Fe^{2+} in a D5MRs unit [83]. The N_2 molecule interacts very weakly with $[\text{FeO}]^{2+}$. Physical adsorption of N_2O on Fe^{2+} leads to elongation of Fe– O_F bonds to 2.046–2.119 Å. The average Fe– O_F distance equals 2.075 Å. Because of the increase of the formal charge and, consequently, of the Lewis acidity of the iron cation, dissociation of N_2O results in shortening of the Fe– O_F distances to 2.032–2.044 Å and the average bond length is 2.038 Å. The Fe– O_{EF} bond length is 1.62 Å. In this configuration $[\text{FeO}]^{2+}$ forms an almost perfect square-pyramidal coordination environment of the iron cation (Figure 3.3). The perturbations of the local framework geometry following N_2O dissociation are very small. Further oxidation of $[\text{FeO}]^{2+}$ by N_2O resulting in $[\text{FeO}_2]^{2+}$ cations is very unlikely with a calculated energy difference of $\Delta E = +109$ kJ/mol. The high endothermicity is due to the highly unfavorable oxidation of formally

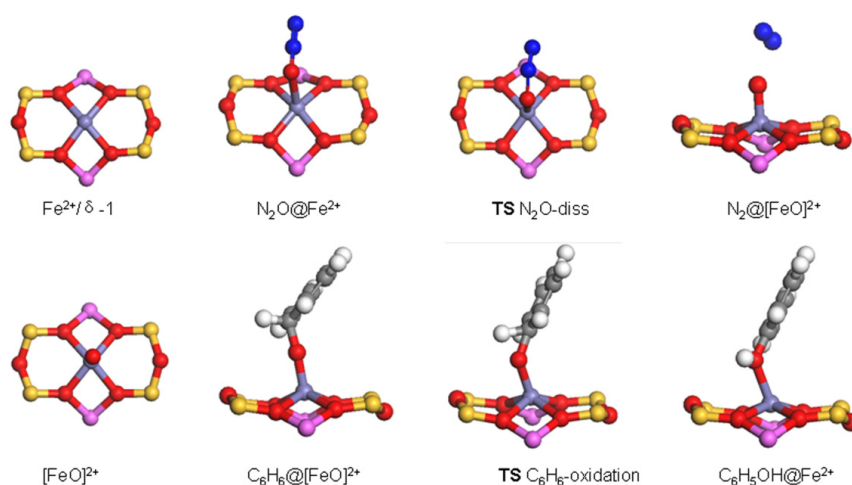


Figure 3.3. Local structures of all intermediates and transition states over mononuclear Fe^{2+} at the δ -1 site

Fe(IV) to Fe(VI) and the severe distortions resulting from the additional O ligand in the coordination sphere of iron.

The next step involves the adsorption of benzene on the extraframework oxygen atom of $[\text{FeO}]^{2+}$. Structural changes in the benzene ring point to a partial loss of the aromaticity and the formation of a σ -complex. One of the C–H bonds is elongated and protrudes from the initial plane of the benzene ring. The extraframework oxygen atom forms a bond with this carbon atom at a distance of 1.425 Å. The reaction energy (ΔE^{PBE}) for the formation of this activated complex is -32 kJ/mol. The activation barrier for phenol formation of 75 kJ/mol is substantially higher than the value of 41 kJ/mol predicted for Fe^{2+} stabilized in a D5MRs cluster [83]. Subsequent desorption of phenol and regeneration of the active Fe^{2+}/δ -1 site is endothermic. The reaction energy (ΔE^{PBE}) equals 69 kJ/mol for this step. This is almost twice lower as compared to the value reported by Fella et al [83]. The large deviations between our results and those obtained previously by Fella et al. using a cluster modeling approach are due to the more realistic representation of the intrazeolite environment by a periodic Fe/ZSM-5 model and the resulting substantial repulsive interactions between the confined hydrocarbon intermediates and the zeolitic walls.

Addition of the vdW contributions to the calculated energies ($\Delta E^{PBE+vdW}$) has a pronounced effect on the overall energy profiles, although the qualitative picture for the individual reaction steps remains unchanged (Figure 3.2). The influence of dispersive interactions is negligible for the transformations involving N_2O and these have therefore not been included. As the interaction between hydrocarbons and the zeolite oxygen anions are predominantly dispersive, substantial corrections were obtained for the states involving benzene and phenol in the zeolite micropores. The inclusion of these dispersive interactions makes the complete evacuation of phenol from the zeolite matrix much more

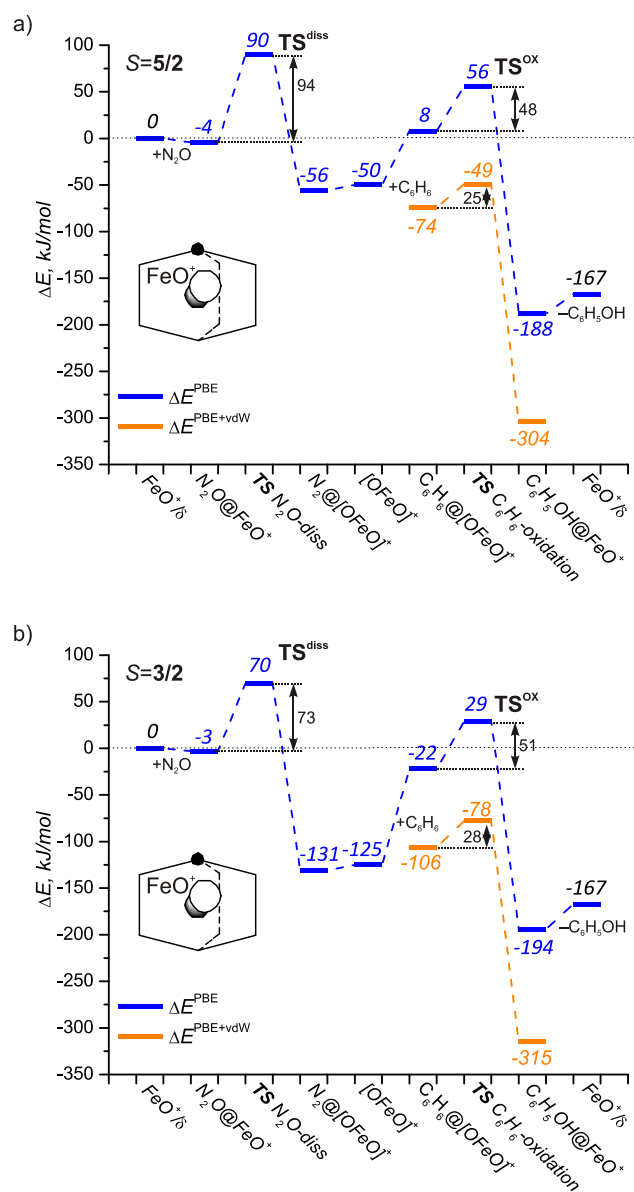


Figure 3.4. Reaction energy diagrams for benzene oxidation to phenol by N₂O over mononuclear FeO⁺ in (a) high-spin state ($S = 5/2$) and (b) low-spin state ($S = 3/2$).

endothermic ($\Delta E^{PBE+vdW} = 176$ kJ/mol) compared to the intrinsic barrier for benzene oxidation (96 kJ/mol). Obviously, the correction for the latter activation barrier is minor as compared to the desorption step, because of the similar magnitude of the Van der Waals stabilization of benzene and phenol in the zeolite channels.

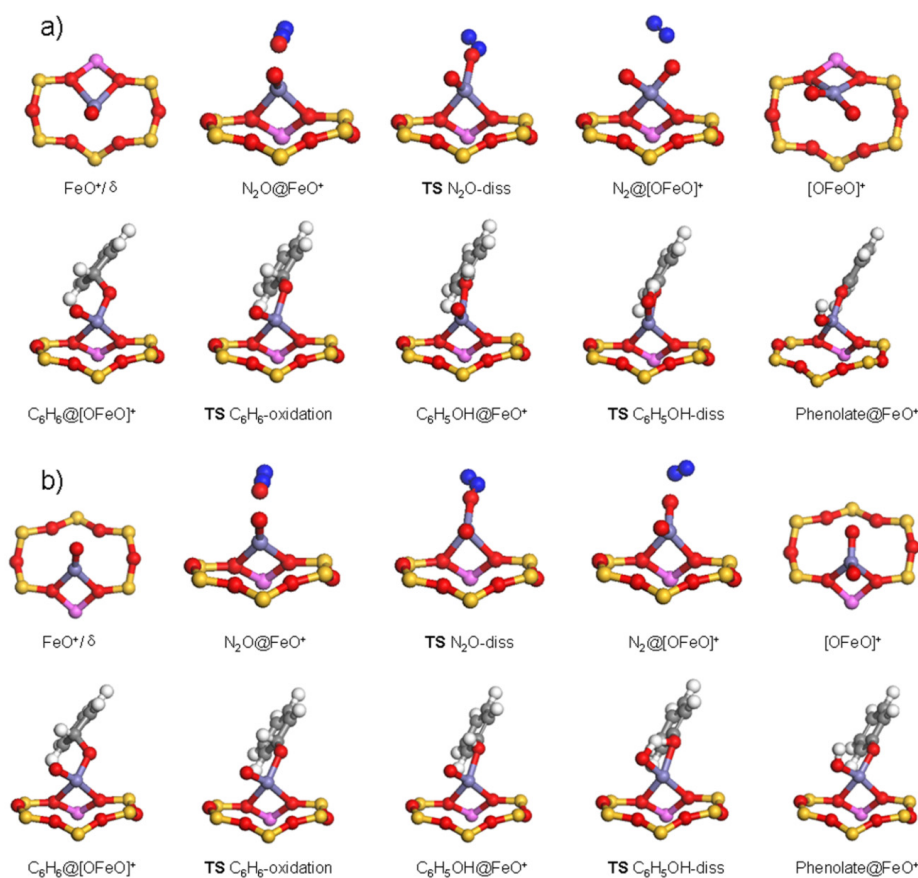


Figure 3.5. Local structures of all intermediates and transition states over mononuclear FeO⁺ in (a) high-spin state ($S = 5/2$) and (b) low-spin state ($S = 3/2$).

Geometry optimization of [FeO]⁺ at the δ -1 site containing a single framework Al substitution at the T11 site results in a three-coordinated complex with two Fe–O_F bonds. The complex is located above the plane of the 6MR unit of the δ -1 site. We considered the high ($S = 5/2$) and low spin ($S = 3/2$) states of Fe(III). The energy differences between these electronic configurations are 21 kJ/mol with a preference for the high spin state. Figures 3.4 (a) and (b) give the reaction energy diagrams for benzene oxidation for the high and low spin states, respectively. The local optimized geometries of all reaction intermediates and transition states are shown in Figure 3.5. The low spin structure of [OFeO]⁺ formed upon the dissociative adsorption of N₂O is more stable than the high spin equivalent. This result implies a very low barrier for spin flip depending on the specific coordination environment and the presence of adsorbates. The energy barriers for N₂O dissociation are 94 ($S = 5/2$) and 73 ($S = 3/2$) kJ/mol, while the respective values for the benzene oxidation are 48 and 51 kJ/mol. The adsorption energy (ΔE^{PBE}) of benzene on the

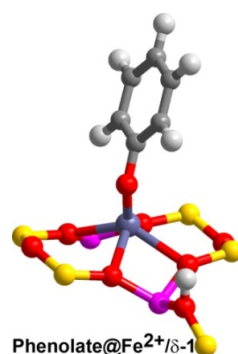
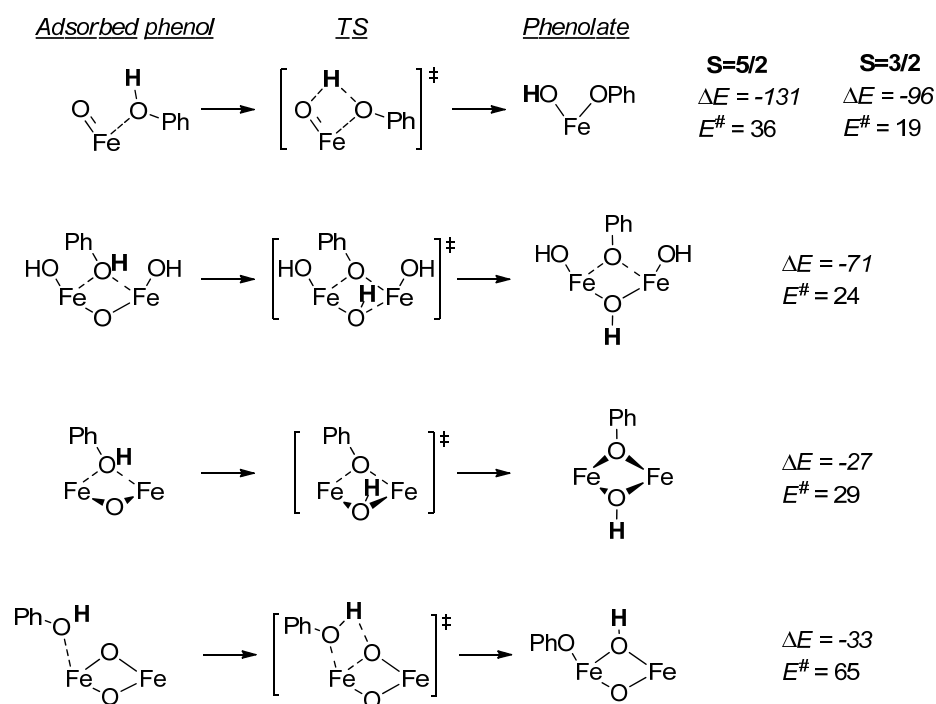


Figure 3.6. Local structure of [Fe^{II}-OC₆H₅]⁺ phenolate complex formed at δ- site.

[FeO]⁺/δ-1 site is endothermic because of repulsive interactions with the zeolite framework. When the vdW interactions are taken into account, the formation of the adsorption complex becomes more favorable ($\Delta E^{PBE+vdW}$). Consequently, the barriers for benzene oxidation are around 25 kJ/mol for both spin states ($\Delta E^{PBE+vdW}$). Likewise, the desorption energies of phenol become comparable to the values reported above for the [FeO]²⁺ site after inclusion of the dispersive interactions.

An important intermediate conclusion is that the activation barrier for benzene oxidation by the [OFeO]⁺ intermediate (~25 kJ/mol) is substantially lower than the corresponding barrier by the [FeO]²⁺ intermediate (96 kJ/mol). However, an alternative pathway leading to the deactivation of the reactive complex competes with phenol desorption. This competing path involves proton transfer from the adsorbed phenol to the adjacent terminal O ligand at the Fe³⁺ center, resulting in the formation of a [HO-Fe-OPh]⁺ hydroxyphenolate complex (Scheme 3.1). This reaction is strongly exothermic and proceeds with a low activation barrier of 36 and 19 kJ/mol for the high and low spin states, respectively. The formation of such hydroxyphenolate species stabilizes the system by 131 ($S = 5/2$) and 96 ($S = 3/2$) kJ/mol as compared to the adsorption complex of phenol with [FeO]⁺. As a result, in the case of the high-spin reaction path, the energy required for the complete regeneration of [FeO]⁺/ZSM-5 from the grafted phenolate complex exceeds 250 kJ/mol. These results imply that the benzene oxidation over mononuclear [FeO]⁺ is a stoichiometric reaction producing a highly stable grafted intermediate that blocks the catalytic process.

Note that there also exists a possibility for the dissociation of phenol over the mononuclear Fe²⁺ sites. In this case the basic O atoms from the [AlO₂]⁻ lattice units of the zeolite framework play the role of proton accepting sites. Such a dissociation results in the formation of a formally monovalent [Fe^{II}-OC₆H₅]⁺ species and a Brønsted acid site. We calculated the thermodynamics of this reaction over the Fe²⁺/δ-1 site. To minimize repulsion between two cationic species in one zeolitic ring, the acidic proton was located at a 6MR site neighboring the δ-1 site accommodating the [Fe^{II}-OC₆H₅]⁺ phenolate complex (see Figure 3.6). The reaction energy for the dissociation of phenol over the Fe²⁺/δ-1 site is



Scheme 3.1. Dissociation of adsorbed phenol and the formation of grafted phenolates on oxygenated iron complexes in ZSM-5 (reaction energies (ΔE) and activation barriers (E^\ddagger) are in kJ/mol).

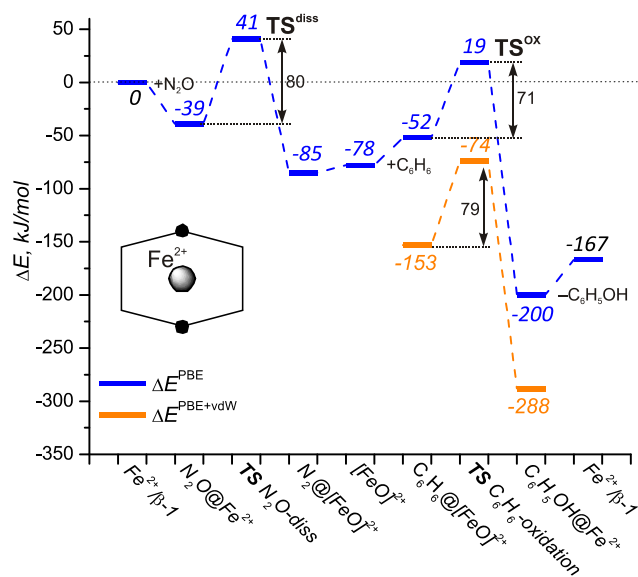


Figure 3.7. Reaction energy diagram for benzene oxidation to phenol by N_2O on mononuclear Fe^{2+} at the β -1 site of ZSM-5.

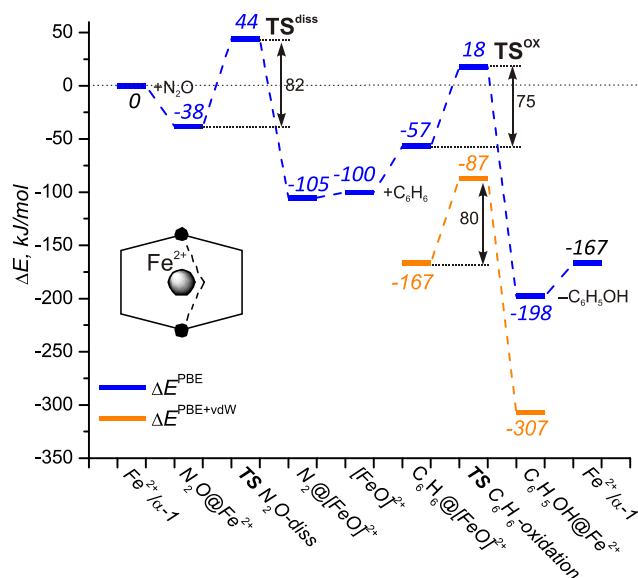


Figure 3.8. Reaction energy diagram for benzene oxidation to phenol by N_2O on mononuclear Fe^{2+} at the α -1 site of ZSM-5.

90 kJ/mol. This implies that the activation barrier will be higher than this value of 90 kJ/mol and, accordingly, this pathway can be excluded, because it significantly exceeds the interaction energy between phenol and Fe^{2+} ($E_{\text{ads}}^{\text{PBE}}$).

Benzene oxidation with N_2O over the less stable Fe^{2+} configurations β -1 and α -1 of Fe/ZSM-5 was considered in order to probe the influence of the local zeolitic environment on the catalytic reactivity of the mononuclear Fe^{2+} sites. The corresponding reaction energy diagrams are shown in Figures 3.7 and 3.8. In both cases, the coordination environment of the iron species is substantially distorted resulting in the enhancement of the Lewis acidity of the exchangeable cation. This is evident from the much strong molecular adsorption of the weakly basic N_2O reactant compared to the more stable δ -1 configuration. The calculated N_2O adsorption energies are equal to -39 kJ/mol and -38 kJ/mol, respectively, for configurations β -1 and α -1. Subsequent formation of the oxygenated iron sites via N_2O dissociation is exothermic ($\Delta E = -46$ and -67 kJ/mol for β -1 and α -1, respectively) and proceeds with an activation energy of about 80 kJ/mol in both cases. The interaction between N_2 and the product $[\text{FeO}]^{2+}$ ion is very weak.

Subsequent benzene coordination to the $[\text{FeO}]^{2+}$ species at configurations β -1 and α -1 is endothermic ($\Delta E^{\text{PBE}} = 26$ and 43 kJ/mol, respectively) according to PBE calculations. These energy losses are mainly associated with the repulsion due to the unfavorable location of the benzene molecule upon interaction of $[\text{FeO}]^{2+}$ at these sites. The specific local zeolite environment decreases the accessibility of the active site. The energy losses due to the steric repulsion are to a large extent compensated when the attractive dispersion

interactions are taken into account. After vdW correction, the adsorption energies ($\Delta E^{PBE+vdW}$) equal -67 and -75 kJ/mol, respectively for α -1 and β -1 configurations. The activation energy for the H transfer from the adsorbed benzene to the extraframework oxygen and the formation of phenol are 71 and 79 kJ/mol before and after vdW correction for the β -1 configuration, while corresponding values for the α -1 configuration are 75 and 80 kJ/mol. Phenol desorption and the regeneration of the active sites is endothermic. The vdW-corrected phenol desorption energies for Fe^{2+}/α -1 and Fe^{2+}/β -1 sites equal 140 and 121 kJ/mol, respectively.

Summarizing, activation barriers and reaction energies for benzene oxidation over mononuclear Fe^{2+} stabilized at α -1, β -1, and δ -1 sites are quite similar. This implies that the intrinsic properties of the nucleophilic oxygen species formed upon the N_2O dissociation over the exchangeable Fe^{2+} cations depend only slightly on the stability of the catalytic sites and their coordination environment. The formation of phenol on $[FeO]^+$ also proceeds with relatively low activation barrier. However, in this case, a pathway leading to deactivation by formation of a hydroxyphenolate complex is strongly favored. Direct desorption of phenol from this state is negligible.

3.3.2. Binuclear iron sites as the active site for benzene oxidation

3.3.2.1 Choice of binuclear Fe clusters

We further considered three binuclear iron complexes for benzene oxidation with N_2O , namely (i) hydroxylated $[HOFe(\mu-O)FeOH]^{2+}$, which can be readily formed by condensation of two isolated $[Fe^{III}(OH)_2]^+$ species [25, 41, 84, 85], (ii) the diamond-shaped $[Fe(\mu-O)_2Fe]^{2+}$ core resulting from the self-organization of two $[Fe^{III}O]^+$ species [86] and (iii) the mono-oxygen-bridged $[Fe(\mu-O)Fe]^{2+}$ species formed by condensation and dehydration of two $[Fe^{II}OH]^+$ ions [87, 88]. The first two complexes contain two Fe^{3+} ions, while the latter complex is composed of two Fe^{2+} cations. The binuclear Fe complexes are located at the 8MR along the sinusoidal channel of ZSM-5 (γ - site, Figure 3.1 (b)). This site has previously been considered for the stabilization of binuclear cationic species in ZSM-5 zeolite [89]. The larger size and specific shape of this site allows the formation of a favorable coordination environment around both Fe centers, resulting in the efficient stabilization of the relatively large binuclear complex. To compensate for the 2+ charge of these extraframework cationic complexes, two framework Al substitutions were introduced at T7 and T12 framework sites.

3.3.2.2 Reaction mechanism of benzene oxidation on $[HOFe(\mu-O)FeOH]^{2+}$

The optimized geometry of $[HOFe(\mu-O)FeOH]^{2+}$ at the 8MR of the ZSM-5 zeolite is shown in Figure 3.9. Each Fe cation is coordinated by four O atoms, two of which belong to the zeolite lattice. The reaction energy diagram for catalytic oxidation of benzene with N_2O over this complex is shown in Figure 3.10. The local structures of all intermediates and transition states are displayed in Figure 3.11. The initial N_2O dissociation over

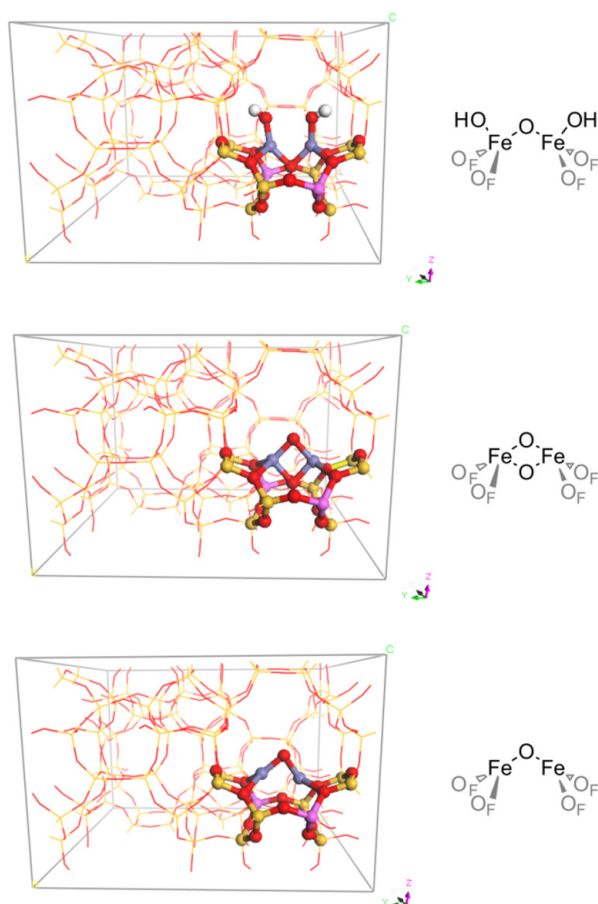


Figure 3.9. Optimized structures of $[\text{HOFe}(\mu\text{-O})\text{FeOH}]^{2+}$, $[\text{Fe}(\mu\text{-O})_2\text{Fe}]^{2+}$, and $[\text{Fe}(\mu\text{-O})\text{Fe}]^{2+}$ complexes in ZSM-5.

$[\text{HOFe}(\mu\text{-O})\text{FeOH}]^{2+}$ results in the $[\text{HOFe}(\mu\text{-O})_2\text{FeOH}]^{2+}$ complex. The activation barrier in this case is nearly twice as high as compared to the mononuclear iron sites considered above. The reaction energy is also less exothermic. The activation barrier for N_2O dissociation of 136 kJ/mol is somewhat lower than the value for a similar complex stabilized at a double 5MRs cluster model of 157 kJ/mol [41]. Subsequent benzene oxidation by the oxygenated $[\text{HOFe}(\mu\text{-O})_2\text{FeOH}]^{2+}$ complex is energetically more favorable as compared to the case of mononuclear Fe^{2+} sites. This reaction step proceeds with an activation barrier of only 31 kJ/mol and a reaction energy of -218 kJ/mol ($\Delta E^{\text{PBE+vdW}}$).

For this binuclear site it is clear that the N_2O dissociation is the rate controlling step. Thus, it can be argued that the hydroxylated $[\text{HOFe}(\mu\text{-O})\text{FeOH}]^{2+}$ complex is not relevant for the oxidation activity of Fe/ZSM-5 catalysts, because it is generally accepted that N_2O dissociation to produce the oxidizing oxygen atom is easier than the subsequent reaction

Direct benzene oxidation to phenol in Fe/ZSM-5: a comprehensive periodic DFT study

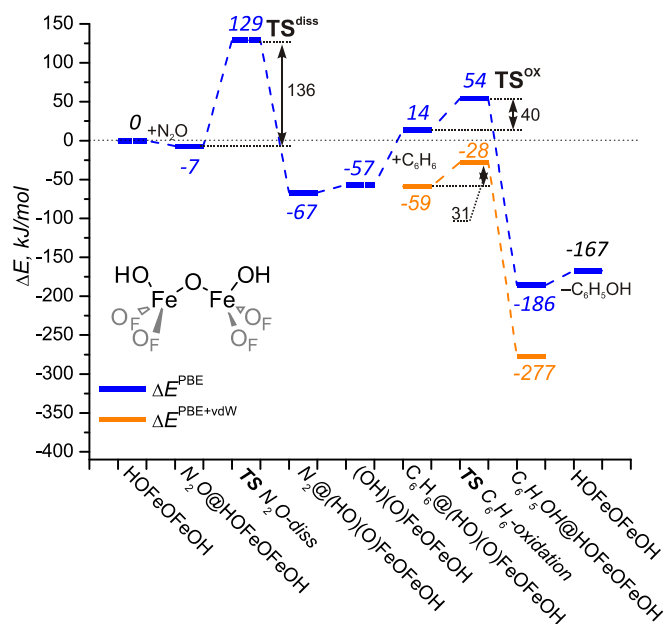


Figure 3.10. Reaction energy diagram for benzene oxidation to phenol by N_2O over a binuclear $[HOFe(\mu-O)FeOH]^{2+}$ complex in ZSM-5.

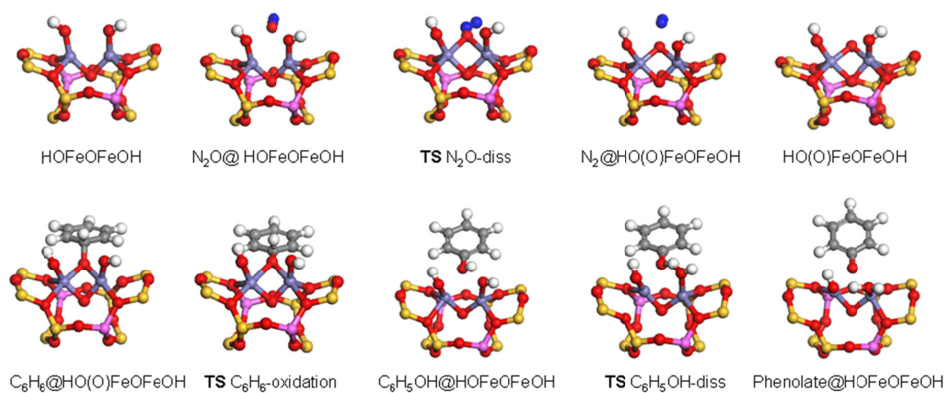


Figure 3.11. Local structures of all intermediates and transition states over binuclear $[HOFe(\mu-O)FeOH]^{2+}$.

steps. The finding that for this complex N_2O activation is difficult is in line with the cluster modeling predictions by Heyden et al [41]. In situ Raman and IR spectroscopic results also showed that the presence of H_2O on Fe/ZSM-5 leads to a decrease in the activity of N_2O decomposition, which is associated with the hydroxylation of the active dehydroxylated binuclear Fe sites to the hydroxylated structures [90].

3.3.2.3 Reaction mechanism of benzene oxidation on $[\text{Fe}(\mu\text{-O})_2\text{Fe}]^{2+}$

The di- μ -oxo-bridged diamond-shaped $[\text{Fe}(\mu\text{-O})_2\text{Fe}]^{2+}$ complex is formed upon dehydration of the $[\text{HOFe}(\mu\text{-O})\text{FeOH}]^{2+}$ complex. Water removal does not affect the formal oxidation state of the involved iron centers. The optimized structure is also included in Figure 3.9. The reaction energy diagram for the oxidation of benzene to phenol is given in Figure 3.12.

The coordination environment of the iron centers in the $[\text{Fe}(\mu\text{-O})_2\text{Fe}]^{2+}$ species is distorted resulting in their notable coordination unsaturation, and hence, enhanced Lewis acidity. Similar to the cases of $\text{Fe}^{2+}/\alpha\text{-1}$ and $\text{Fe}^{2+}/\beta\text{-1}$ discussed above, the increased Lewis acidity is evident from the substantial energy of molecular adsorption of N_2O ($E_{\text{ads}}^{\text{PBE}} = -42$ kJ/mol). The adsorbed N_2O dissociates over the $[\text{Fe}(\mu\text{-O})_2\text{Fe}]^{2+}$ site resulting in the $[\text{O-Fe}(\mu\text{-O})_2\text{Fe}]^{2+}$ complex with an activation barrier of 102 kJ/mol and a reaction energy of -36 kJ/mol. The thus formed terminal oxygen ligand is highly reactive towards benzene oxidation. The activation energies for benzene oxidation are only 26 and 15 kJ/mol before and after vdW correction, respectively. The reaction energy exceeds -200 kJ/mol. Subsequent phenol desorption is very difficult. The vdW-corrected phenol desorption energy equals 220 kJ/mol. The very strong interaction between the $[\text{Fe}(\mu\text{-O})_2\text{Fe}]^{2+}$ complex and the adsorbed phenol is due to the enhanced Lewis acidity of the coordinatively unsaturated iron centers. The local structures of all intermediates and transition states involved are shown in Figure 3.13.

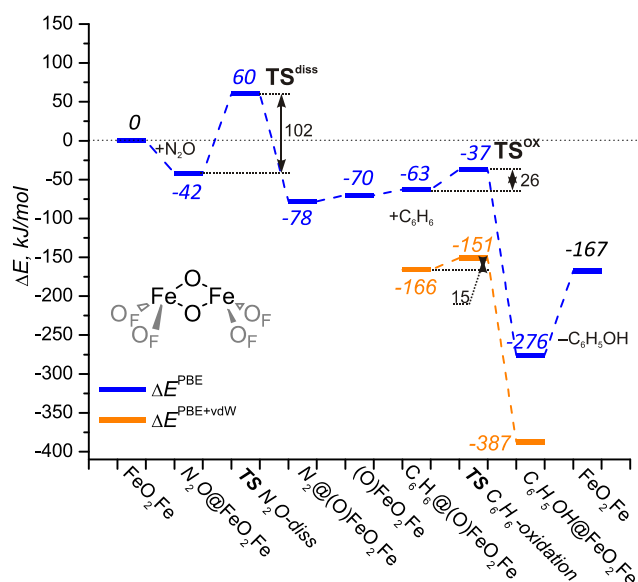


Figure 3.12. Reaction energy diagram for benzene oxidation to phenol by N_2O over a binuclear $[\text{Fe}(\mu\text{-O})_2\text{Fe}]^{2+}$ complex in ZSM-5.

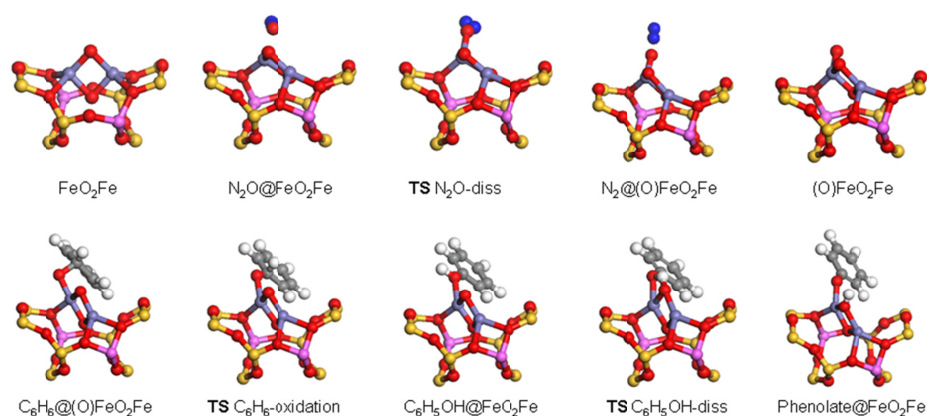


Figure 3.13. Local structures of all intermediates and transition states over binuclear $[\text{Fe}(\mu\text{-O})_2\text{Fe}]^{2+}$

3.3.2.4 Reaction mechanism of benzene oxidation on $[\text{Fe}(\mu\text{-O})\text{Fe}]^{2+}$

The reaction energy diagram for catalytic benzene oxidation by the $[\text{Fe}(\mu\text{-O})\text{Fe}]^{2+}$ complex (Figure 3.9) is shown in Figure 3.14. The local structures of all intermediates and transition states are shown in Figure 3.15. The framework oxygens of the 8MR zeolitic cation site and the bridging extraframework ligand form a distorted tetrahedral coordination site for both Fe^{2+} ions. N_2O adsorption on this site is very weak and its dissociation proceeds with a high activation barrier (116 kJ/mol). The geometry of the resulting oxygenated complex $[\text{Fe}(\mu\text{-O})_2\text{Fe}]^{2+}$ is substantially different from the structure discussed in section 3.3.2.3. Instead of the diamond-shape structure, a boat conformation of the $[\text{Fe}(\mu\text{-O})_2\text{Fe}]^{2+}$ is realized with highly reactive bridging oxygen ligands that readily oxidize benzene. This reaction step is exothermic and has low activation energy of 24 kJ/mol. The regeneration of the $[\text{Fe}(\mu\text{-O})\text{Fe}]^{2+}/\text{ZSM-5}$ structure proceeds with a reaction energy ($\Delta E^{\text{PBE}+\text{vdW}} = 143$ kJ/mol) close to that observed for the mononuclear sites.

3.3.2.5 Phenolate formation over binuclear iron sites

Similar to the case of the mononuclear $[\text{FeO}]^+$ sites, the close proximity of additional basic extraframework oxo- and hydroxy- ligands in the binuclear complexes opens a reaction path alternative to the closure of the catalytic cycle for benzene oxidation and results in the formation of grafted phenolate complexes. We investigated the required proton transfer reaction from adsorbed phenol to one of the extraframework oxygens bonded to the binuclear iron complex. The computed activation and reaction energies related to the adsorbed phenol state are summarized in Scheme 3.1. For all binuclear clusters the formation of phenolates is exothermic. The calculated activation barriers are 29 and 65 kJ/mol for the $[\text{Fe}(\mu\text{-O})\text{Fe}]^{2+}$ and $[\text{Fe}(\mu\text{-O})_2\text{Fe}]^{2+}$ sites, respectively. The energy gain due to the formation of phenolate species for these sites is about 30 kJ/mol. In the case of the hydroxylated $[\text{HOFe}(\mu\text{-O})\text{FeOH}]^{2+}$ binuclear cluster, the proton transfer from the

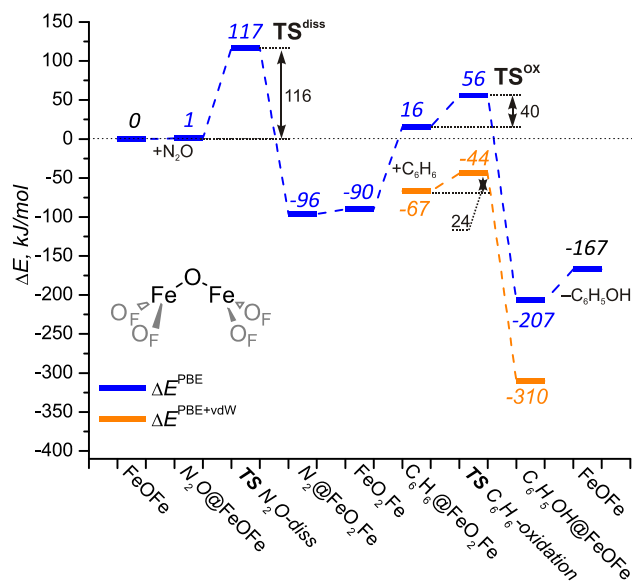


Figure 3.14. Reaction energy diagram for benzene oxidation to phenol by N_2O over a binuclear $[\text{Fe}(\mu\text{-O})\text{Fe}]^{2+}$ complex in ZSM-5.

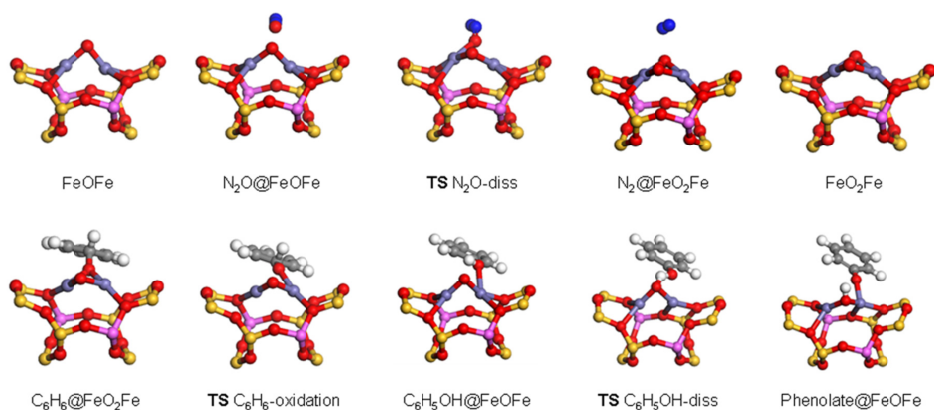


Figure 3.15. Local structures of all intermediates and transition states over binuclear $[\text{Fe}(\mu\text{-O})\text{Fe}]^{2+}$.

adsorbed phenol to hydroxyl ligand proceeds with a low activation barrier of 24 kJ/mol and stabilizes the final complex by 71 kJ/mol. Thus, the regeneration of the binuclear iron sites upon the catalytic benzene oxidation via phenol desorption is blocked because of the formation of grafted phenolate species. This deactivation path is exothermic and proceeds with low activation barriers over all binuclear sites considered here.

3.4. Discussion

The catalytic cycle for benzene oxidation to phenol with nitrous oxide involves the dissociative adsorption of N_2O to form an extraframework oxygen species followed by the oxidation of benzene to phenol. The activation barriers for the oxygenation of the mononuclear Fe^{2+} species at various zeolitic sites lie between 59 ($Fe^{2+}/\delta-1$) and 82 ($Fe^{2+}/\alpha-1$) kJ/mol. These values are close to those computed for isolated Fe^{2+} ions in a periodic model ferrierite [48].

Alternative mononuclear Fe^{3+} and binuclear Fe^{2+} and Fe^{3+} complexes are generally less reactive for the initial dissociative adsorption of N_2O . Whereas in the case of $[FeO]^+$ at the $\delta-1$ site, the calculated activation barrier for N_2O dissociation only slightly exceeds that for $Fe^{2+}/\delta-1$ and lies in the range of 73-94 kJ/mol depending on the spin state, the barriers for the binuclear ferric complexes are much higher: 116, 102, and 136 kJ/mol for $[Fe(\mu-O)Fe]^{2+}$, $[Fe(\mu-O)_2Fe]^{2+}$, and $[HOFe(\mu-O)FeOH]^{2+}$, respectively. The activation barrier for $[HOFe(\mu-O)FeOH]^{2+}$ is the highest among the complexes considered in this study. This is in line with the trends found by Hansen et al. [41] and Xia et al [90]. The iron ions in the binuclear complexes form a (distorted) tetrahedral coordination environment with the framework and extraframework oxygen ions. The introduction of an additional oxygen ligand into their first coordination sphere upon N_2O dissociation is associated with substantial structural perturbations. This decreases the reactivity of the binuclear iron complexes compared to the mononuclear species, in which an open coordination is readily available for the dissociating N_2O molecule.

Concerning the first step (dissociative adsorption of N_2O) we compared the reaction energies for the reaction $N_2O + Fe^{2+} \rightarrow [FeO]^{2+} + N_2$ to the stabilities of Fe^{2+} at the zeolite lattice. Benco et al. have argued that the stability of a cation and its reactivity – in that case towards NO – can be related to the Lewis acidity of the cation [91]. It is generally believed that less stable sites exhibit a higher reactivity [92, 93]. In our case no clear correlation was found between the reaction energy for N_2O dissociation and the relative stability of the Fe^{2+} site. Whereas the reaction energy for the most stable $\delta-1$ configuration equals -57 kJ/mol, it is only 9 kJ/mol more exothermic for the D-4 site, which is less stable by 200 kJ/mol. This suggests that the local coordination environment has only a minor effect on the reactivity of Fe^{2+} .

The most important conclusion of this part is that the initial dissociative adsorption of N_2O to form a reactive extraframework oxygen atom proceeds with a relatively moderate barrier (60-90 kJ/mol) for isolated Fe^{2+} and FeO^+ with a preference for the isolated ferrous ions. The barriers are higher for binuclear iron complexes. In support of these findings are experimental data showing that N_2O dissociation occurs at relatively low temperature. This property has been used to titrate the density of Fe^{2+} sites in Fe/ZSM-5 sites [13]. One should note that the catalytic N_2O decomposition involves recombination of extraframework O atoms formed upon the dissociative adsorption of N_2O . This process is easier over the binuclear sites. In this case, the formation of O_2 is the rate limiting step

and it proceeds with higher barriers. The catalytic decomposition of N_2O therefore requires higher reaction temperatures compared to benzene oxidation [28].

Inspection of the reaction energy diagrams of the complete catalytic cycles for benzene oxidation over the most stable Fe^{2+} locations at δ -1, α -1, and β -1 sites (Figures 3.2, 3.7 and 3.8) indicates that the activation barriers for N_2O dissociation and benzene oxidation are very close. The most pronounced difference in the catalytic behavior of Fe^{2+} at δ -1, α -1, and β -1 configurations is the stabilization of benzene and phenol at these sites that becomes apparent after considering the vdW corrections. The unfavorable confinement of benzene close to the Fe^{2+}/α -1 and Fe^{2+}/β -1 sites destabilizes the reaction intermediates and lowers the desorption energy of phenol and, accordingly, favors the closure of the catalytic cycle. Despite these differences between the 6MR exchange sites, it turns out that the overall barrier only slightly depends on the coordination of Fe^{2+} to the zeolite.

For all the alternative catalytic sites the kinetic parameters for benzene hydroxylation and phenol desorption are found to be very comparable to the values for isolated Fe^{2+} . Binuclear iron complexes in their oxygenated states oxidize benzene with very low activation barriers of 15-30 kJ/mol (Figures 3.10, 3.12, 3.14). However, the initial N_2O dissociation step is more difficult for these binuclear complexes suggesting that they are most likely not involved in benzene oxidation. Nevertheless, it is not possible to completely exclude the contribution of mononuclear $[\text{FeO}]^+$ or binuclear Fe^{2+} and Fe^{3+} sites for oxidation of benzene to phenol. An important reason to exclude them as potential catalytic reaction centers turns out to be the presence of at least one additional extraframework basic oxygen anion that can act as a proton acceptor. This extra oxygen ligand opens an alternative reaction pathway that may lead to deactivation of the active site. Indeed, in all these cases the OH group of adsorbed phenol can heterolytically dissociate over the $\text{Fe}^{\delta+}\cdots\text{O}^{\delta-}$ acid base pair yielding a phenolate species ($\text{C}_6\text{H}_5\text{O}^-$) and an OH group grafted to iron sites. This reaction is thermodynamically favored and proceeds with very low activation energies for all sites containing extraframework oxygen species (Scheme 3.1). The formation of such a stable phenolate intermediate is more favorable than the regeneration of the extraframework iron-complexes. The formation of Fe(III)-phenolate complex was also evidenced in a combined UV-Vis and Raman study [19]. Dissociation of phenol over the isolated exchangeable Fe^{2+} sites is strongly disfavored thermodynamically. Accordingly, it is reasonable to suggest that despite the competing reactivity of $[\text{FeO}]^+$ and oxygen/hydroxy-bridged binuclear $\text{Fe}^{2+}/\text{Fe}^{3+}$ complexes these sites deactivate due to irreversible adsorption of a phenolate complex following benzene oxidation. The thus formed grafted hydrocarbon species can play a role of the intrazeolitic coke precursors and substantially decrease the accessibility of the zeolitic voids. This deactivating reaction pathway is not possible for the isolated Fe^{2+} ions.

3.5. Conclusion

A comprehensive DFT study on the reactivity of ferrous and ferric ions in a periodic ZSM-5 model has been carried out. The intrinsic reactivity of the Fe²⁺ in ZSM-5 zeolite in the catalytic oxidation of benzene to phenol with N₂O depends only slightly on the local coordination environment of the ferrous ion. The confinement effect exerted by the zeolite cage on the hydrocarbon reactant and product in the vicinity of Fe²⁺ affects the reaction energy diagram. Such steric constraints lead to more facile desorption of phenol and regeneration of the active Fe²⁺ site. Accordingly, the most preferred catalytic pathway is the oxidation of benzene to phenol catalyzed by Fe²⁺ at the α - and β - sites.

Oxygen-containing mono- and binuclear Fe²⁺ and Fe³⁺ complexes are also potential sites for the formation of phenol, although the initial formation of the reactive oxygen atom via the dissociation adsorption of N₂O is considerably less favorable for the binuclear complexes. The overall reaction is however not catalytic because of the presence of highly basic oxygen ligands in the active Fe complexes. These basic oxygen anions favor dissociation of adsorbed phenol as compared to desorption, leading to the formation of stable phenolates that are difficult to desorb under practical conditions.

References

- [1] K.A. Dubkov, V.I. Sobolev, E.P. Talsi, M.A. Rodkin, N.H. Watkins, A.A. Shteinman, G.I. Panov. *J. Mol. Catal. A: Chem* 123 (1997) 155-161.
- [2] E.J.M. Hensen, Q. Zhu, R.A. van Santen. *J. Catal.* 220 (2003) 260.
- [3] L.V. Pirutko, V.S. Chernyavsky, A.K. Uriarte, G.I. Panov. *Appl. Catal. A: Gen.* 227 (2002) 143-157.
- [4] P. Kubanek, B. Wichterlova, Z. Sobalik. *J. Catal.* 211 (2002) 109-118.
- [5] E.J.M. Hensen, Q.J. Zhu, P.-H. Liu, K.-J. Chao, R.A. van Santen. *J. Catal.* 226 (2004) 466-470.
- [6] G.I. Panov, A.S. Kharitonov, V.I. Sobolev. *Appl. Catal. A: Gen.* 98 (1993) 1-20.
- [7] S.H. Choi, B.R. Wood, J.A. Ryder, A.T. Bell. *J. Phys. Chem. B* 107 (2003) 11843-11851.
- [8] J.F. Jia, K.S. Pillai, W.M.H. Sachtler. *J. Catal.* 221 (2004) 119-126.
- [9] E.J.M. Hensen, Q. Zhu, R.A.J. Janssen, P. Magusin, P.J. Kooyman, R.A. van Santen. *J. Catal.* 233 (2005) 123-132.
- [10] E.J.M. Hensen, Q. Zhu, R.A. van Santen. *J. Catal.* 233 (2005) 136-146.
- [11] K. Yoshizawa, Y. Shiota, T. Yamabe. *J. Am. Chem. Soc.* 121 (1999) 147-153.
- [12] G. Marban, T. Valdes-Solis, A.B. Fuertes. *J. Catal.* 226 (2004) 138-155.
- [13] K.A. Dubkov, N.S. Ovanesyan, A.A. Shteinman, E.V. Starokon, G.I. Panov. *J. Catal.* 207 (2002) 341-351.
- [14] V.S. Chemyavsky, L.V. Pirutko, A.K. Uriarte, A.S. Kharitonov, G.I. Panov. *J. Catal.* 245 (2007) 466-470.
- [15] R. Joyner, M. Stockenhuber. *J. Phys. Chem. B* 103 (1999) 5963-5976.
- [16] S.H. Choi, B.R. Wood, A.T. Bell, M.T. Janicke, K.C. Ott. *J. Phys. Chem. B* 108 (2004) 8970-8975.
- [17] L.J. Lobree, I.C. Hwang, J.A. Reimer, A.T. Bell. *J. Catal.* 186 (1999) 242-253.
- [18] J. Perez-Ramirez, M.S. Kumar, A. Bruckner. *J. Catal.* 223 (2004) 13-22.
- [19] H. Xia, K. Sun, K. Sun, Z. Feng, W.X. Li, C. Li. *J. Phys. Chem. C* 112 (2008) 9001-9005.
- [20] A.A. Battiston, J.H. Bitter, D.C. Koningsberger. *Catal. Lett.* 66 (2000) 75-79.
- [21] A.A. Battiston, J.H. Bitter, F.M.F. de Groot, A.R. Overweg, O. Stephan, J.A. van Bokhoven, P.J. Kooyman, C. van der Spek, G. Vank, D.C. Koningsberger. *J. Catal.* 213 (2003) 251-271.
- [22] A.A. Battiston, J.H. Bitter, W.M. Heijboer, F.M.F. de Groot, D.C. Koningsberger. *J. Catal.* 215 (2003) 279-293.
- [23] A.A. Battiston, J.H. Bitter, D.C. Koningsberger. *J. Catal.* 218 (2003) 163-177.
- [24] P. Marturano, L. Drozdov, A. Kogelbauer, R. Prins. *J. Catal.* 192 (2000) 236-247.
- [25] P. Marturano, L. Drozdova, G.D. Pirngruber, A. Kogelbauer, R. Prins. *Phys. Chem. Chem. Phys.* 3 (2001) 5585-5595.

- [26] J.F. Jia, Q. Sun, B. Wen, L.X. Chen, W.M.H. Sachtler. *Catal. Lett.* 82 (2002) 7-11.
- [27] H. Xia, K. Sun, Z. Liu, Z. Feng, P. Ying, C. Li. *J. Catal.* 270 (2010) 103-109.
- [28] K. Sun, H. Xia, Z. Feng, R. van Santen, E. Hensen, C. Li. *J. Catal.* 254 (2008) 383-396.
- [29] H. Xia, K. Sun, F. Fan, K. Sun, W. Su, Z. Feng, P. Ying, C. Li. *J. Catal.* 259 (2008) 269-275.
- [30] H. Xia, S.D. Fleischman, C. Li, S.L. Scott. *J. Phys. Chem. Lett.* 2 (2011) 190-195.
- [31] Y. Li, H. Xia, F. Fan, Z. Feng, R.A. van Santen, E.J.M. Hensen, C. Li. *Chem. Commun.* 6 (2008) 774-776.
- [32] G.D. Pirngruber, P.K. Roy, R. Prins. *Phys. Chem. Chem. Phys.* 8 (2006) 3939-3950.
- [33] A. Zecchina, M. Rivallan, G. Berlier, C. Lamberti, G. Ricchiardi. *Phys. Chem. Chem. Phys.* 9 (2007) 3483-3499.
- [34] J. Perez-Ramirez, G. Mul, F. Kapteijn, J.A. Moulijn, A.R. Overweg, A. Domenech, A. Ribera, I. Arends. *J. Catal.* 207 (2002) 113-126.
- [35] A.A. Battiston, J.H. Bitter, D.C. Koningsberger. *J. Catal.* 218 (2003) 163-177.
- [36] J.A. Ryder, A.K. Chakraborty, A.T. Bell. *J. Phys. Chem. B* 106 (2002) 7059-7064.
- [37] J.A. Ryder, A.K. Chakraborty, A.T. Bell. *J. Catal.* 220 (2003) 84-91.
- [38] A. Heyden, B. Peters, A.T. Bell, F.J. Keil. *J. Phys. Chem. B* 109 (2005) 1857-1873.
- [39] A. Heyden, A.T. Bell, F.J. Keil. *J. Catal.* 233 (2005) 26-35.
- [40] A.L. Yakovlev, G.M. Zhidomirov, R.A. van Santen. *J. Phys. Chem. B* 105 (2001) 12297-12302.
- [41] N. Hansen, A. Heyden, A.T. Bell, F.J. Keil. *J. Phys. Chem. C* 111 (2007) 2092-2101.
- [42] N. Hansen, A. Heyden, A.T. Bell, F.J. Keil. *J. Catal.* 248 (2007) 213-225.
- [43] L. Kiwi-Minsker, D.A. Bulushev, A. Renken. *J. Catal.* 219 (2003) 273-285.
- [44] L. Kiwi-Minsker, D.A. Bulushev, A. Renken. *Catal. Today* 91-2 (2004) 165-170.
- [45] L. Kiwi-Minsker, D.A. Bulushev, A. Renken. *Catal. Today* 110 (2005) 191-198.
- [46] H. Guesmi, D. Berthomieu, L. Kiwi-Minsker. *J. Phys. Chem. C* 112 (2008) 20319-20328.
- [47] H. Guesmi, D. Berthomieu, B. Bromley, B. Coq, L. Kiwi-Minsker. *Phys. Chem. Chem. Phys.* 12 (2010) 2873-2878.
- [48] S. Sklenak, P.C. Andrikopoulos, B. Boekfa, B. Jansang, J. Novakova, L. Benco, T. Bucko, J. Hafner, J. Dedecek, Z. Sobalik. *J. Catal.* 272 (2010) 262-274.
- [49] K. Yoshizawa, Y. Shiota, T. Yumura, T. Yamabe. *J. Phys. Chem. B* 104 (2000) 734-740.
- [50] N.A. Kachurovskaya, G.M. Zhidomirov, R.A. van Santen. *J. Phys. Chem. B* 108 (2004) 5944-5950.
- [51] M.F. Fella, I. Onal. *Turkish J. Chem.* 33 (2009) 333-345.
- [52] M.F. Fella, R.A. van Santen, I. Onal. *J. Phys. Chem. C* 113 (2009) 15307-15313.
- [53] M.F. Fella, I. Onal, R.A. van Santen. *J. Phys. Chem. C* 114 (2010) 12580-12589.
- [54] L. Benco, T. Bucko, J. Hafner. *J. Phys. Chem. C* 113 (2009) 18807-18816.
- [55] N. Hansen, T. Kerber, J. Sauer, A.T. Bell, F.J. Keil. *J. Am. Chem. Soc.* 132 (2010) 11525-11538.
- [56] S. Svelle, C. Tuma, X. Rozanska, T. Kerber, J. Sauer. *J. Am. Chem. Soc.* 131 (2009) 816-825.
- [57] I.L.C. Buurmans, E.A. Pidko, J.M. de Groot, E. Stavitski, R.A. van Santen, B.M. Weckhuysen. *Phys. Chem. Chem. Phys.* 12 (2010) 7032-7040.
- [58] E. Stavitski, E.A. Pidko, M.H.F. Kox, E.J.M. Hensen, R.A. van Santen, B.M. Weckhuysen. *Chem. Eur. J.* 16 (2010) 9340-9348.
- [59] G. Kresse, J. Hafner. *Phys. Rev. B* 48 (1993) 13115-13118.
- [60] G. Kresse, J. Hafner. *Phys. Rev. B* 49 (1994) 14251-14269.
- [61] G. Kresse, J. Furthmuller. *Comput. Mater. Sci.* 6 (1996) 15-50.
- [62] G. Kresse, J. Furthmuller. *Phys. Rev. B* 54 (1996) 11169-11186.
- [63] P.E. Blochl. *Phys. Rev. B* 50 (1994) 17953-17979.
- [64] G. Kresse, D. Joubert. *Phys. Rev. B* 59 (1999) 1758-1775.
- [65] J.P. Perdew, K. Burke, M. Ernzerhof. *Phys. Rev. Lett.* 77 (1996) 3865-3868.
- [66] H.J. Monkhorst, J.D. Pack. *Phys. Rev. B* 13 (1976) 5188-5192.
- [67] H. van. *Acta Crystallogr. Sect. B* 46 (1990) 731-735.
- [68] C. Baerlocher, L.B. McCusker, Database of Zeolite Structures. <http://www.iza-structure.org/databases/>.
- [69] G. Mills, H. Jonsson, G.K. Schenter. *Surf. Sci.* 324 (1995) 305-337.
- [70] D.H. Kitson, A.T. Hagler. *Biochem.* 27 (1988) 7176-7180.
- [71] P. Dauberoguthorpe, V.A. Roberts, D.J. Osguthorpe, J. Wolff, M. Genest, A.T. Hagler. *Proteins Struct. Funct. Genet.* 4 (1988) 31-47.
- [72] T. Demuth, L. Benco, J. Hafner, H. Toulhoat, F. Hutschka. *J. Chem. Phys.* 114 (2001) 3703-3712.
- [73] A.M. Vos, X. Rozanska, R.A. Schoonheydt, R.A. van Santen, F. Hutschka, J. Hafner. *J. Am. Chem. Soc.* 123 (2001) 2799-2809.
- [74] J.D. Z Gale. *Kristall.* 220 (2005) 552.
- [75] T.J. Hou, L.L. Zhu, X.J. Xu. *J. Phys. Chem. B* 104 (2000) 9356-9364.

- [76] H. Jobic, H. Ramanan, S.M. Auerbach, M. Tsapatsis, P. Fouquet. *Microporous Mesoporous Mater.* 90 (2006) 307-313.
- [77] E.A. Pidko, R.A. van Santen, *Zeolites and Catalysis: Synthesis, Reactions and Applications*, Wiley-VCH Verlag GmbH & Co. KGaA, 2010.
- [78] Q. Zhu, B. L. Mojet, R. A. Janssen, E. J. M. Hensen, J. van Grondelle, P. Magusin, R. A. van Santen. *Catal. Lett.* 81 (2002) 205-212.
- [79] Y. Shiota, K. Suzuki, K. Yoshizawa. *Organometallics* 25 (2006) 3118-3123.
- [80] W. Z. Liang, A. T. Bell, M. Head-Gordon, A. K. Chakraborty. *J. Phys. Chem. B* 108 (2004) 4362.
- [81] C. R. F. Lund. *J. Catal.* 243 (2006) 438-441.
- [82] B. R. Wood, J. A. Reimer, A. T. Bell, M. T. Janicke, K. C. Ott. *J. Catal.* 224 (2004) 148-155.
- [83] M. F. Fellah, R. A. van Santen, I. Onal. *J. Phys. Chem. C* 113(2009) 15307-15313.
- [84] E. M. El-Malki, R. A. van Santen, W. M. H. Sachtler. *J. Phys. Chem. B* 103(1999) 4611-4622.
- [85] H.-Y. Chen, W. M. H. Sachtler. *Catal. Today* 42 (1998) 73-83.
- [86] K. Yoshizawa, Y. Shiota, T. Yumura, T. Yamabe. *J. Phys. Chem. B* 104 (2000) 734-740.
- [87] A. Heyden, N. Hansen, A. T. Bell, F. J. Keil. *J. Phys. Chem. B* 110 (2006) 17096-17114.
- [88] M.J. Rice, A. K. Chakraborty, A. T. Bell. *J. Phys. Chem. B* 104 (2000) 9987-9992.
- [89] E. J. M. Hensen, E. A. Pidko, N. Rane, R. A. van Santen. *Angew. Chem. Int. Ed.* 46 (2007) 7273-7276.
- [90] H. Xia, K. Sun, Z. Feng, C. Li. *J. Phys. Chem. C* 115 (2011) 542-548.
- [91] L. Benco, T. Bucko, R. Grybos, J. Hafner, Z. Sobalik, J. Dedecek, J. Hrusak. *J. Phys. Chem. C* 111 (2007) 579-586.
- [92] E.A. Pidko, V.B. Kazansky, E.J.M. Hensen, R.A. van Santen. *J. Catal.* 240 (2006) 73-84.
- [93] L. Benco, T. Bucko, J. Hafner, H. Toulhoat. *J. Phys. Chem. B* 109 (2005) 20361-20369.



CHAPTER 4

CATALYTIC PROPERTIES OF EXTRAFRAMEWORK IRON- CONTAINING SPECIES IN ZSM-5 FOR N₂O DECOMPOSITION

The reactivity of mononuclear and binuclear iron-containing complexes in ZSM-5 zeolite for catalytic N₂O decomposition has been investigated by periodic DFT calculations and micro kinetic modeling. It is demonstrated that the catalytic reaction over mononuclear isolated Fe²⁺ and [FeO]⁺ sites is hampered by the high barriers (>180 kJ/mol) for the activation of the second N₂O molecule necessary to complete the catalytic cycle. The catalytic cycles for N₂O decomposition over binuclear [Fe(μ-O)Fe]²⁺ and [Fe(μ-O₂)Fe]²⁺ species are interconnected. The structures may interconvert in the course of the catalytic reaction. Because the coordination of iron centers is changing along with the reaction coordination, the most stable electronic state for different reaction intermediates corresponds to different spin states. The change of spin multiplicities along the minimum energy path is one of the prominent features which facilitate the O₂ formation and evolution at the end of the reaction. Both O₂ desorption and N₂O dissociation can be the rate-limited steps depending on reaction mechanism and the catalytic sites. Based on DFT results, a micro kinetic model was constructed. It is shown that at low temperature the surface is dominated by the oxidized [Fe(μ-O)₂FeO]²⁺ species, whereas at the higher temperatures both [Fe(μ-O)₂Fe]²⁺ and [Fe(μ-O)Fe]²⁺ species are present. This indicates that both reaction paths proposed in the text take place under the actual catalytic conditions and compete with each other. The apparent activation energy equals 106 kJ/mol at 723 K. The reaction order with respect to N₂O partial pressure is dependent sensitively on reaction temperature.

4.1. Introduction

Fe/ZSM-5 zeolite is among the most active non-noble metal-containing catalysts capable of promoting such a reaction [1]. These considerations have inspired a high interest in the past decade in identifying the nature of the active site and the reaction mechanism for N₂O decomposition over Fe/ZSM-5 catalysts [2-4]. Nevertheless, despite the apparent simplicity of the reaction, these issues are still under debate [1, 5-15].

Most experimental and theoretical studies indicated that the reaction rate is first order in N₂O partial pressure and zero order in O₂ partial pressure. Both N₂O dissociation and oxygen desorption from the active site have been suggested as the rate-limited step [16-22]. The migration and recombination of surface oxygen species have been proposed to be the rate-limited step by several experimental steady-state kinetic studies [9, 18, 23, 24]. However, the results of a computational study by Bell et al. suggested that the rate of N₂O dissociation determines the overall rate of the catalytic process [21, 22]. Very recently, Kiwi-Minsker et al. demonstrated through a complementary computational and experimental study that the rate-limiting step depends actually on the reaction temperature. Whereas at low temperature O₂ desorption is the most difficult step, above 700 K the N₂O dissociation becomes rate-limiting [13, 25].

The catalytic properties of Fe/ZSM-5 catalysts are related to the iron-containing species distributed in the micropores of ZSM-5 zeolite. However, because of the high heterogeneity of the catalytic materials and the fact that only a fraction of iron sites actively participates in the catalytic reaction, the unambiguous identification of the nuclearity, chemical composition and oxidation state of the iron centers in the intrazeolitic reactive complex is a challenge [12, 18, 26-34].

Both mono- [3, 7, 12, 35, 36] and binuclear [17, 37-41] Fe sites have been proposed as the active sites for N₂O decomposition. At low iron loading in the catalyst, isolated iron species at cation-exchange positions present in the form of Fe²⁺ [20, 29, 42], [FeO]⁺ [4, 22], and [Fe(OH)₂]⁺ [7, 35, 43] have been considered as reactive complexes. The interactions of NO and N₂O probes with activated Fe/ZSM-5 provide evidence of two families of mononuclear Fe^{II} centers differing in the coordination state of Fe [44]. Sklenak et al. proposed that the cooperative action of two exchangeable Fe²⁺ cations is essential for the high reactivity of Fe-containing zeolites in N₂O decomposition [45]. The reaction mechanism and the kinetic parameters of N₂O decomposition over Fe^{III}-containing isolated [FeO]⁺ and [Fe(OH)₂]⁺ complexes have been studied by Heyden et al using DFT cluster modeling approach and transition state theory [22, 43, 46, 47]. The computed apparent activation energies range between 109 kJ/mol and 231 kJ/mol depending on the water content in the reaction feed. In line with these theoretical considerations, Pérez-Ramírez et al. concluded that steam-activated zeolite containing mostly isolated Fe³⁺ ions at extraframework sites shows the highest activity per mole of iron, while the highly clustered liquid-ion-exchanged catalyst presents the lowest activity [48].

On the other hand, Sachtler et al. discovered that the rate of N₂O decomposition increased dramatically along with the Fe loading, indicating the importance of multinuclear Fe sites for the reactivity [17]. This is in line with the results of EXAFS measurements reported by Prins et al. [28] and Koningsberger et al. [49]. By the transient response method, steady-state kinetics, and in situ IR and Raman results, N₂O decomposition was investigated by Xia et al [50-52]. The dehydroxylated binuclear Fe-peroxo complex with a characteristic Raman band at 867 cm⁻¹ was proposed as an intermediate during N₂O decomposition. The DFT reaction energy profile of N₂O decomposition over binuclear Fe complexes was reported for the first time by van Santen and co-workers [53]. It was shown that, at low temperature, trace amount of water results in inactive hydroxylated Fe sites on Fe/ZSM-5 [17, 19, 36, 51, 54]. These findings cohere well with the results of DFT studies reporting very high activation barriers of N₂O decomposition over such hydroxylated iron complexes [21, 22, 55, 56].

In this Chapter a continuation of the computational studies devoted to the investigation of structure and reactivity of Fe/ZSM-5 catalyst is presented. The mechanism of catalytic N₂O decomposition over the dominant binuclear [Fe(μ -O)Fe]²⁺ and [Fe(μ -O)₂Fe]²⁺ is studied by means of DFT calculations and micro kinetic modeling. The reactivity of the binuclear sites is compared to that of the alternative mononuclear species.

4.2. Computational details

All the DFT calculations were performed using the Vienna *ab initio* Simulation Package (VASP). The same parameters of unit cell, geometric optimizations, transition state search, and frequency analysis were used as previous demonstrated in Chapter 3.

To model the transient behavior and temperature of the species in our system, we used micro-kinetic modeling. Within this approach, the reaction rate for each elementary reaction step is expressed using the Arrhenius formula:

$$r = \nu \cdot \exp\left(\frac{-E_a}{k_b T}\right) \prod_i c_i \quad (4-1)$$

where ν stands for the pre-exponential factor, E_a the electronic energy difference between the initial state and the transition state (i.e. the electronic activation energy), k_b the Boltzmann constant and T the temperature. The pre-exponential factor and the exponent are multiplied with the product of the species in the initial state to obtain the rate.

For the pre-exponential factor we used $\nu = \frac{k_b T}{h} \approx 10^{13}$ with the exception for adsorption and desorption reactions, where either a much lower or higher value is used to account for the change in entropy when transferring a species either from or to the gas phase. The activation energies were obtained using DFT simulations and resemble the electronic energy differences between initial and final state. Note that we did not modify the

activation energies to include zero point energy corrections.

For a system with N elementary reactions steps, one obtains $2N$ equations like eq. 4.1. The change of a particular species or compound over time is expressed via the equation

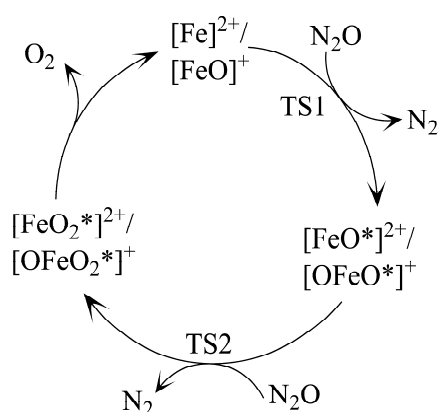
$$\frac{dc_i}{dt} = \sum_j r_j^+ - r_j^- \quad (4-2)$$

where $\frac{dc_i}{dt}$ is the change in the concentration of species i over time and r_j is the reaction rate of species i in elementary reaction step j . Note that when species i is a reagents (r_j^-), the reaction rate is subtracted, while in the case species i is a product (r_j^+), the rate is added to the total rate. All rates r_j are per definition taken as positive values. For a total of N compounds, N ordinary differential equations are obtained via the above procedure which can be solved using N boundary conditions which are the concentrations of species i at time $t = 0$.

4.3. Results

4.3.1. Reaction mechanism of N_2O decomposition over isolated Fe^{2+}

The isolated Fe^{2+} ion has been frequently proposed as the active site for direct N_2O decomposition. According to the results presented in Chapter 2, the most favorable location of isolated Fe^{2+} in ZSM-5 is δ -1 site with symmetrically arranged framework Al ions within six-membered ring (6MR) at the intersection of straight and zigzag channels [57]. The alternative 6MR α -1 and β -1 sites are less stable than δ -1 site by 64 and 36 kJ/mol, respectively. These configurations were considered as the potential active sites in the direct N_2O decomposition to understand the effect of local zeolite environment on reactivity of isolated Fe^{2+} sites.



Scheme 4.1. Possible reaction paths for direct N_2O decomposition over mononuclear Fe^{2+} and $[FeO]^+$.

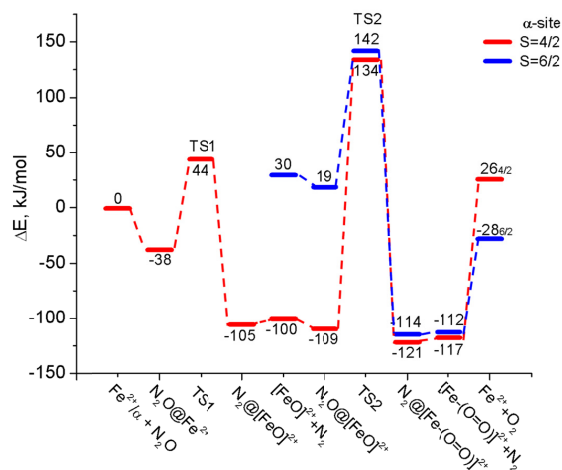


Figure 4.1. Reaction energy profile of N₂O decomposition over isolated Fe²⁺@ α -1 site. Both low-spin state ($S = 4/2$) and high-spin state ($S = 6/2$) are indicated.

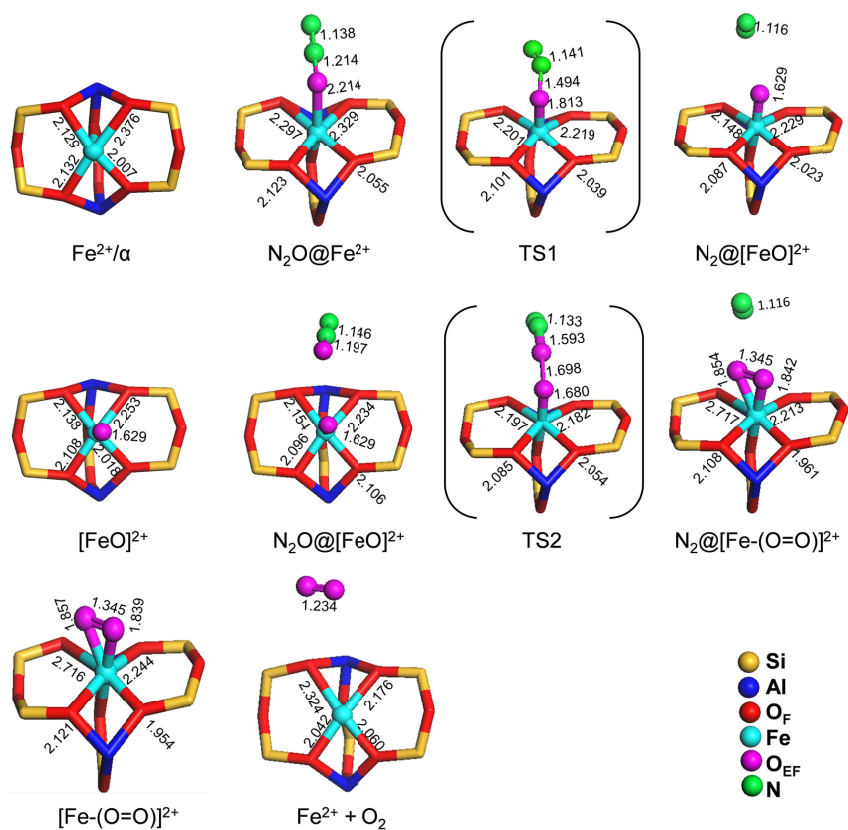


Figure 4.2. Selected interatomic distances of the intermediates and transition state structures involved in N₂O decomposition over Fe²⁺@ α -1 site.

The proposed reaction mechanisms over mononuclear site are presented in Scheme 4.1. Figure 4.1 shows the reaction energy diagram of N₂O decomposition over isolated Fe²⁺ site at 6MR of the α - site. The local structures and geometric parameters of reaction intermediates and transition states are summarized in Figure 4.2. The adsorption of first N₂O molecule on Fe²⁺ is energetically favorable ($\Delta E^{ads} = -38$ kJ/mol). Nitrous oxide interacts with the Fe center via oxygen atom forming a Fe–O_{EF} (O_{EF} = extraframework oxygen atom) coordination bond with a length of 2.214 Å. Subsequent dissociation of the N–O bond generates a [FeO]²⁺ species and molecular N₂. This step is thermodynamically favorable ($\Delta E = -67$ kJ/mol) and proceeds with an activation energy ($\Delta E^{\ddagger TS1}$) of 82 kJ/mol. The desorption of N₂ from the active center and formation of bare [FeO]²⁺ is only slightly endothermic. The transition state of N–O bond dissociation is a twisted N–N–O species with elongated N–O bond coordinated to the Fe center (Figure 4.2). The Fe–O_{EF} bond is being formed at this step ($r = 1.813$ Å). After the N–O bond is cleaved, the bond length of Fe–O_{EF} is 1.629 Å.

The next step involves the dissociation of a second N₂O molecule by the [FeO]²⁺ species. The reaction mechanism is different from the one discussed above. In this case, N₂O physically adsorbs ($\Delta E^{ads} = -9$ kJ/mol) to the terminal oxygen atom rather than to the iron center. The subsequent dissociation reaction proceeds with a very high barrier ($\Delta E^{\ddagger TS2} = 243$ kJ/mol). The reaction is only slightly exothermic ($\Delta E = -12$ kJ/mol). The low reactivity of [FeO]²⁺ is due to the quite stable square bipyramidal configuration of Fe²⁺ formed with adjacent zeolitic framework oxygen atoms (see local structure of [FeO]²⁺ in Figure 4.2). The saturated 6-fold coordination environment of Fe²⁺ weakens the Lewis acidity of the Fe center and hampers its further interaction with other reactants. The reaction is mainly driven by the formation of a O₂ peroxy/superoxy species ($r(\text{O–O}) = 1.345$ Å) bonded to Fe. After the removal of the weakly bound N₂, the catalytic cycle is closed by desorption of O₂ from the [FeO₂]²⁺ showing a reaction energy of 143 kJ/mol on the spin surface of $S = 4/2$. One should note that because the ground state of the initial isolated Fe²⁺ corresponds to $S = 4/2$, after triplet oxygen evolution, the spin state of the system changes to $S = 6/2$. As shown in Figure 4.1, the intermediates in the $S = 6/2$ electronic configuration are generally much less stable, compared to their $S = 4/2$ counterparts, until the generation of surface O₂ species. The O₂ desorption barrier is lowered to 89 kJ/mol when the spin state transition between the two electronic configurations is considered.

The reaction path for N₂O decomposition over isolated Fe²⁺ at the β -1 site is shown in Figure 4.3. The exothermic adsorption of N₂O ($\Delta E^{ads} = -39$ kJ/mol) is followed by a facile dissociation of N–O bond and removal of N₂ molecule resulting in the oxygenated [FeO]²⁺ species ($\Delta E^{\ddagger} = 80$ kJ/mol, $\Delta E = -46$ kJ/mol). The local structures and geometric parameters of each intermediate involved in the reaction are shown in Figure 4.4. The ability of [FeO]²⁺ to activate second N₂O molecule is only slightly higher than that of Fe²⁺/ α -1. The adsorption energy of N₂O to [FeO]²⁺ in this case is only -3 kJ/mol. The activation barrier of N–O bond dissociation is 176 kJ/mol and the reaction energy is -62 kJ/mol.

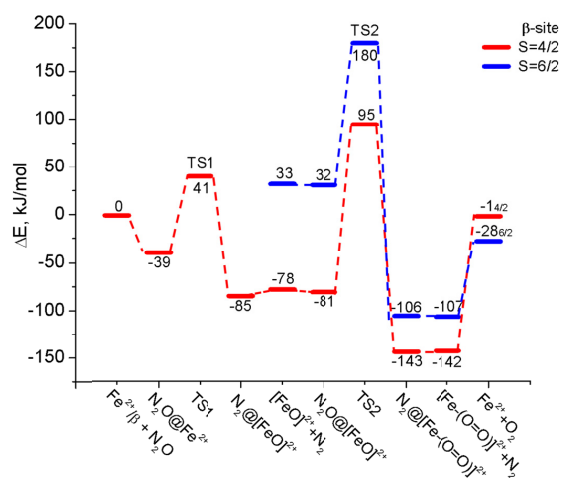


Figure 4.3. The reaction energy profile of N₂O decomposition over isolated Fe²⁺@β-1 site. Both low-spin state ($S = 4/2$) and high-spin state ($S = 6/2$) are indicated.

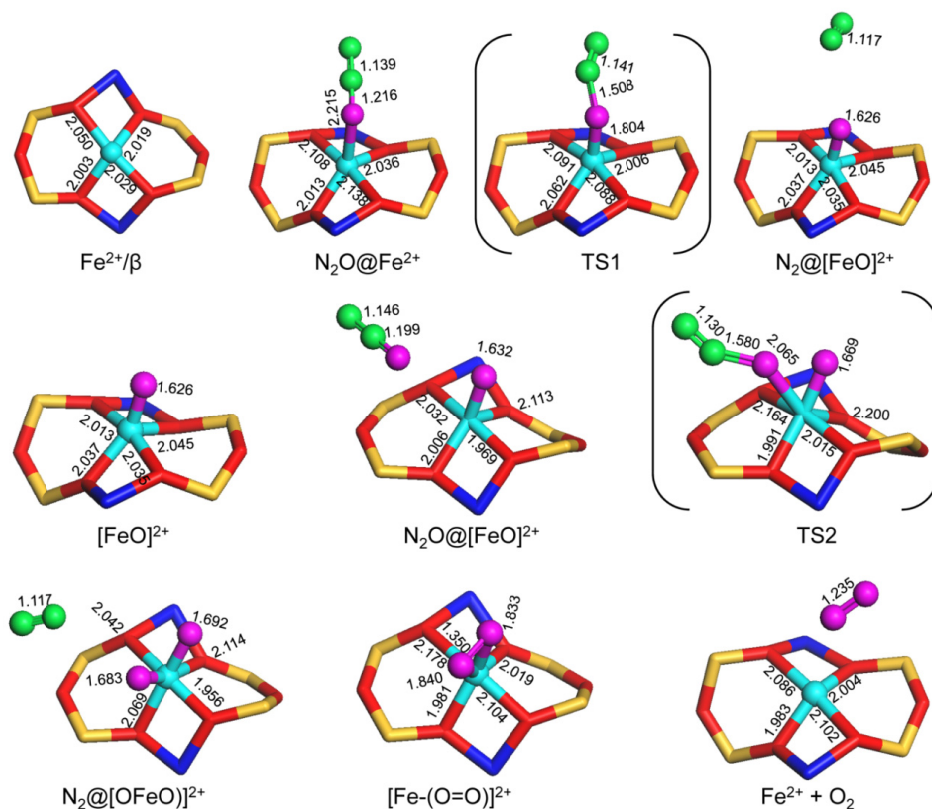


Figure 4.4. Selected interatomic distances of the intermediates and transition state structures involved in N₂O decomposition over Fe²⁺@β-1 site.

In contrast to the situation discussed above for Fe^{2+}/α -1, in the case of the β -1 site, the N–O bond in TS2 is activated directly by the Fe center with $r(\text{Fe}-\text{O}_{\text{EF}}) = 2.065 \text{ \AA}$. This is due to the deformed structure of the 6MR of β -1 site, which significantly reduces the repulsion between framework and extraframework oxygen atoms in the TS2. Another important factor is that, the isolated Fe^{2+} over β -1 site is 4-fold coordinated by O_{F} (O_{F} = framework oxygen atoms). After the first N_2O decomposition, Fe^{2+} has only 5 ligands allowing thus for the accommodation of one more oxygen atom after the N_2O dissociation (See the local structure of $\text{N}_2\text{O}@\text{[OFeO]}^{2+}$ in Figure 4.4). However, for the situation of α -1 site, the initial Fe^{2+} is bound to five O_{F} atoms (four of them in the 6MR, and one O_{F} at the bottom of the plane). After the formation of the Fe– O_{EF} bond (O_{EF} = extraframework oxygen atoms), a stable distorted octahedral configuration is formed and the catalytic activity of Fe center decreases dramatically. This explains the different mechanism, as well as the lower activation barrier and reaction energy computed for the activation of the second N_2O molecule over Fe^{2+}/β -1 site compared to those over α -1 site.

At the next step of the catalytic reaction, N_2 is desorbed and the formed $[\text{OFeO}]^{2+}$ species transforms into peroxy/superoxy $[\text{FeO}_2]^{2+}$ complex (Figure 4.4). The subsequent desorption of O_2 shows a barrier of 141 kJ/mol on the potential energy surface of $S = 4/2$. Similar to the situation in the case of the α -1 site, at this step the transition from the $S = 4/2$ to $S = 6/2$ spin state becomes favorable. When such a transition is taken into account the energy of O_2 desorption is lowered to 114 kJ/mol.

Fe^{2+} stabilized within the configuration of the most stable δ -1 sites shows a similar reactivity to that over Fe^{2+}/α -1 site (Figure 4.5). The adsorption of first N_2O is only slightly exothermic with $\Delta E^{\text{ads}} = -9 \text{ kJ/mol}$. The N–O bond cleavage over the Fe^{2+} is an exothermic process ($\Delta E = -57 \text{ kJ/mol}$) and shows the lowest activation energy among the Fe^{2+} complex considered (δ -1: $\Delta E^{\ddagger\text{TS1}} = 59 \text{ kJ/mol}$, α -1: $\Delta E^{\ddagger\text{TS1}} = 82 \text{ kJ/mol}$, β -1: $\Delta E^{\ddagger\text{TS1}} = 80 \text{ kJ/mol}$). The resulting $[\text{FeO}_{\text{EF}}]^{2+}$ forms an almost perfect square-pyramidal configuration of the Fe center with the zeolite framework leading to its low Lewis acidity similar to the α -1 case (see local structure of $[\text{FeO}]^{2+}$ in Figure 4.6). The second N_2O molecule interacts only weakly with the terminal oxygen of $[\text{FeO}]^{2+}$ ($\text{N}_2\text{O}@\text{[FeO]}^{2+}$ in Figure 4.6) and dissociates with a very high activation barrier ($\Delta E^{\ddagger\text{TS2}} = 222 \text{ kJ/mol}$) and a moderate reaction energy ($\Delta E = -49 \text{ kJ/mol}$). The catalytic cycle is closed by recombination of two terminal oxygen atoms form a surface O_2 species and release molecular O_2 into gas phase with a desorption barrier of 126 kJ/mol at the spin surface of $S = 4/2$, and of 89 kJ/mol by consideration of the transition to the $S = 6/2$ electronic state.

The result presented so far suggest that the isolated Fe^{2+} at the deformed β -1 6MR site is the most reactive towards the direct N_2O decomposition. It shows a somewhat lower activation barrier for dissociating second N_2O molecule compared to the situation when the reaction is carried out on Fe^{2+} located at α -1 and δ -1 positions. Fe^{2+} ions at all three locations are very reactive towards dissociation of the first N_2O and generation of the highly active surface oxygen species necessary for hydrocarbon oxidation [57]. However,

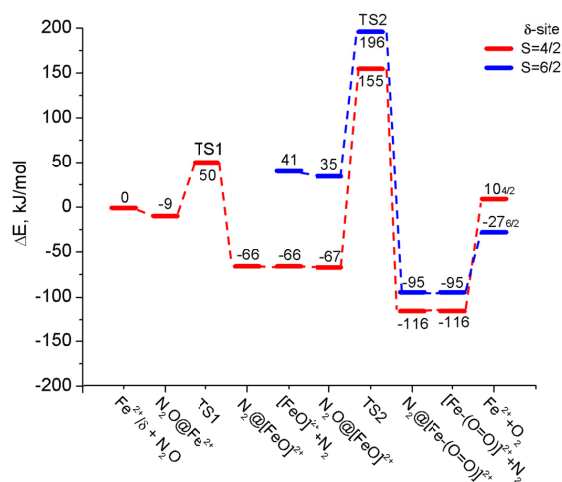


Figure 4.5. The reaction energy profile of N₂O decomposition over isolated Fe²⁺@δ-1 site. Both low-spin state ($S = 4/2$) and high-spin state ($S = 6/2$) are indicated.

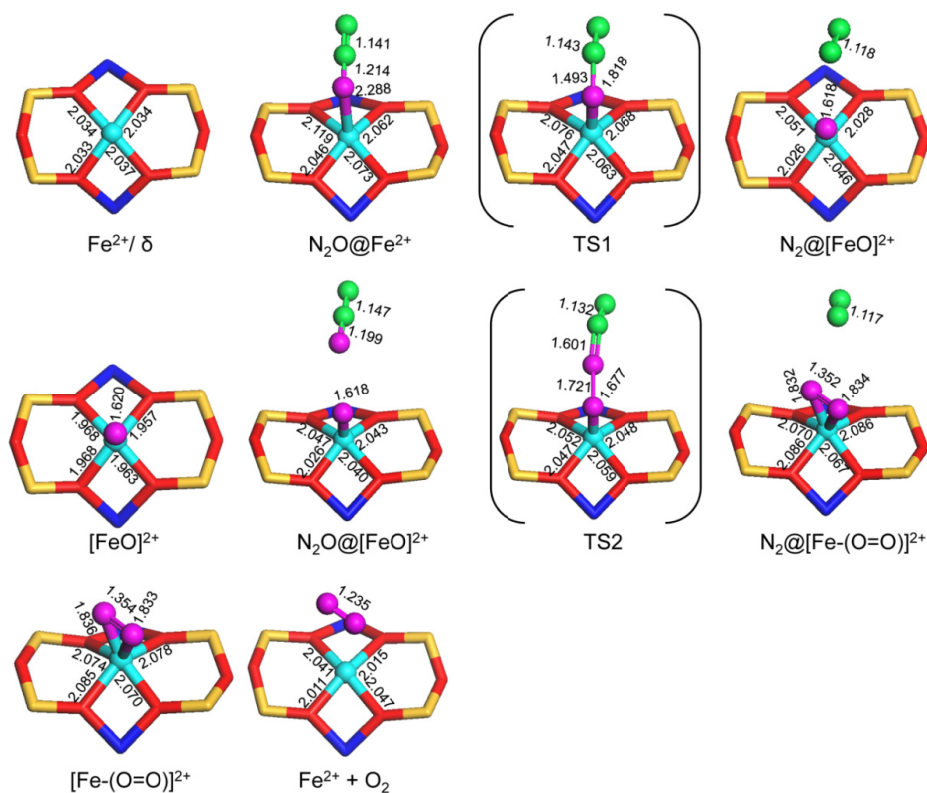


Figure 4.6. Selected interatomic distances of the intermediates and transition state structures involved in N₂O decomposition over Fe²⁺@δ-1 site.

depending on the local zeolite environment, only specific location of the $[\text{FeO}]^{2+}$ species exhibit sufficient Lewis acidity to activate N–O bond and form surface O_2 species as precursor towards molecular O_2 .

4.3.2. Reaction mechanism of N_2O decomposition over $[\text{FeO}]^+$

Beside isolated Fe^{2+} species, mononuclear $[\text{FeO}]^+$ complex containing formally Fe^{3+} ions has also been proposed as the active site for the direct N_2O decomposition. Therefore we also considered $[\text{FeO}]^+$ species as the potential active site. The most stable configuration, containing $[\text{FeO}]^+$ stabilized at δ - site 6MR with one charge compensating $[\text{AlO}_2]^-$ unit at the T11 lattice position [57], has been selected to investigate the mechanism of the catalytic reaction.

Figure 4.7 presents the calculated reaction energy profiles for N_2O decomposition and O_2 evolution by $[\text{FeO}]^+$ following the mechanism illustrated in Scheme 4.1. Because the energy difference between the high spin ($S = 5/2$) and the low spin states ($S = 3/2$) of $[\text{FeO}]^+$ species equals is only 21 kJ/mol, both states can potentially be involved in the catalytic reaction. The adsorption energy of the first N_2O molecule over $[\text{FeO}]^+$ at the high spin potential energy surface ($S = 5/2$) equals -4 kJ/mol. The reaction energy for N_2O decomposition is -51 kJ/mol. After N–O bond cleavage, the low spin state ($S = 3/2$) of $[\text{OFeO}]^+$ is 54 kJ/mol more stable than the $S = 5/2$, indicating a spin-transition upon the N_2O dissociation ($5/2 \rightarrow 3/2$). The computed barriers for this step are 9 ($S = 5/2$) and 73 ($S = 3/2$) kJ/mol, respectively. After N_2 desorption, $[\text{OFeO}]^+$ is a distorted square-planar complex with two O_F and two O_EF atoms acting as ligands (Figure 4.8). This structural property is only slightly dependent on the different electronic configurations involved. At this stage, there are one more electronic configuration ($S = 1/2$) becomes possible. The lowest-spin doublet $[\text{OFeO}]^+$ shows a comparable stability ($\Delta E^{3/2-1/2} = 4$ kJ/mol) to the quartet electronic configuration. The high-spin $S = 5/2$ state lies 50 kJ/mol above the quartet $S = 3/2$ configuration. The Fe center in the square-planar $[\text{OFeO}]^+$ can coordinate and activate the second N_2O molecule. The activation barrier in this case is 178 kJ/mol.

The reaction is accompanied by a change of the electronic ground state from $S = 3/2$ to $S = 1/2$. The most stable electronic configuration of $[\text{OFeOO}]^+$ after the second N_2O dissociation ($S = 1/2$) is 44 kJ/mol more stable than $S = 3/2$ and 103 kJ/mol more stable than $S = 5/2$. The reaction energy for spin-crossing is 27 kJ/mol. The lengths of three Fe– O_EF bonds in $[\text{OFeOO}]^+$ are ca. 1.70 Å (Figure 4.8). At the next stage, the $[\text{OFe(O=O)}]^+$ species is formed by recombination of two terminal oxygen atoms in $[\text{OFeOO}]^+$ species. This structural rearrangement is favorable and accompanied by the stabilization of the high spin $S = 5/2$ state. The active center is regenerated via O_2 desorption ($\Delta E = 94$ kJ/mol and 72 kJ/mol for the paths without ($S = 5/2$) and with spin transition ($S = 5/2 \rightarrow S = 7/2$), respectively).

Thus, both isolated Fe^{2+} and $[\text{FeO}]^+$ active sites are very reactive towards dissociating a single N_2O molecule. However, for further catalytic reaction to proceed, a very

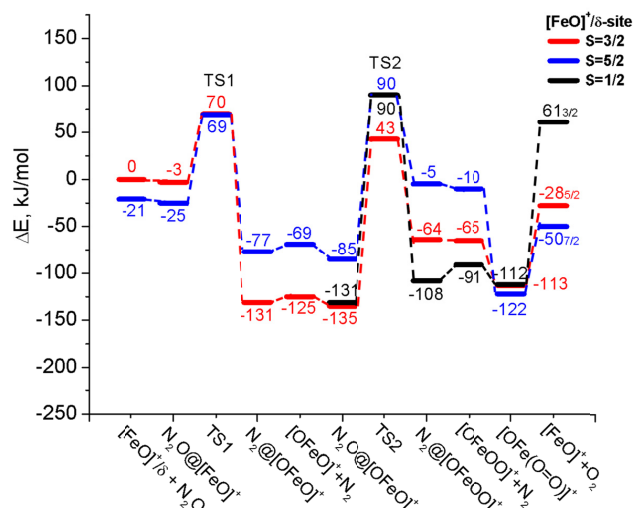


Figure 4.7. The reaction energy profile of N₂O decomposition over [FeO]⁺/δ-1 site.

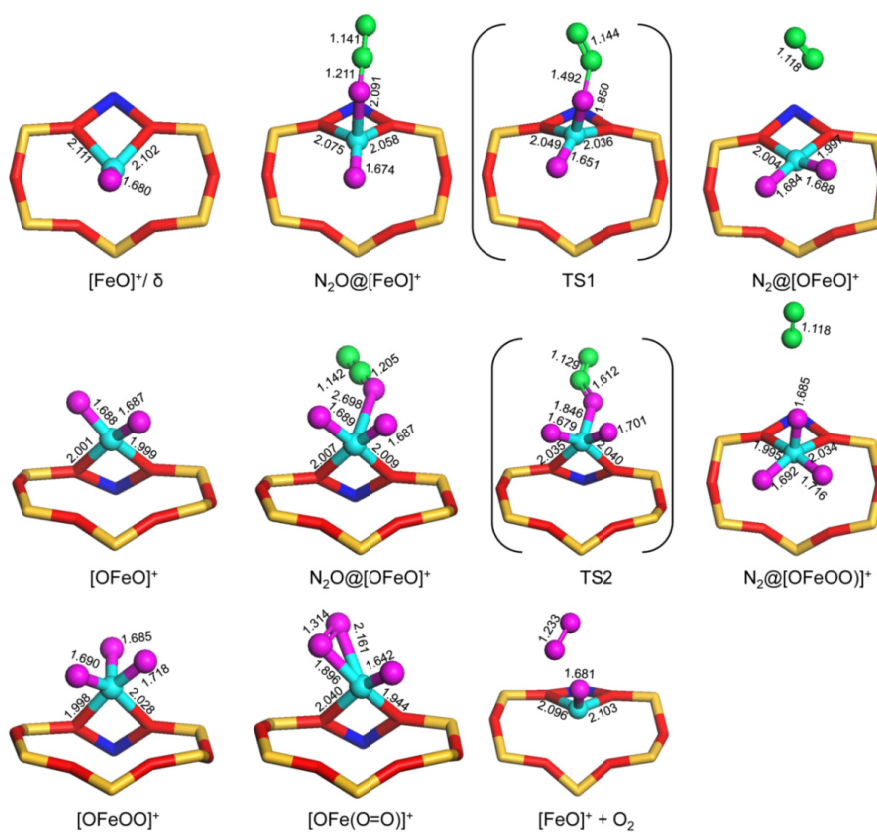
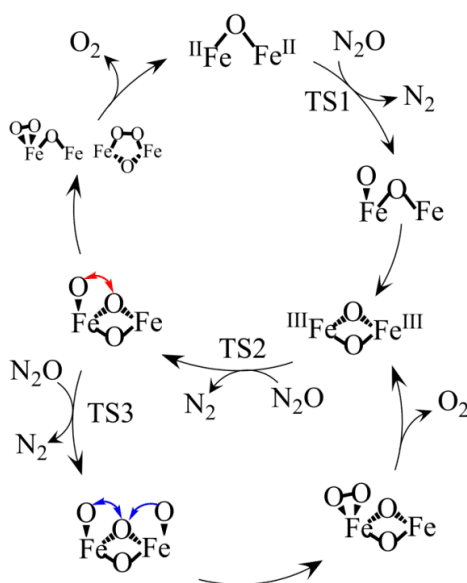


Figure 4.8. Selected interatomic distances of the intermediates and transition state structures involved in N₂O decomposition over [FeO]⁺/δ-1 site on spin state of S = 5/2.

unfavorable activation of the second N_2O molecule has to take place. In the case of the $[\text{FeO}]^{2+}$ intermediates at α - and δ - sites, the reaction involves the interaction with the terminal oxygen atoms of the extraframework species and show barriers above 200 kJ/mol. Somewhat lower barriers are computed in the case of the reaction over $[\text{FeO}]^{2+}$ at β -1 site and $[\text{OFeO}]^+$ at δ - site, which still reach values of around 180 kJ/mol. These results suggest that, the mononuclear Fe^{2+} and $[\text{FeO}]^+$ cannot be considered as the dominate active sites for the catalytic N_2O decomposition reaction.

4.3.3. Reaction mechanism of N_2O decomposition over $[\text{Fe}(\mu\text{-O})\text{Fe}]^{2+}$

We further investigated the catalytic reactivity of binuclear Fe sites in ZSM-5. In Chapter 2, we demonstrated that depending on the catalyst activation conditions, the binuclear $[\text{Fe}(\mu\text{-O})\text{Fe}]^{2+}$ or $[\text{Fe}(\mu\text{-O})_2\text{Fe}]^{2+}$ complexes are the predominant iron-containing sites in Fe/ZSM-5. The oxygen bridged cations were accommodated in the 8MR of the sinusoidal channel with two charge compensating Al atoms at T7 and T12 sites. This location is preferred site for stabilizing $[\text{Fe}(\mu\text{-O})\text{Fe}]^{2+}$ and $[\text{Fe}(\mu\text{-O})_2\text{Fe}]^{2+}$ binuclear complexes (Chapter 2). The high spin ferromagnetic state ($S = 8/2$) is the ground state electronic configuration for both complexes.



Scheme 4.2. Possible reaction paths for direct N_2O decomposition over binuclear $[\text{Fe}(\mu\text{-O})\text{Fe}]^{2+}$ site.

The proposed reaction mechanism is depicted schematically in Scheme 4.2. As can be seen from Figure 4.9, physical adsorption of N_2O on the $[\text{Fe}(\mu\text{-O})\text{Fe}]^{2+}$ species is slightly exothermic ($\Delta E^{ads} = -15$ kJ/mol). By overcoming an activation barrier of 85 kJ/mol, the N–O bond is dissociated and $[\text{OFe}(\mu\text{-O})\text{Fe}]^{2+}$ species is formed with weakly bonded N_2 molecule. The reaction energy (-77 kJ/mol) for this step is close to that computed for the

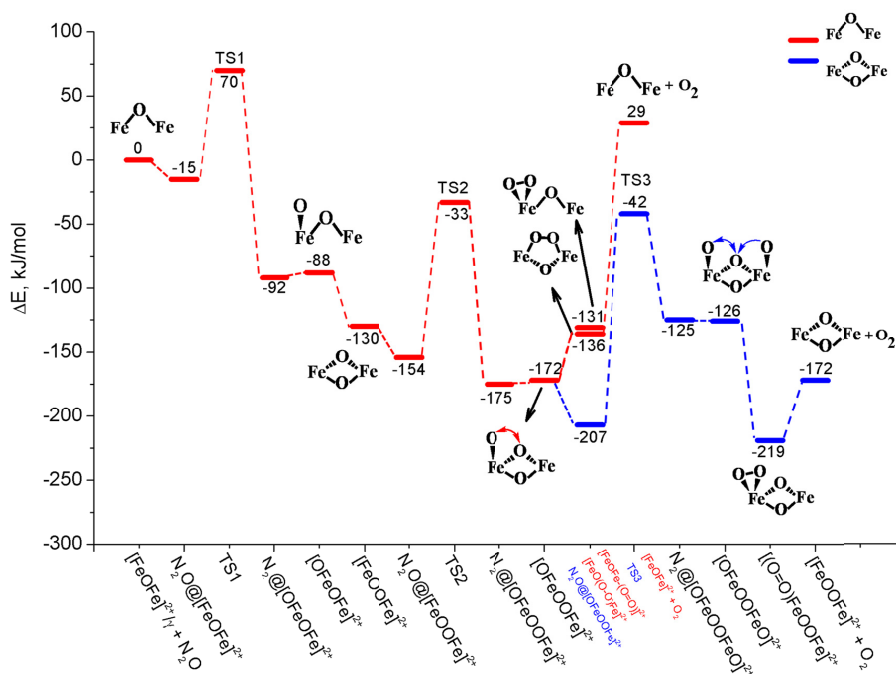


Figure 4.9. The reaction energy profile of N₂O decomposition over $[\text{FeOFe}]^{2+}/\gamma$ - site ($S = 8/2$). Schematic representations of concerned key intermediates are inserted.

mononuclear sites discussed above. The optimized local geometrical parameters for all reaction intermediates are summarized in Figure 4.10. At the next step, prior to reacting with the second N₂O molecule, $[\text{OFe}(\mu\text{-O})\text{Fe}]^{2+}$ undergoes a structural rearrangement to form a cyclic $[\text{Fe}(\mu\text{-O})_2\text{Fe}]^{2+}$ driven by the excessive basicity of the terminal oxygen in $[\text{OFe}(\mu\text{-O})\text{Fe}]^{2+}$. As shown in Figure 4.10a ($[\text{FeOOFe}]^{2+}$), the cyclic $[\text{Fe}(\mu\text{-O})_2\text{Fe}]^{2+}$ complex is a quasi-planar structure lying above the 8MR, which is about 40 kJ/mol more stable than the $[\text{OFe}(\mu\text{-O})\text{Fe}]^{2+}$ isomer. Such a structural rearrangement has been observed before and can be considered as a general phenomenon [58]. After this rearrangement, both iron centers become available for the coordination of a next reactant molecule. The intrinsic activation barrier for the dissociation of second N–O bond is 121 kJ/mol, which is about 60 kJ/mol lower than the values computed for the mononuclear sites. The reaction yields a $[\text{OFe}(\mu\text{-O})_2\text{Fe}]^{2+}$ complex.

The reaction can then proceed via two alternative mechanisms (Scheme 4.2). Two of three extraframework oxygens of $[\text{OFe}(\mu\text{-O})_2\text{Fe}]^{2+}$ could recombine resulting in a $[(\text{O}=\text{O})\text{Fe}(\mu\text{-O})\text{Fe}]^{2+}$ complex with an O₂ precursor bound to one of the iron centers. Alternatively, it can transform to a $[\text{Fe}(\mu\text{-O})(\mu\text{-OO})\text{Fe}]^{2+}$ peroxo-diiron intermediate (see the local structure in Figure 4.10b). These two intermediates have comparable stability, and the rearrangement shows a barrier of ca. 40 kJ/mol. At the next step, the $[\text{Fe}(\mu\text{-O})\text{Fe}]^{2+}$

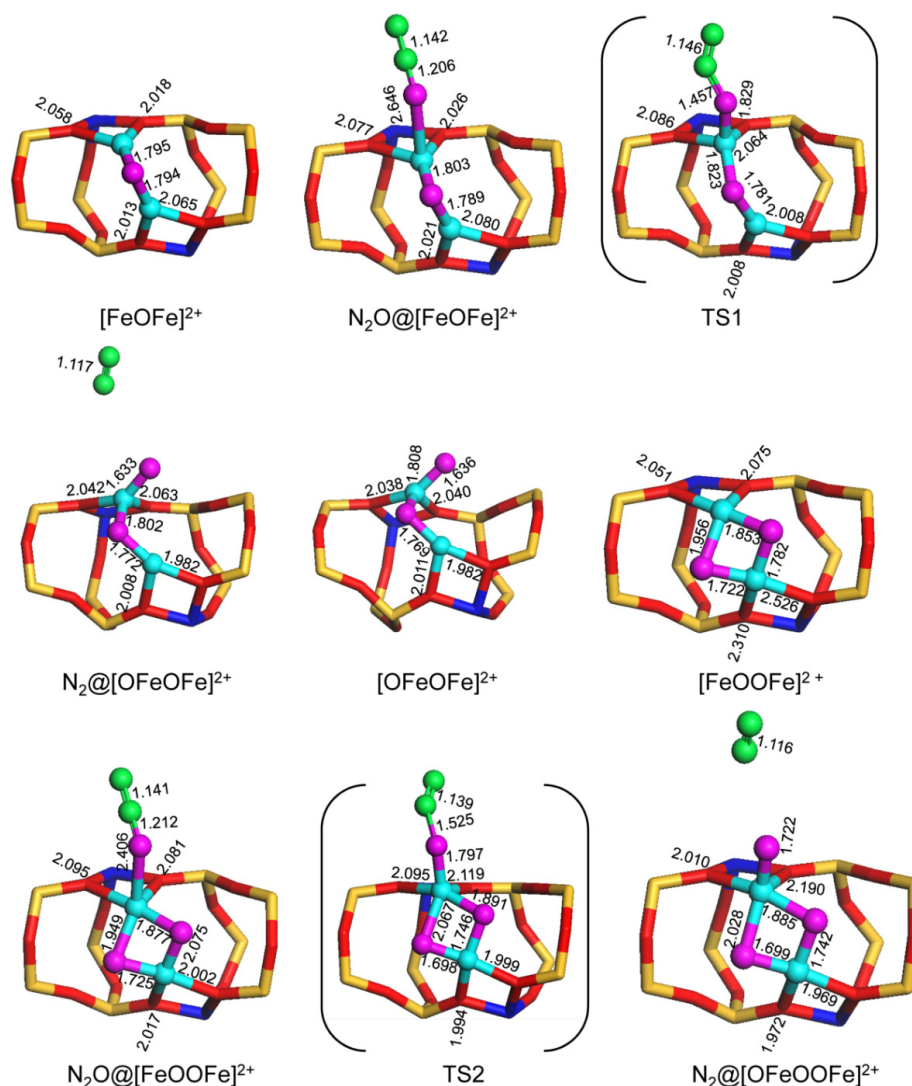


Figure 4.10a. Selected interatomic distances of the intermediates and transition state structures involved in N_2O decomposition over $[\text{FeOFe}]^{2+}@ \gamma$ -site ($S = 8/2$).

active site is regenerated and the catalytic cycle is closed by O_2 desorption which is the rate-limited step with a barrier of 160 and 165 kJ/mol from $[(\text{O}=\text{O})\text{Fe}(\mu\text{-O})\text{Fe}]^{2+}$ and $[\text{Fe}(\mu\text{-O})(\mu\text{-OO})\text{Fe}]^{2+}$ complex, respectively.

One should note that, besides the 5-coordinated iron center in $[\text{OFe}(\mu\text{-O})_2\text{Fe}]^{2+}$ (see the local structure of $[\text{OFeOOFe}]^{2+}$ in Figure 4.10b), the other 4-coordinated iron center can also play a role of an active center and activate further one more N_2O molecule. Figure 4.9 shows that, adsorption of the third N_2O on the coordinatively unsaturated Fe site in

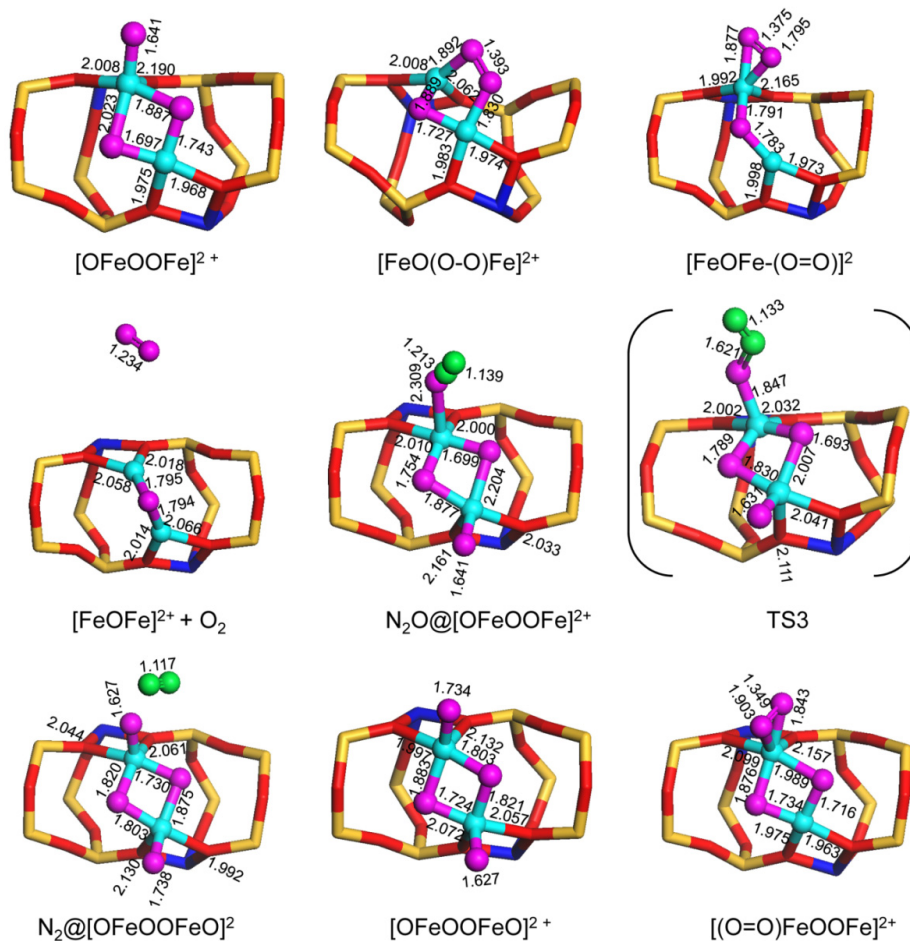


Figure 4.10b. (Continued).

$[OFe(\mu-O)_2Fe]^{2+}$ is exothermic ($\Delta E^{ads} = -35$ kJ/mol) indicating its considerable Lewis acidity. The subsequent dissociation of the N–O bond proceeds with a barrier of 165 kJ/mol. The reaction is endothermic and the produced intermediate $[OFe(\mu-O)_2FeO]^{2+}$ is 82 kJ/mol less stable than the initial state. Recombination of the terminal extraframework oxygens leads to a superoxo-like species coordinated to one of the iron ions (see local structure of $[(O=O)FeOOFe]^{2+}$ in Figure 4.10b). This process leads to an energy gain of 93 kJ/mol. Finally, desorption of O₂ with a barrier of 61 kJ/mol leaves behind $[Fe(\mu-O)_2Fe]^{2+}$ complex with both Fe ions in the formal trivalent state.

Summarizing, both the activation barrier and reaction energy for the first N₂O dissociation over $[Fe(\mu-O)Fe]^{2+}$ site are comparable to that over mononuclear Fe²⁺ and $[FeO]^+$ sites. This indicates that all three sites are able to dissociate N₂O molecule and generate a reactive extraframework oxygen center. However, the mononuclear sites cannot

carry out the reaction in a catalytic manner. The activation barrier for the dissociation of the second N_2O molecule over $[\text{FeO}]^{2+}$ and $[\text{FeO}_2]^+$ is prohibitively high. During the catalytic N_2O decomposition, binuclear $[\text{Fe}(\mu\text{-O})\text{Fe}]^{2+}$ site converts to $[\text{OFe}(\mu\text{-O})\text{Fe}]^{2+}$ that rearranges into a more stable $[\text{Fe}(\mu\text{-O})_2\text{Fe}]^{2+}$ cyclic complex. This leads to two iron centers exposed to further coordination and activation of the second N_2O molecule. The activation barrier for the second N_2O dissociation over $[\text{Fe}(\mu\text{-O})_2\text{Fe}]^{2+}$ site is 121 kJ/mol, which is much lower than the values computed for the mononuclear sites. The recombination of extraframework oxygen atoms in $[(\text{O}=\text{O})\text{Fe}(\mu\text{-O})\text{Fe}]^{2+}$ or $[\text{Fe}(\mu\text{-O})(\mu\text{-OO})\text{Fe}]^{2+}$ intermediates leads to desorption of molecular O_2 and closes the catalytic cycle. An alternative path involves the activation of the third N_2O reactant over $[\text{OFe}(\mu\text{-O})_2\text{Fe}]^{2+}$. This step shows an activation barrier of 165 kJ/mol. Nevertheless, it is still lower than the barriers computed for the mononuclear sites. This transformation is thermodynamically less favorable on the high spin potential energy surface ($\Delta E = 82$ kJ/mol) because of the coexistence of two unstable terminal oxygen ligands of $[\text{OFeOOFeO}]^{2+}$ complex. Finally, O_2 recombination takes place and the initial $[\text{Fe}(\mu\text{-O})\text{Fe}]^{2+}$ becomes oxidized into Fe^{III} -containing $[\text{Fe}(\mu\text{-O})_2\text{Fe}]^{2+}$ cationic complex.

4.3.4. Spin state transition

With regard to the spin state of Fe, usually the high spin state is favorable [21, 25, 55, 59]. Previous theoretical investigations on antiferromagnetic nature of binuclear iron complexes in Fe/ZSM-5 have stated that it has only a minor effect on the reaction mechanism of the N_2O decomposition such as the nature of the rate-limited step and the height of the reaction barriers [21, 25, 56]. However, one expects that the change of the coordination of iron centers and structural rearrangement of the intermediates in the course of the reaction influence significantly the electronic configurations of the intrazeolite complex. With this consideration, the stabilities of reaction intermediates with respect to different electronic configurations were investigated. The results are summarized in Figure 4.11. One can see that, the high spin state ($S = 8/2$) is preferred for the initial $[\text{Fe}(\mu\text{-O})\text{Fe}]^{2+}$ complex. However, after the first N_2O dissociation, the stability of the resulting $[\text{FeOFeO}]^{2+}$ in $S = 6/2$ state becomes comparable to the $S = 8/2$ configuration. After the structural rearrangement, $[\text{Fe}(\mu\text{-O})_2\text{Fe}]^{2+}$ is slightly more stable on the $S = 6/2$ PES (potential energy surface) than on the high spin PES. This electronic configuration is the ground state during the subsequent dissociation of the second N_2O molecule. Upon recombination of the extraframework oxygen atoms, different spin state stabilities for $[\text{FeOFe}(\text{O}=\text{O})]^{2+}$ ($S = 8/2$) and $[\text{FeO}(\text{O}=\text{O})\text{Fe}]^{2+}$ ($S = 6/2$) are observed. Because of the triplet configuration of molecular oxygen, for O_2 desorption and $[\text{FeOFe}]^{2+}$ regeneration step at the end of the cycle, $S = 10/2$ is the preferred state compared to the other spin multiplicities. For the alternative reaction path, after the third N_2O decomposition over $[\text{OFeOOFe}]^{2+}$, antiferromagnetic $[\text{OFeOOFeO}]^{2+}$ complex with $S = 0$ corresponds to the ground state. However, after oxygen migration and recombination, the spin state with $S = 6/2$ becomes stable again. These results imply that the catalytic N_2O decomposition over binuclear Fe

Catalytic properties of extraframework iron-containing species in ZSM-5 for N₂O decomposition

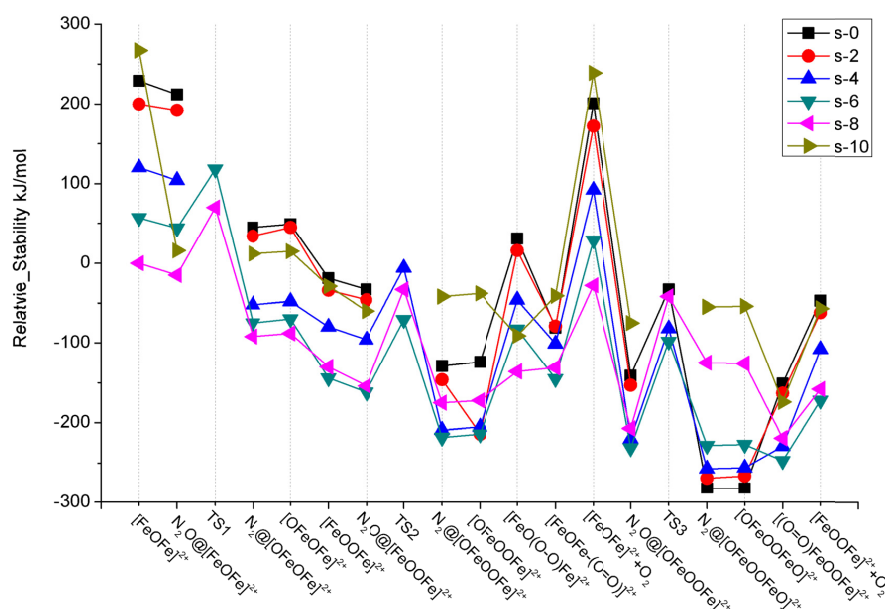


Figure 4.11. Spin states dependent stabilities of reaction intermediates involved in N₂O decomposition over binuclear [Fe(μ -O)Fe]²⁺ active site.

sites in ZSM-5 is associated with multiple changes in the spin state along the reaction coordinate.

After taking the spin state crossing into account, Figure 4.12 presents the minimum energy path for N₂O decomposition over binuclear [FeOFe]²⁺ active center. It can be seen that there are totally 6 spin states crossing involved in the overall reaction path. They are observed during structural rearrangement, O₂ desorption, and [OFeOOFe]²⁺ formation steps. Accompanying structural rearrangement of [OFeOFe]²⁺ into [FeOOFe]²⁺ closed ring, the spin state transfer takes place from the highest $S = 8/2$ state to the intermediate $S = 6/2$ one. The activation barrier of the second N₂O decomposition on the PES of $S = 6/2$ is 30 kJ/mol lower than that on the high spin PES (Figure 4.9). The energy of the resulting [FeOOFe]²⁺ is lowered on the low spin PES by 43 kJ/mol. This results in the reaction energy benefited by -35 kJ/mol. The reverse spin transition from the lower state back to the highest state occurs during the migration and recombination of extraframework oxygen atoms into adsorbed O₂. This process faces a barrier of 70-80 kJ/mol depending on the type of adsorbed O₂ species. The overall barrier for O₂ generation and desorption from the active center is 186 kJ/mol on the minimum energy reaction coordinate. The activation of the third N₂O shows a barrier of 133 kJ/mol. The resulting intermediate with two terminal oxygen ligands is much more stable on the singlet antiferromagnetic PES. The spin state crossing at this step dramatically changes the reaction process from endothermic on PES $S = 8/2$ to thermodynamically very favorable. As a result, the O₂ desorption proceeds with an energy of 110 kJ/mol. Thus, when changes in spin multiplicities are allowed during the

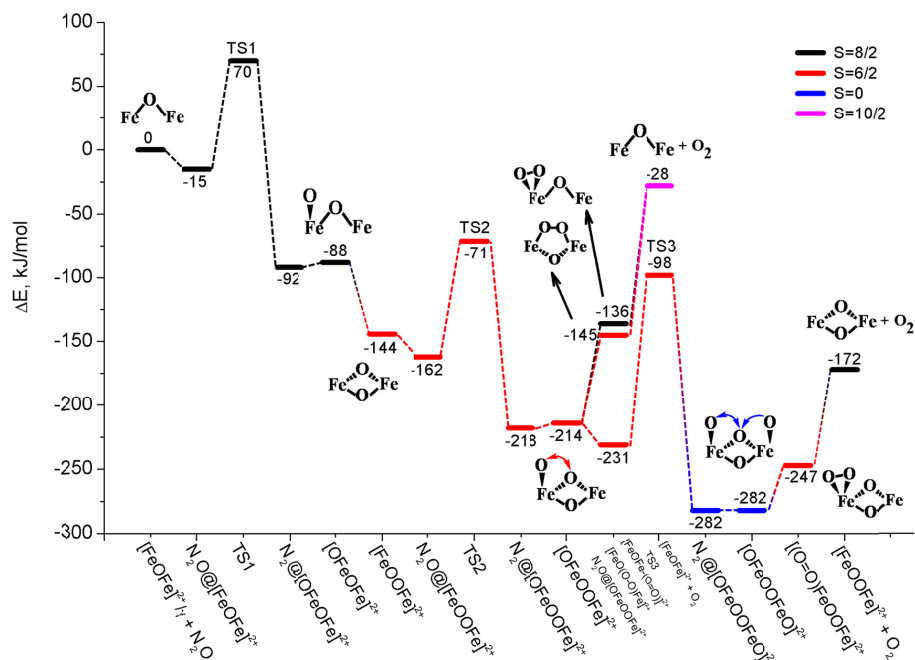


Figure 4.12. Minimum energy path of N_2O decomposition over binuclear $[\text{FeOFe}]^{2+}$ active site after spin state optimization.

catalytic cycle, the Fe^{II} to Fe^{III} reaction path becomes more favorable than that over the highest-spin PES $S = 8/2$. These results are in contrast to the previous statements on the low impact of spin crossings on the reactivity of binuclear Fe sites [21, 25].

Summarizing the above results, it can be concluded that binuclear $[\text{Fe}(\mu\text{-O})\text{Fe}]^{2+}$ species is much more active for the catalytic N_2O decomposition than the mononuclear Fe^{2+} and $[\text{FeO}]^+$ species. It is in agreement with the spectroscopic data of Sun et al. which suggested that binuclear iron sites are responsible for the catalytic activity of Fe/ZSM-5 in N_2O decomposition, whereas the mononuclear iron sites are active for benzene hydroxylation to phenol [60]. The distinct catalytic reactivity for N_2O decomposition over mononuclear and binuclear sites implies that there are two types of extraframework oxygen species. They could be distinguished by their different catalytic performances with respect to specific reactions. The mononuclear Fe^{2+} and $[\text{FeO}]^+$ sites are capable of generating one type of reactive extraframework oxygen by activating a single N_2O molecule. This kind of “isolated” extraframework oxygen is potentially active for benzene oxidation as has been proved by the realistic activation energies discussed in Chapter 3 [57]. In principle, they could also contribute to catalytic oxygen evolution reactions. However, since the activation barrier for direct activation of the second N_2O molecule over mononuclear site is prohibitively high, we speculate that the O_2 evolution in this case takes place mainly

through the long range surface migration and recombination of extraframework oxygens from different mononuclear active sites. Such a long-range migration can potentially be achieved at high temperature. For binuclear iron-containing species, each iron center can act as catalytic site for N₂O activation. Therefore, the surface O₂ species can be formed through short range migration and recombination of terminal oxygen atoms between two iron centers within a single binuclear complex. We propose that this type of extraframework oxygen species contributes to the generation of O₂ at moderate temperatures. This is in line with the available experimental data suggesting the presence of different surface oxygen species with different thermal stability [61]. Ates et al. found that the amount of surface oxygen evolved upon a temperature-programmed desorption (TPD) experiment strongly depends on the temperature, because the formation of O₂ precursors at different sites needs to overcome different activation barriers. For materials with a higher iron content, the desorption of surface oxygen species is facilitated [14, 15, 61]. Kiwi-Minsker et al. also reported that only a part of surface oxygen deposited by decomposing N₂O was active in CO oxidation at 523 K. Such O species are characterized by a sharp O₂ peak at 666 K during the TPD measurements [32]. The broad peak with a maximum at 940 K in the TPD-O₂ profile was assigned to a diffusion-controlled recombination mechanism. Similar TPD results reported by Xia et al. also indicate that the low temperature O₂ desorption peak at 640 K after N₂O decomposition was formed on the binuclear sites [51]. By taking these experimental results into account, we propose that the low-temperature TPD-O₂ peak is due to the direct O₂ recombination from binuclear [Fe(μ -O)Fe]²⁺ and [Fe(μ -O)₂Fe]²⁺ sites, whereas the high-temperature signal is contributed by the extraframework oxygen migration and recombination between mononuclear Fe²⁺ and [FeO]⁺ sites. The binuclear sites are responsible for the catalytically direct N₂O decomposition reaction. The extraframework oxygen atoms on both mononuclear and binuclear sites have high activity for benzene oxidation. However, the extraframework oxygen ligands of binuclear sites favor the dissociative adsorption of the phenol product resulting in the deactivation of oxygenated iron complexes by stable grafted phenolate species.

4.3.5. Microkinetic analysis

Microkinetic analysis was performed on the basis of minimum reaction energy paths provided by the DFT calculations to get a further insight into the microscopic behavior of the systems upon the catalytic reaction. Figure 4.13a shows the concentration of intrazeolite complexes as a function of temperature in the range of 373 – 973 K. One can see that below 523 K the composition of extraframework cationic species is completely dominated by [Fe(μ -O)₂FeO]²⁺ complex. This is due to the relatively high stability of this complex that hinders the subsequent O₂ evolution or N₂O activation step showing rather high barriers. With increasing temperature the concentration of [Fe(μ -O)₂FeO]²⁺ gradually decreases and the [Fe(μ -O)Fe]²⁺ and [Fe(μ -O)₂Fe]²⁺ complexes dominate the Fe/ZSM-5 catalyst. Above 800 K, when the reaction rate increases strongly (Figure 4.13b), the

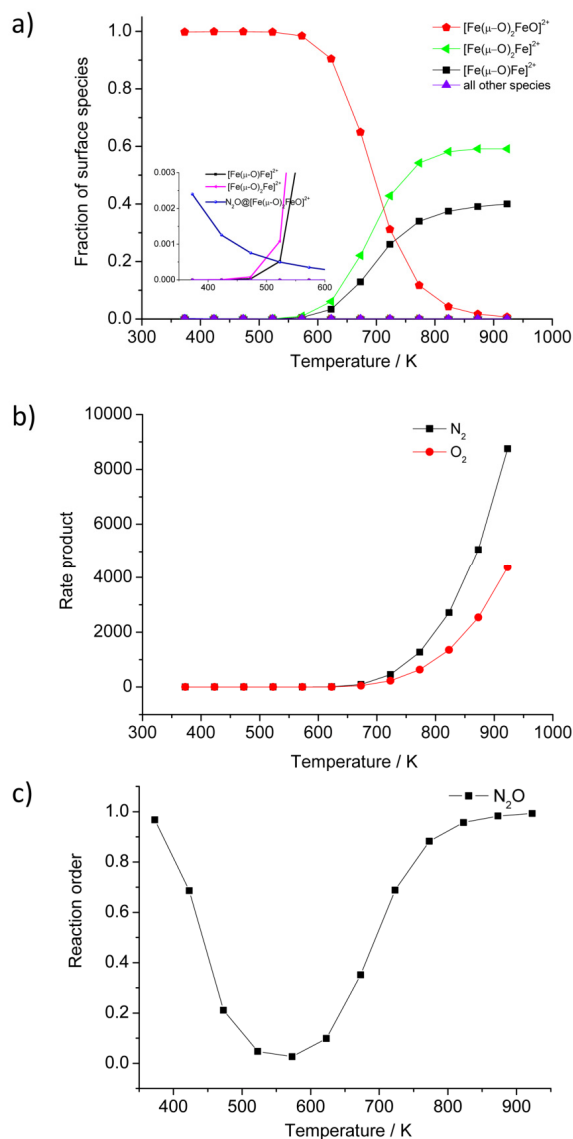


Figure 4.13. Micro-kinetic analysis based on minimum reaction energy path of DFT results. a): the steady-state surface species, b): the rate of producing N_2 and O_2 , c): the reaction order of N_2O , depends on the temperature.

$[\text{Fe}(\mu\text{-O})_2\text{FeO}]^{2+}$ concentration decreases to zero, and the intrazeolite iron complexes are present as $[\text{Fe}(\mu\text{-O})\text{Fe}]^{2+}$ and $[\text{Fe}(\mu\text{-O})_2\text{Fe}]^{2+}$ in a 60:40 ratio. This implies that both reaction paths depicted in Scheme 4.2 take place under the actual catalytic conditions and compete with each other. The slightly higher concentration of $[\text{Fe}(\mu\text{-O})_2\text{Fe}]^{2+}$ complex suggests that the reaction path of Fe^{II} to Fe^{III} is slightly more favorable. It is due to the

relatively lower barriers of N₂O dissociation over [Fe(μ -O)₂FeO]²⁺ complex and of O₂ desorption from [Fe(μ -O)₂Fe(OO)]²⁺ intermediate compared to the barrier of O₂ desorption from [Fe(μ -O)FeO]²⁺ species. The concentrations of all the other intermediates are very low at all temperatures.

Figure 4.13b shows the rate of production of N₂ and O₂ as a function of temperature. The simultaneous desorption of N₂ and O₂ from catalytic site is triggered at 673 K. The apparent activation energy (E_{app}) of the reaction at 723 K is 106 kJ/mol. The experimentally determined E_{app} values at the temperatures between 673 to 773 K lie between 120 to 190 kJ/mol depending on the catalyst synthesis and pre-activation conditions [4, 51, 62]. It is usually observed steam-calcined catalysts show higher E_{app} than the materials prepared using alternative methods. This can be attributed to the high activation barrier of N₂O decomposition over hydroxylated iron-containing species formed upon the high-temperature reaction of extraframework iron sites with water vapor [51]. An alternative explanation is the reaction inhibition by trace amount of water present in the feed under experimental conditions [51, 56]. Another source of error in the computed results can be also associated with the inaccuracies of DFT methodologies for the description of spin-transition and different electronic configurations of Fe complexes.

The reaction order with respect to N₂O is one at 373 K but decreases to zero with the temperature increase to 573 K (Figure 4.13c). Above 773 K the reaction order in N₂O becomes equal to one again. The change of the reaction order in the reactant from 0 \rightarrow 1 in the temperature range of 573 K to 773 K is in line with the experimental observations reported by Guesmi et al [13]. This result demonstrates that at 573 K, the reaction rate is independent of the partial pressure of N₂O. The migration and recombination of extraframework oxygen ligands on the active site is the rate-limited step which is not influenced by the N₂O concentration. Above 773 K, the reaction rate is first order with respect to N₂O because adsorption and dissociation of N₂O becomes the rate-limiting step. To explain the reaction order decrease from one to zero below 573 K, we analyzed the concentrations of less populated states (inset in Figure 13a). One can see that at the low temperatures, in addition to the predominant [Fe(μ -O)₂FeO]²⁺ complex, the adsorbed N₂O@[Fe(μ -O)₂FeO]²⁺ complex is much more abundant compared to all other reaction intermediates. This reflects that the first order of reaction rate with respect to N₂O observed at this stage is caused by the high barrier of N₂O dissociation over [Fe(μ -O)₂FeO]²⁺ complex.

4.4. Conclusion

The activities of stable mononuclear Fe²⁺ and [FeO]⁺ as well as binuclear [Fe(μ -O)Fe]²⁺ and [Fe(μ -O)₂Fe]²⁺ species in ZSM-5 zeolite for N₂O decomposition have been studied by periodic DFT calculation. Different reaction paths have been compared. The quantum-chemical results have been evaluated with a microkinetic analysis. Both mononuclear and binuclear iron-containing sites exhibit high activity for the activation of

the N–O bond and the generation of highly reactive extraframework oxygen species. However, the ability to form adsorbed O₂ species which is the precursor for O₂ evolution is structurally sensitive. In the case of mononuclear Fe²⁺, the activity and reaction mechanism depend on the local zeolite environment in the vicinity of the active site. The activation of a second N₂O over α - and δ - sites can only be promoted by the reaction with the terminal oxygen ligand showing prohibitively high activation barriers over 200 kJ/mol. A higher reactivity of the isolated Fe²⁺ in the catalytic N₂O decomposition can be achieved when the Fe²⁺ cation is stabilized at the deformed β - site at the intersection of straight and sinusoidal channels. The distorted local zeolite structure facilitates the coordination and activation of a second N₂O molecule at such site. For mononuclear [FeO]⁺ site, the reactivity for O₂ evolution is comparable to that over Fe²⁺/ β - site. The spin transitions between different spin potential energy surfaces are essential for stabilizing oxygenated intermediates. Nevertheless, both Fe²⁺ and [FeO]⁺ display limited reactivity for the catalytic N₂O decomposition and O₂ recombination due to the high activation barriers for the activation of the second N₂O molecule. They can generate one type of extraframework oxygens by dissociation of a single N₂O molecule. The resulting structures show a rather high stability and play an important role in benzene oxidation reaction. However, the O₂ evolution probably can only be realized by diffusion and recombination of this kind of extraframework oxygens formed at distant mononuclear sites.

The activation barrier for the direct N₂O decomposition and O₂ recombination over binuclear Fe sites is much lower than those computed in the cases of the mononuclear sites. In agreement with the experimental observations, the computational results obtained suggest the presence of two distinct types of extraframework oxygen species showing different thermal stability and corresponding to mono- and binuclear intrazeolite Fe complexes. The reaction energy for the first N₂O decomposition over binuclear site is lowered by the structural rearrangement of [OFeOFe]²⁺ intermediate into [FeOOFe]²⁺ complex. This makes both iron centers in the extraframework cation available for further activation of N₂O. The final state of iron can be either Fe^{II} or Fe^{III} depending on the reaction path followed. The catalytic decomposition of N₂O over the binuclear Fe sites in Fe/ZSM-5 involves multiple transitions among different spin multiplicities. Dependent on the specific chemical and coordination environment realized in a particular reaction intermediate ferromagnetic or antiferromagnetic electronic configuration can be preferred resulting in a high complexity of the overall mechanism of the catalytic reaction.

Microkinetic modeling provides further insights into the macroscopic parameters of the reaction such as the reaction rate, apparent activation barriers, and reaction order as a function of temperature that can be directly compared with reported experimental data. The computed apparent activation energy was found to be in a very good agreement with the available experimental result. The reaction order in the reactant was found to strongly depend on the reaction temperature, which is also in line with the experimental observation. The results obtained further support our proposal on the essential role of binuclear [Fe(μ -O)Fe]²⁺ and [Fe(μ -O)₂Fe]²⁺ species for the direct N₂O decomposition and O₂

evolution reactions.

References

- [1] V.I. Sobolev, G.I. Panov, A.S. Kharitonov, V.N. Romannikov, A.M. Volodin, K.G. Ione. *J. Catal.* 139 (1993) 435-443.
- [2] G.I. Panov, V.I. Sobolev, A.S. Kharitonov. *J. Mol. Catal.* 61 (1990) 85-97.
- [3] B.R. Wood, J.A. Reimer, A.G. Bell. *J. Catal.* 209 (2002) 151-158.
- [4] Q. Zhu, B.L. Mojet, R.A.J. Janssen, E.J.M. Hensen, J. van Grondelle, P. Magusin, R.A. van Santen. *Catal. Lett.* 81 (2002) 205-212.
- [5] G.I. Panov, A.K. Uriarte, M.A. Rodkin, V.I. Sobolev. *Catal. Today* 41 (1998) 365-385.
- [6] K.A. Dubkov, N.S. Ovanesyan, A.A. Shteinman, E.V. Starokon, G.I. Panov. *J. Catal.* 207 (2002) 341-352.
- [7] L.J. Lobree, I.-C. Hwang, J.A. Reimer, A.T. Bell. *J. Catal.* 186 (1999) 242-253.
- [8] Z. Sobalík, E. Tabor, J. Nováková, N.K. Sathu, K. Závěta. *J. Catal.* 289 (2012) 164-170.
- [9] E.V. Kondratenko, V.A. Kondratenko, M. Santiago, J. Pérez-Ramírez. *J. Catal.* 256 (2008) 248-258.
- [10] E.V. Kondratenko, J. Pérez-Ramírez. *J. Phys. Chem. B* 110 (2006) 22586-22595.
- [11] G.I. Panov, K.A. Dubkov, E.V. Starokon. *Catal. Today* 117 (2006) 148-155.
- [12] B.R. Wood, J.A. Reimer, A.T. Bell, M.T. Janicke, K.C. Ott. *J. Catal.* 224 (2004) 148-155.
- [13] H. Guesmi, D. Berthomieu, B. Bromley, B. Coq, L. Kiwi-Minsker. *Phys. Chem. Chem. Phys.* 12 (2010) 2873-2878.
- [14] A. Ates, A. Reitzmann. *J. Catal.* 235 (2005) 164-174.
- [15] A. Ates, A. Reitzmann. *Chem. Eng. J.* 134 (2007) 218-227.
- [16] F. Kapteijn, G. Marban, J. RodriguezMirasol, J.A. Moulijn. *J. Catal.* 167 (1997) 256-265.
- [17] E.M. El-Malki, R.A. van Santen, W.M.H. Sachtler. *J. Catal.* 196 (2000) 212-223.
- [18] J. Perez-Ramirez, F. Kapteijn, G. Mul, J.A. Moulijn. *J. Catal.* 208 (2002) 211-223.
- [19] D.A. Bulushev, P.M. Precht, A. Renken, L. Kiwi-Minsker. *Ind. Eng. Chem. Res.* 46 (2007) 4178-4185.
- [20] N. Liu, R. Zhang, B. Chen, Y. Li, Y. Li. *J. Catal.* 294 (2012) 99-112.
- [21] N. Hansen, A. Heyden, A.T. Bell, F.J. Keil. *J. Phys. Chem. C* 111 (2007) 2092-2101.
- [22] A. Heyden, N. Hansen, A.T. Bell, F.J. Keil. *J. Phys. Chem. B* 110 (2006) 17096-17114.
- [23] G.D. Pirngruber, P.K. Roy, R. Prins. *J. Catal.* 246 (2007) 147-157.
- [24] E.V. Kondratenko, V.A. Kondratenko, M. Santiago, J. Pérez-Ramírez. *Appl. Catal., B* 99 (2010) 66-73.
- [25] H. Guesmi, D. Berthomieu, L. Kiwi-Minsker. *J. Phys. Chem. C* 112 (2008) 20319-20328.
- [26] Q. Zhu, R.M. van Teeffelen, R.A. van Santen, E.J.M. Hensen. *J. Catal.* 221 (2004) 575-583.
- [27] E.J.M. Hensen, Q. Zhu, M.M.R.M. Hendrix, A.R. Overweg, P.J. Kooyman, M.V. Sychev, R.A. van Santen. *J. Catal.* 221 (2004) 560-574.
- [28] P. Marturano, L. Drozdov, A. Kogelbauer, R. Prins. *J. Catal.* 192 (2000) 236-247.
- [29] G.D. Pirngruber, P.K. Roy. *Catal. Today* 110 (2005) 199-210.
- [30] G.D. Pirngruber, P.K. Roy, R. Prins. *Phys. Chem. Chem. Phys.* 8 (2006) 3939-3950.
- [31] R. Joyner, M. Stockenhuber. *J. Phys. Chem. B* 103 (1999) 5963-5976.
- [32] L. Kiwi-Minsker, D.A. Bulushev, A. Renken. *J. Catal.* 219 (2003) 273-285.
- [33] J. Pérez-Ramírez, F. Kapteijn, J.C. Groen, A. Doménech, G. Mul, J.A. Moulijn. *J. Catal.* 214 (2003) 33-45.
- [34] A. Zecchina, M. Rivallan, G. Berlier, C. Lamberti, G. Ricchiardi. *Phys. Chem. Chem. Phys.* 9 (2007) 3483-3499.
- [35] S.H. Choi, B.R. Wood, J.A. Ryder, A.T. Bell. *J. Phys. Chem. B* 107 (2003) 11843-11851.
- [36] G.I. Panov, E.V. Starokon, L.V. Pirutko, E.A. Paukshtis, V.N. Parmon. *J. Catal.* 254 (2008) 110-120.
- [37] T. Nobukawa, M. Yoshida, K. Okumura, K. Tomishige, K. Kunimori. *J. Catal.* 229 (2005) 374-388.
- [38] J. Perez-Ramirez, F. Kapteijn, A. Bruckner. *J. Catal.* 218 (2003) 234-238.
- [39] E.M. El-Malki, R.A. van Santen, W.M.H. Sachtler. *Microporous Mesoporous Mater.* 35-6 (2000) 235-244.
- [40] M. Yoshida, T. Nobukawa, S.I. Ito, K. Tomishige, K. Kunimori. *J. Catal.* 223 (2004) 454-464.
- [41] H.-Y. Chen, W.M.H. Sachtler. *Catal. Today* 42 (1998) 73-83.
- [42] M. Rivallan, G. Ricchiardi, S. Bordiga, A. Zecchina. *J. Catal.* 264 (2009) 104-116.
- [43] B. Peters, A.T. Bell, F.J. Keil. *J. Phys. Chem. B* 109 (2005) 1857-1873.
- [44] M. Rivallan, G. Ricchiardi, S. Bordiga, A. Zecchina. *J. Catal.* 264 (2009) 104-116.
- [45] S. Sklenak, P.C. Andrikopoulos, B. Boekfa, B. Jansang, J. Novakova, L. Benco, T. Bucko, J. Hafner, J. Dedecek, Z. Sobalík. *J. Catal.* 272 (2010) 262-274.

Chapter 4

- [46] J.A. Ryder, A.K. Chakraborty, A.T. Bell. *J. Phys. Chem. B* 106 (2002) 7059-7064.
- [47] A. Heyden, A.T. Bell, F.J. Keil. *J. Catal.* 233 (2005) 26-35.
- [48] J. Pérez-Ramírez, M. Santhosh Kumar, A. Brückner. *J. Catal.* 223 (2004) 13-27.
- [49] A.A. Battiston, J.H. Bitter, D.C. Koningsberger. *Catal. Lett.* 66 (2000) 75-79.
- [50] H.A. Xia, K.Q. Sun, Z.M. Liu, Z.C. Feng, P.L. Ying, C. Li. *J. Catal.* 270 (2010) 103-109.
- [51] H.A. Xia, K.Q. Sun, Z.C. Feng, C. Li. *J. Phys. Chem. C* 115 (2011) 542-548.
- [52] H. Xia, K. Sun, K. Sun, Z. Feng, W.X. Li, C. Li. *J. Phys. Chem. C* 112 (2008) 9001-9005.
- [53] A.L. Yakovlev, G.M. Zhidomirov, R.A. van Santen. *J. Phys. Chem. B* 105 (2001) 12297-12302.
- [54] Q. Zhu, E.J.M. Hensen, B.L. Mojet, J. van Wolput, R.A. van Santen. *Chem. Commun.* (2002) 1232-1233.
- [55] A. Heyden, B. Peters, A.T. Bell, F.J. Keil. *J. Phys. Chem. B* 109 (2005) 1857-1873.
- [56] N. Hansen, A. Heyden, A.T. Bell, F.J. Keil. *J. Catal.* 248 (2007) 213-225.
- [57] G. Li, E.A. Pidko, R.A. van Santen, Z.C. Feng, C. Li, E.J.M. Hensen. *J. Catal.* 284 (2011) 194-206.
- [58] E.A. Pidko, E.J.M. Hensen, R.A. van Santen. *Proc. R. Soc. A* 468 (2012) 2070-2086.
- [59] M.F. Fella, I. Onal, R.A. van Santen. *J. Phys. Chem. C* 114 (2010) 12580-12589.
- [60] K. Sun, H. Xia, Z. Feng, R. van Santen, E. Hensen, C. Li. *J. Catal.* 254 (2008) 383-396.
- [61] A. Ates, A. Reitzmann, G. Waters. *Appl. Catal., B* 119-120 (2012) 329-339.
- [62] G.D. Pirngruber, M. Luechinger, P.K. Roy, A. Cecchetto, P. Smirniotis. *J. Catal.* 224 (2004) 429-440.

CHAPTER 5

ON THE NATURE OF ACTIVE SITES AND MECHANISM OF SELECTIVE METHANE OXIDATION OVER Cu/ZSM-5 ZEOLITE

The nature of active sites and the reaction mechanism of methane oxidation over Cu/ZSM-5 catalysts have been studied by periodic DFT calculation. The reactivity of potential binuclear $[\text{Cu}(\mu\text{-O})\text{Cu}]^{2+}$ as well as trinuclear hydroxylated $[\text{Cu}_3(\mu\text{-OH})_2(\mu\text{-O})]^{2+}$ and oxygenated $[\text{Cu}_3(\mu\text{-O})_3]^{2+}$ species towards methane activation is discussed. The initial C–H bond over these catalytic sites proceeds via a homolytic (radical) mechanism resulting in the formation of an OH group bound to the extraframework Cu sites and a CH_3^\bullet radical in the zeolite channel. When the reaction takes place over a binuclear site, in addition to the direct radical rebound resulting in the formation of adsorbed methanol, the formed CH_3^\bullet species may diffuse away from the active site and recombine on basic zeolitic lattice sites resulting in grafted methoxy groups. Neither of the reaction paths over the binuclear complexes allows the removal of methanol in the course of the catalytic cycle. It can only be extracted by a post-catalytic reaction of such surface species with a protic solvent. Two plausible mechanisms of the formation of hydroxylated $[\text{Cu}_3(\mu\text{-OH})_2(\mu\text{-O})]^{2+}$ and oxygenated $[\text{Cu}_3(\mu\text{-O})_3]^{2+}$ cations driven by the self-organization of extraframework species with lower nuclearity are proposed. Trinuclear complexes are much active towards C–H bond cleavage compared to their binuclear counterparts. More importantly, the direct rebound of CH_3^\bullet on these sites is preferred over the separation of the radical pair formed at the initial step. The higher mobility of extraframework oxygens within the Cu clusters of higher nuclearity not only facilitate the formation of methanol but also reduce the barrier for its subsequent elimination from the active site.

5.1. Introduction

In 2005, a novel system based on ZSM-5 zeolite over-exchanged with copper ions has been shown by Groothaert et al. to be able to oxidize methane to methanol at temperatures as low as 100 °C [1]. However, this reaction is not catalytic. It appears that the activation of methane takes place via its stoichiometric reaction with only a fraction of intrazeolitic Cu sites, after which methanol extraction by substantial amounts of a solvent has to be carried out. A later study by Weckhuysen et al. [2] pointed to the necessity of the use of protic solvent for the efficient extraction of methanol. The last step of the process involves regeneration of the Cu/ZSM-5 material by a high-temperature treatment in oxygen. It is important to note that, a similar stoichiometric chemistry was proposed for ZSM-5 zeolites modified with iron [3-6]. Despite consisting of three almost independent processes, the methane to methanol conversion over Cu/ZSM-5 represents a more attractive alternative over than involving Fe/ZSM-5 because of the much lower costs and the direct availability of oxygen as the oxidant instead of N₂O [7-9].

The first studies on the mechanism of methane oxidation and the nature of the active sites in Cu/ZSM-5 zeolite have been reported in the pioneering works performed in the group of Schoonheydt [10-13]. This subject was further explored in the later studies by other researchers [2, 14-16]. The unique reactivity of Cu/ZSM-5 zeolite in the methane oxidation reaction as well as in the catalytic decomposition of NO and N₂O has been attributed to specific extraframework Cu-containing species characterized by an absorption band at 22700 cm⁻¹ in the UV-Vis spectrum of the activated Cu/ZSM-5 [15]. In the original proposal, this band was assigned to bis(μ -oxo)dicopper (II) complexes [Cu(μ -O)₂Cu]²⁺ [10, 17]. However, in a more recent work, Woertink et al. [8] have concluded on the basis of resonance Raman spectroscopy measurements involving ¹⁸O labeled substrates that the specific reactivity of Cu/ZSM-5 is due to the presence of (μ -oxo)dicopper(II) [Cu(μ -O)Cu]²⁺ complexes that do not have counterparts in molecular inorganic chemistry or biochemical systems [18-23]. The structural assignment of the active species in ref. [8] has been supported by time-dependent density functional theory calculations on a rather small cluster model representing a potential structure of intrazeolitic [Cu(μ -O)Cu]²⁺ cations.

Furthermore, Woertink et al. proposed a reaction mechanism for the activation of methane over the oxygen-bridged binuclear Cu sites based on the combination of the experimental and computational results [8]. It was concluded that the initial C–H activation proceeds via a homolytic (radical) dissociation of methane over [Cu(μ -O)Cu]²⁺ resulting in a confined mobile CH₃[•] species and formally an OH[•] radical stabilized between two Cu ions. Subsequent direct rebound of these radicals was proposed to lead to the formation of a methanol molecule strongly adsorbed to two neighboring Cu⁺ species. Because of the strong binding of CH₃OH to two Lewis acid sites, its release from the zeolite voids is hampered. There is however an alternative explanation for the inability to observe the formation of methanol in situ upon the reaction of methane with the activated Cu/ZSM-5.

Due to the only weak correlation of the CH_3^\bullet and $[\text{Cu}(\mu\text{-OH})\text{Cu}]^{2+}$ radical pair formed by the reaction of methane with the binuclear extraframework Cu site, the CH_3^\bullet can diffuse from the active complex into the zeolite channel and then recombine with any available basic site. This may potentially lead to the formation of a wide range of grafted methoxy species in the zeolite voids as suggested by Vanelderen et al. [14]. The low efficiency of the direct rebound mechanism resulting from the escape of a radical intermediate from the reaction center has previously been discussed for oxidation reactions over coordination compounds [24, 25]. Nevertheless, to the best of our knowledge such a reaction path has not been considered before for methane activation on Cu/ZSM-5 zeolite.

Due to the high heterogeneity of extraframework sites in Cu-containing zeolites, one cannot exclude that other types of Cu species can play key roles in selective methane oxidation. The stoichiometric nature of the methane oxidation reaction over binuclear Cu sites and more specifically the difficulty to directly obtain the methanol product in the course of the reaction can be ascribed to the low mobility of the extraframework oxygen ion bridging two Cu^{2+} ions and, related, to the very high Lewis acidity of the dual Cu^+ site formed at the end of the reaction. A selective synthesis of alternative Cu-containing sites with improved characteristics in the zeolite confined space can determine a significant progress towards the development of an improved methane oxidation system based on Cu/ZSM-5 materials.

Besides mononuclear and binuclear copper complexes attracting most of the attention as the potential sites for C–H activation, Cu-containing clusters with a higher degree of nuclearity (e.g. trinuclear and tetranuclear copper complexes) have also been considered as the active species in chemocatalytic and biological systems [22, 26]. Multinuclear copper complexes are recently in the center of attention of many research groups because of their similarity to the active sites of different metalloproteins [27, 28]. Chan et al. provided evidence that trinuclear bis(μ_3 -oxo)trinuclear copper(II, II, III) complex can be present in the pMMO enzyme and that this particular cluster is responsible for the mediation of the dioxygen chemistry and O–transfer during the alkane hydroxylation [29]. These authors have designed and successfully synthesized a model tricopper coordination complex that exhibit similar spectroscopic properties and chemical reactivity to the putative trinuclear active site in the pMMO [30-32]. These experimental results were further supported by a computational study [33]. The possibility of the presence of trinuclear extraframework Cu sites in Cu/ZSM-5 zeolite has also been discussed previously [26, 34]. Solomon et al. demonstrated that the specific spectroscopic features of Cu/ZSM-5 evidence the exchange coupling between several oxidized Cu species in mixed-valent state. This is characteristic for multinuclear extraframework complexes. This proposition is indirectly supported by the computational study reported by Yoshizawa and co-workers that indicated a higher reactivity of mixed-valent Cu(II/III) species compared to those containing only Cu(III) centers [35]. Very recently, a group of Lercher has succeeded in synthesis of a Cu-containing zeolite material exhibiting reactivity towards methane activation that is an order of magnitude higher than that of the previously reported materials [36]. Subsequent

extensive characterization of these materials evidenced the presence of Cu-containing complexes with nuclearity higher than 2 confined within the zeolite pores. These findings motivated us to investigate the possibility of the formation and reactivity of alternative multinuclear Cu sites in ZSM-5 zeolite.

In this chapter, a detailed computational study of the reaction mechanism of methane activation over different potential extraframework Cu sites in ZSM-5 zeolite is reported. The chapter is organized as follows: first, the results of DFT calculations on the structural properties, stability and reactivity of the binuclear (μ -oxo)dicopper(II) $[\text{Cu}(\mu\text{-O})\text{Cu}]^{2+}$ extraframework cations will be discussed. This will be followed by a section the possibility of the formation of larger hydroxylated and oxygenated trinuclear Cu species and their reactivity towards methane activation will be discussed.

5.2. Computational methods

For the quantum-chemical calculations we used the same method and VASP software as previously described in Chapter 2. The orthogonal unit cell with lattice parameters of $a = 20.241$, $b = 20.015$, and $c = 13.439$ Å as optimized with VASP for an all-silica MFI periodic model was used for all periodic simulations, which in good agreement with the experimental data for calcined ZSM-5 [37]. For the simulations of the active sites and the reaction mechanism to compensate for the charge of the extraframework copper complex two of the Si atoms were substituted with Al. A description of the location of the active site and the Al substitutions follows further in the text. Geometry optimizations were carried out with plane wave basis set cutoff of 400 eV. And the geometry optimizations were performed requiring the forces on all atoms to be less than 0.05 eV/Å. The transition states optimization and the frequency analysis of the stationary points were also performed by the same means as in Chapter 3. The transition states were confirmed by the presence of a single imaginary frequency corresponding to the reaction path.

5.3. Results and discussion

5.3.1. Binuclear $[\text{Cu}(\mu\text{-O})\text{Cu}]^{2+}$ in ZSM-5 zeolite

5.3.1.1. Structure and location

Two distinct configurations of the $[\text{Cu}(\mu\text{-O})\text{Cu}]^{2+}$ complex in ZSM-5 micropores were considered, namely the γ eight-membered ring (8MR) site located within the sinusoidal channel, and the so-called I10 site representing a ten-membered ring (10MR) at the intersection of the straight and sinusoidal channels (Figure 5.1). These configurations were selected as representative examples because of the different confinement exerted by the local zeolite structure onto the extraframework Cu-containing species. Furthermore, the distribution of lattice Al ions is very different for these two locations. Whereas in the case of the γ - site, framework aluminums are separated by three silicon-occupied oxygen tetrahedra, the negatively charged $[\text{AlO}_2]^-$ lattice sites within the I10 site are located at the next-nearest positions. Nevertheless, despite very different local zeolite configuration, the

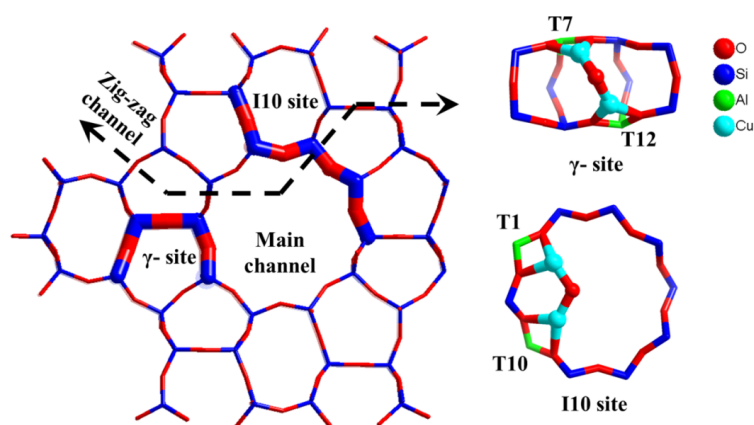


Figure 5.1. Schemetical representation of ZSM-5 framework and selected locations for accommodation extraframework Cu-containing species.

computed energies of different structures and reaction intermediates considered for these two sites usually do not deviate by more than 26 kJ/mol. Only in the cases of specific reaction intermediates capable of forming strong hydrogen bonds with the lattice oxygen ions, such as hydroxylated Cu complexes or methanol an additional stabilization of ca. 20 kJ/mol was observed in the case of the more confined γ - site (evaluated based on Dr. Vassilev's results). This implies, that the reactivity of $[\text{Cu}(\mu\text{-O})\text{Cu}]^{2+}$ depends only slightly on the geometrical properties and the fine details of the chemical composition of the zeolite site. Therefore, the reactivity of Cu sites stabilized only at the γ - site was considered further.

5.3.1.2. Methane activation by binuclear $[\text{Cu}(\mu\text{-O})\text{Cu}]^{2+}$ complex

The initial activation of methane proceeds via a homolytic mechanism over $[\text{Cu}(\mu\text{-O})\text{Cu}]^{2+}$. This reaction involves the homolytic (radical) dissociation of a C–H bond over the extraframework bridging oxygen center and results in the formation of a hydroxyl group bridging two Cu centers and a CH_3^\bullet radical. The computed activation barrier for this step is 93 kJ/mol that is somewhat higher than the experimentally determined value of 66 kJ/mol [19]. This elementary step can be viewed as an abstraction of an H (spin-down, \downarrow , $S = -1/2$) radical by a biradical $[\text{Cu}(\mu\text{-O})\text{Cu}]^{2+}$ cation ($\uparrow\uparrow$, $S = 1$) that leaves behind a CH_3^\bullet species (spin-up, \uparrow , $S = 1/2$). This process is accompanied by a single electron transfer resulting in the partial reduction of one of the Cu centers and the formation of a hydroxyl. The $S = 1$ triplet state of the system is preserved in the course of this reaction. The thus formed partially reduced $[\text{Cu}^{\text{I}}(\mu\text{-OH})\text{Cu}^{\text{II}}]^{2+\bullet}$ (\uparrow) and CH_3^\bullet (\uparrow) represent a ferromagnetically coupled radical pair. The reaction energy for methane dissociation over $[\text{Cu}(\mu\text{-O})\text{Cu}]^{2+}$ equals 61 kJ/mol.

In principle, the formation of methanol can be readily achieved by a direct rebound of the formed radicals. However, such a process should proceed over a singlet potential energy,

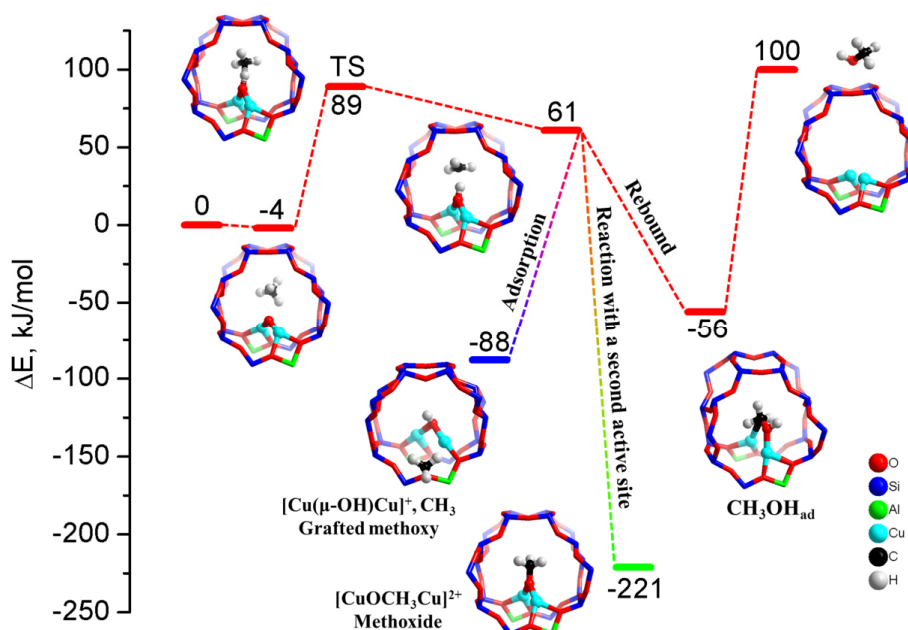


Figure 5.2. Reaction paths for methane oxidation over binuclear $[\text{Cu}(\mu\text{-O})\text{Cu}]^{2+}$ site.

because of the closed-shell ground state of the reaction product $[\text{Cu}^{\text{I}}(\text{CH}_3\text{OH})\text{Cu}^{\text{I}}]^{2+}$. Thus, direct rebound would involve a spin-crossing transition similar to those discussed for the case of the N_2O decomposition over binuclear Fe/ZSM-5 (Chapter 4). This change of the spin state involves a decoupling of the radical pair that can readily be achieved by spatial separation of the interacting species.

If the radicals formed after the initial methane activation become decoupled, the reaction outcome will not be uniquely determined anymore (Figure 5.2). Although there is still a possibility for the methyl radical to diffuse back to the original partially reduced Cu complex resulting in the formation of the $[\text{Cu}(\text{CH}_3\text{OH})\text{Cu}]^{2+}$ adsorption complex, The computed reaction energy (ΔE) for the direct rebound is -117 kJ/mol. A number of alternative equally possible reaction channels become available. CH_3^\bullet can recombine with one of the open Cu sites resulting in the $[\text{CH}_3\text{-Cu}(\mu\text{-OH})\text{Cu}]^{2+}$ cation that can be viewed as a product of heterolytic dissociation of methane activation over a Cu–O acid-base pair in $[\text{Cu}(\mu\text{-O})\text{Cu}]^{2+}$. This intermediate can then interconvert into $[\text{Cu}(\text{CH}_3\text{OH})\text{Cu}]^{2+}$ with an activation barrier of only 50 kJ/mol. These results imply that the rebound of a CH_3^\bullet fragment with any site of the partially reduced $[\text{Cu}(\mu\text{-OH})\text{Cu}]^{2+}$ will ultimately lead to the thermodynamically preferred adsorption complex of methanol with a pair of reduced Cu^+ sites $[\text{Cu}(\text{CH}_3\text{OH})\text{Cu}]^{2+}$.

Another plausible alternative is the recombination of CH_3^\bullet with basic oxygen atoms of the zeolite framework next to the original active complex. The recombination in this case involves a single-electron transfer reaction from the methyl radical to the extraframework

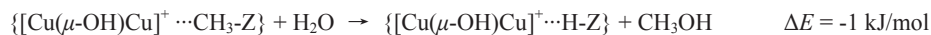
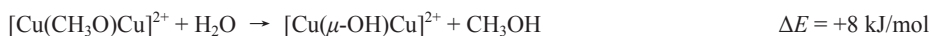
Cu species resulting in the reduction of the latter to $[\text{Cu}^{\text{I}}(\mu\text{-OH})\text{Cu}^{\text{I}}]^+$ and the formation of a zeolitic methoxy group $\text{CH}_3\text{-Z}$ that can formally be regarded as a CH_3^+ species charge-compensated by a lattice anionic site (adsorption route in Figure 5.2). This path is more favourable than the direct rebound mechanism and is characterized by a reaction energy (ΔE) of -149 kJ/mol. In order to form a methanol molecule, the lattice-bound CH_3 group has to transform into the intermediates describe above for the rebound paths. The associated chemical transformations are very unfavourable.

The most exothermic reaction path ($\Delta E = -282$ kJ/mol) identified here may be realized when CH_3^* completely leaves the initial active site and recombines with another activated distant $[\text{Cu}(\mu\text{-O})\text{Cu}]^{2+}$ active complex (reaction with a second active site route in Figure 5.2). This route results in two partially reduced independent binuclear Cu complexes containing bridging OH and OCH_3 groups, respectively, at the original methane activation site and at the site of the radical recombination. It is important to note that although the copper centers in these partially reduced complexes have formally different oxidation states (+1 and +2), the results of DFT calculations evidence a delocalization of the unpaired electron over the extraframework species making thus both Cu ions indistinguishable. The outcome of this reaction path is a permanent separation of the CH_3 and OH groups. Their recombination can proceed only via the reverse process involving the formation of the free CH_3^* radical intermediate that shows reaction energy of more than 150 kJ/mol. Therefore, taking into account the distant location of the two reaction intermediates, their recombination resulting in the formation of molecular methanol appears to be very unlikely.

Thus, among the four paths considered, only two involving a rebound of the methyl radical and the binuclear Cu site may potentially lead to the formation of an adsorbed CH_3OH molecule (rebound route in Figure 5.2). However, desorption of methanol from the strongly Lewis acidic dual Cu^+ site is very unfavourable. The computed desorption energy in this case is 156 kJ/mol. To close the catalytic cycle of the selective oxidation of methane to methanol, the methanol product must be removed from the catalyst and the original active complex should be regenerated. The direct desorption of methanol can only occur from the $[\text{Cu}(\text{CH}_3\text{OH})\text{Cu}]^{2+}$ intermediate. This is an endothermic process with a relatively high barrier. Two other radical recombination routes result in the reaction intermediates from which not only the CH_3OH desorption but even its formation is not possible.

5.3.1.3. Extraction of methanol

The results above imply that methane activation by extraframework $[\text{Cu}(\mu\text{-O})\text{Cu}]^{2+}$ may result in a number of reaction intermediates that are strongly bound to different sites in Cu/ZSM-5 either via covalent or coordination bonds. Besides the strongly adsorbed molecular methanol, lattice- and Cu-bound methoxy groups can also be formed. In principle, the latter species can be hydrolysed upon the reaction with protic solvents or those containing (trace) water resulting in methanol. We considered these possibilities in our DFT calculations and the results are summarized below:



In the case of the $[\text{Cu}(\text{CH}_3\text{OH})\text{Cu}]^{2+}$ adsorption complex, water can also promote the product elimination via a substitution reaction:



The computed reaction energies for the hydrolysis of grafted methoxy intermediates indicate that these processes can result in the formation of methanol upon the aqueous extraction or steaming of the Cu/ZSM-5 after its reaction with methane. In principle, the Cu-bridged methoxide intermediate $[\text{Cu}(\text{CH}_3\text{O})\text{Cu}]^{2+}$ can be decomposed by the interaction with any protic solvent via a protonation reaction. The substitution of the adsorbed CH_3OH can potentially be promoted by any strongly coordinating solvent. When water is considered, the computed reaction energy for this step equals to -3 kJ/mol. These results are in line with the experimental observations indicating that the extraction of methanol from the zeolite necessitate the use of polar coordinating solvents [13].

The results presented so far provide a plausible explanation for the available experimental observations [9]. It has been demonstrated that the activation of methane over a Cu/ZSM-5 zeolite activated at high temperature in $^{18}\text{O}_2$ atmosphere with subsequent extraction using unlabelled ethanol yields only 75% of $\text{CH}_3^{18}\text{OH}$, while 25% of the yield is represented by the label-free methanol. Our computational results imply that $\text{CH}_3^{18}\text{OH}$ is formed by the substitution reaction within $[\text{Cu}(\text{CH}_3\text{OH})\text{Cu}]^{2+}$ or by the protonation of a bridging methoxide moiety in $[\text{Cu}(\text{CH}_3\text{O})\text{Cu}]^{2+}$ or any other oxygenated copper species. The presence of substantial amounts of unlabelled methanol can be explained by the protonation of framework-bound $\text{CH}_3\text{-Z}$ species formed within the “adsorption route” shown in Figure 5.2.

5.3.2. Trinuclear Cu sites in Cu/ZSM-5

5.3.2.1. Formation of trinuclear extraframework Cu cations

The results presented above suggest that methane oxidation by binuclear $[\text{Cu}(\mu\text{-O})\text{Cu}]^{2+}$ extraframework cations cannot be performed in a catalytic manner because of the formation of very stable reaction intermediates that require the addition of co-reactants for the extraction of methanol product from the microporous matrix. In principle, extraframework copper complexes that can potentially be formed in the zeolite channels are not limited to this particular binuclear complex. One expects a very heterogeneous speciation of copper in the actual activated Cu/ZSM-5 catalysts. Indeed, the thermochemical activation of an ion-exchanged zeolite initially containing predominantly mononuclear species may result in their self-organization into diverse multinuclear hydroxylated and oxygenated cationic clusters. In principle, they can also contribute to the reactivity of Cu/ZSM-5 towards methane activation. More important is that in the light of

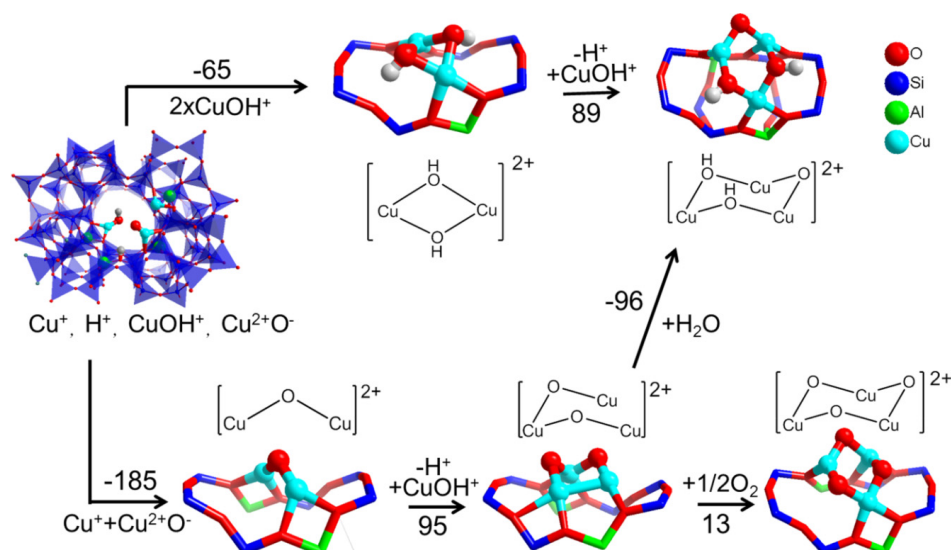


Figure 5.3. The self-organization path I resulting in the formation of trinuclear Cu-containing extraframework complexes in ZSM-5 zeolite.

the above results, bulkier multinuclear oxygenated copper species may be beneficial for the reaction considered. On one hand, mobility of extraframework oxygen ions in the cationic Cu cluster with nuclearity higher than 2 will be increased. This would facilitate the initial CH activation step. On the other hand, because of the decreased space in the channels due to the presence of larger multinuclear cations, the direct rebound path can become promoted. Furthermore, the Lewis acidity of the Cu centers in the resulting partially reduced multinuclear complex will not be as high as that of the dual Cu⁺ site. This factor would facilitate the removal of methanol from the active site at the end of the reaction.

In view of these considerations and inspired by recent experimental findings [47], we also considered the possibility of the formation of trinuclear Cu-containing cations in Cu/ZSM-5 zeolite. In this study, only the 8MR at γ - site was considered for the stabilization of extraframework cationic clusters that has been shown to be the preferred site for the stabilization of a wide range of iron-containing complexes (Chapter 2).

The formation of bi- and multinuclear Cu complexes is assumed to proceed via a self-organization of different mononuclear Cu^I/Cu^{II} containing cationic species, such as Cu⁺, Cu²⁺O⁻, CuOH⁺, and their reactions with residual zeolitic Brønsted acid sites. Following the discussion in Chapter 2 and in the previous literature [38] on the general nature of the phenomenon of self-organization of oxygenated cations in high-silica zeolites, one can expect that two isolated CuOH⁺ cations can assemble into binuclear hydroxylated [Cu(μ-OH)₂Cu]²⁺ complex. On the other hand, the binuclear [Cu(μ-O)Cu]²⁺ complex discussed in the previous section can be formed via the interaction between Cu⁺ and Cu²⁺O⁻ cationic species. The computed reaction energies for these transformations are summarized in Figure 5.3 along with the optimized structures of the complexes involved.

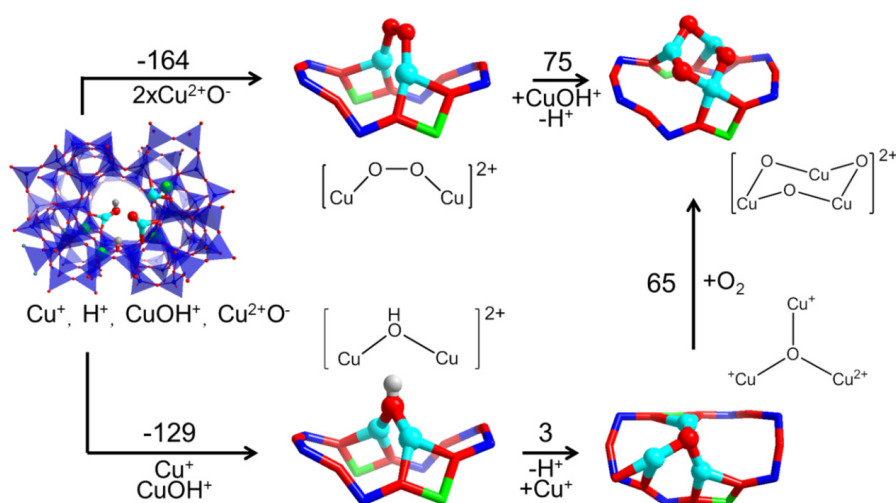


Figure 5.4. The self-organization path II resulting in the formation of trinuclear Cu-containing extraframework complexes in ZSM-5 zeolite.

Both reactions are found to be thermodynamically favorable. The former process shows a reaction energy of -65 kJ/mol, whereas the assembly of the isolated Cu^+ and Cu^{2+}O^- lowers the total energy of the system by -185 kJ/mol. The high reactivity of O^- radical of Cu^{2+}O^- is responsible for fast self-organization. When the loading of copper in the zeolite is high, the hydroxylated $[\text{Cu}(\mu\text{-OH})_2\text{Cu}]^{2+}$ complex can further react with an additional CuOH^+ cation originally stabilized at a distant zeolite site leaving behind a Brønsted acid proton and resulting in a trinuclear hydroxylated $[\text{Cu}_3(\mu\text{-OH})_2(\mu\text{-O})]^{2+}$ cluster. The last reaction step proceeds with a reaction energy of 89 kJ/mol. The formation of oxygenated trinuclear $[\text{Cu}_3(\mu\text{-O})_2]^{2+}$ complex involves a deprotonation-assisted aggregation between binuclear $[\text{Cu}(\mu\text{-O})\text{Cu}]^{2+}$ complex and mononuclear CuOH^+ . This reaction is also endothermic and is characterized by a ΔE value of 95 kJ/mol. This cluster can be further oxidized with O_2 towards a $[\text{Cu}_3(\mu\text{-O})_3]^{2+}$ six-membered ring complex characterized by a chair conformation with three Cu centers pointing towards lattice oxygen ions of the γ -site ($\Delta E = -22$ kJ/mol).

An alternative mechanism involves the aggregation of two mononuclear Cu^{2+}O^- into a binuclear complex (Figure 5.4). In this case, two possible configurations $[\text{Cu}(\mu\text{-}1,2\text{-peroxo})\text{Cu}]^{2+}$ and $[\text{Cu}(\mu\text{-O})_2\text{Cu}]^{2+}$ can potentially be formed. At the γ -site the peroxo-bridged structure is 35 kJ/mol preferred over the latter complex. The formation of the binuclear cluster in this case is strongly favorable thermodynamically ($\Delta E = -164$ kJ/mol). At the next step, a trinuclear $[\text{Cu}_3(\mu\text{-O})_3]^{2+}$ species can be formed via an endothermic process ($\Delta E = 75$ kJ/mol) that proceeds via a deprotonation-assisted reaction of CuOH^+ with $[\text{Cu}(\mu\text{-}1,2\text{-peroxo})\text{Cu}]^{2+}$. Another much more realistic mechanism for the formation of trinuclear Cu cations is initiated by an exothermic aggregation ($\Delta E = -129$ kJ/mol) of rather stable isolated Cu^+ and CuOH^+ cations into a hydroxyl bridged $[\text{Cu}(\mu\text{-OH})\text{Cu}]^{2+}$ structure. Facile exchange of the bridging proton in this complex with

another exchangeable Cu^+ ion yields a trinuclear $[\text{Cu}_3(\mu_3\text{-oxo})]^{2+}$ ($\Delta E = 3$ kJ/mol). Its oxidation with molecular O_2 leads to $[\text{Cu}_3(\mu\text{-O})_3]^{2+}$ ($\Delta E = 65$ kJ/mol). For this trinuclear species, the Cu ions can be in the formal +3 state, however, the actual electronic configuration can be different. Since the in-depth investigation of the electronic configuration of copper centers in different extraframework complexes was out of scope of this study, we did not perform it. In the text below, formal valences are considered.

These results imply that despite a generally higher stability of the binuclear Cu complexes, the hydroxylated $[\text{Cu}_3(\mu\text{-OH})_2(\mu\text{-O})]^{2+}$ and oxygenated $[\text{Cu}_3(\mu\text{-O})_3]^{2+}$ trinuclear cations can potentially be formed in Cu/ZSM-5 zeolite upon the high temperature calcination. The computed reaction energies suggest that the mechanisms involving self-organization of only rather stable Cu^+ and CuOH^+ species are the most probable ones. The limited mobility of these species under ambient conditions requires the use of high temperatures during the catalyst activation.

5.3.2.2. Methane activation over trinuclear Cu sites in ZSM-5

Both $[\text{Cu}_3(\mu\text{-OH})_2(\mu\text{-O})]^{2+}$ and $[\text{Cu}_3(\mu\text{-O})_3]^{2+}$ cations contain an exposed bridging oxygen ligand that can play a role in methane activation. The DFT-computed reaction energy diagrams for methane oxidation over the hydroxylated and oxygenated trinuclear Cu clusters are shown in Figures 5.5 and 5.6, respectively. Let us first consider the reaction over the $[\text{Cu}_3(\mu\text{-OH})_2(\mu\text{-O})]^{2+}$ complex (Figure 5.5). Because this cluster is composed of three formally Cu^{2+} species, it can be present in two electronic configurations, namely high ($S = 3/2$) and low-spin ($S = 1/2$) states. For the initial complex, the energy difference between these two electronic configurations is only 9 kJ/mol with the high-spin state being preferred. Molecular adsorption of methane on $[\text{Cu}_3(\mu\text{-OH})_2(\mu\text{-O})]^{2+}$ is very weak ($\Delta E_{\text{ads}} = -4$ kJ/mol independently of the spin state of the copper complex). Similar to the case of the binuclear Cu sites discussed above, the CH_4 molecule is activated via a homolytic (radical) C–H bond cleavage with a barrier of 71 kJ/mol and reaction energy of 49 kJ/mol ($S = 3/2$) resulting in a CH_3^\cdot radical and a $[\text{Cu}_3(\mu\text{-OH})_3]^{2+}$ extraframework cation. Subsequent formation of adsorbed methanol via a rebound mechanism and its removal from the copper complex is unfavorable over the high-spin potential energy surface (PES). On the other hand, in spite of a somewhat higher barrier for the initial dissociation of methane computed for the low-spin ($S = 1/2$) state of the reactive complex, the reaction products appear to be stabilized by about 30 kJ/mol in this electronic configuration compared to the $S = 3/2$ case. This implies that the initial C–H activation over $[\text{Cu}_3(\mu\text{-OH})_2(\mu\text{-O})]^{2+}$ involves a spin-crossing transition ($S = 3/2 \rightarrow S = 1/2$). The resulting radical pair in the $S = 1/2$ electronic configuration can readily recombine at the next reaction step resulting in an adsorbed methanol molecule. This step lowers the total energy of the system by 191 kJ/mol. Because of the substantial coordinative saturation of the involved Cu ions, CH_3OH is rather weakly bound to only a single copper center in the partially reduced $[\text{Cu}_3(\mu\text{-OH})_2]^{2+}$ cluster containing indistinguishable Cu^{II} and Cu^{I} centers. As a result, the elimination of the methanol molecule from the extraframework site proceeds with a desorption energy of

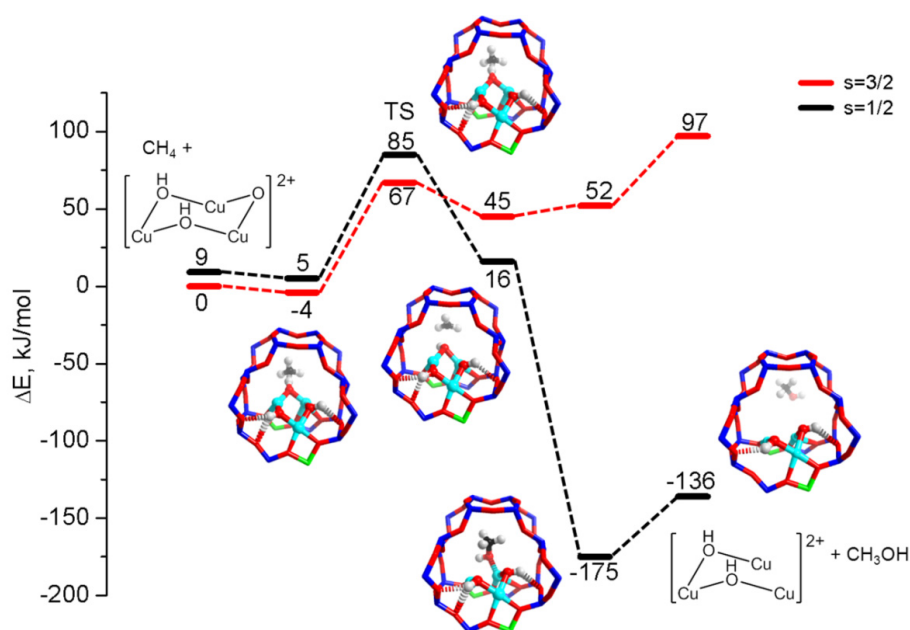


Figure 5.5. Reaction paths for methane oxidation to methanol over trinuclear hydroxylated $[\text{Cu}_3(\mu\text{-OH})_2(\mu\text{-O})]^{2+}$ complex in the high ($S = 3/2$) and low-spin ($S = 1/2$) electronic configurations.

only 39 kJ/mol. The regeneration of the initial active complex can be accomplished by oxidation in O_2 . The reaction $[\text{Cu}_3(\mu\text{-OH})_2]^{2+} + 1/2\text{O}_2 \rightarrow [\text{Cu}_3(\mu\text{-OH})_2(\mu\text{-O})]^{2+}$ is slightly endothermic and is characterized by a computed ΔE value of 19 kJ/mol.

The oxygenated trinuclear $[\text{Cu}_3(\mu\text{-O})_3]^{2+}$ cationic complex promotes methane in a similar manner (Figure 5.6). The ground high-spin state ($S = 3/2$) for this species is only 6 kJ/mol less stable compared to the low-spin electronic configuration. The initial C–H activation in this case proceeds with a barrier of 63 kJ/mol that is slightly lower than that computed for the case of $[\text{Cu}_3(\mu\text{-OH})_2(\mu\text{-O})]^{2+}$. The reaction energy for the formation of the $\text{CH}_3^\bullet \cdots [\text{Cu}_3(\mu\text{-OH})_2(\mu\text{-O})]^{2+}$ radical pair is 41 kJ/mol. In contrast to the reaction promoted by $[\text{Cu}_3(\mu\text{-OH})_2(\mu\text{-O})]^{2+}$, in this case the reaction intermediates and transition states involved in the initial C–H activation corresponding to the low- and high-spin PESs are almost identical in energy. The spin-crossing can take place only at the stage of the rebound of the CH_3 radical with the partially reduced extraframework cluster. It is important to note that the formation of methanol is strongly favored thermodynamically for both electronic configurations. Nevertheless, whereas the reaction energy of the rebound step over the $S = 3/2$ PES is -220 kJ/mol, a spin-crossing transition allows a further stabilization of the system containing the adsorbed CH_3OH by additional 33 kJ/mol (Figure 5.6). After methanol is removed from the partially reduced adsorption site ($\Delta E = 86$ kJ/mol), the initial oxygenated $[\text{Cu}_3(\mu\text{-O})_3]^{2+}$ active complex can be regenerated by an O_2

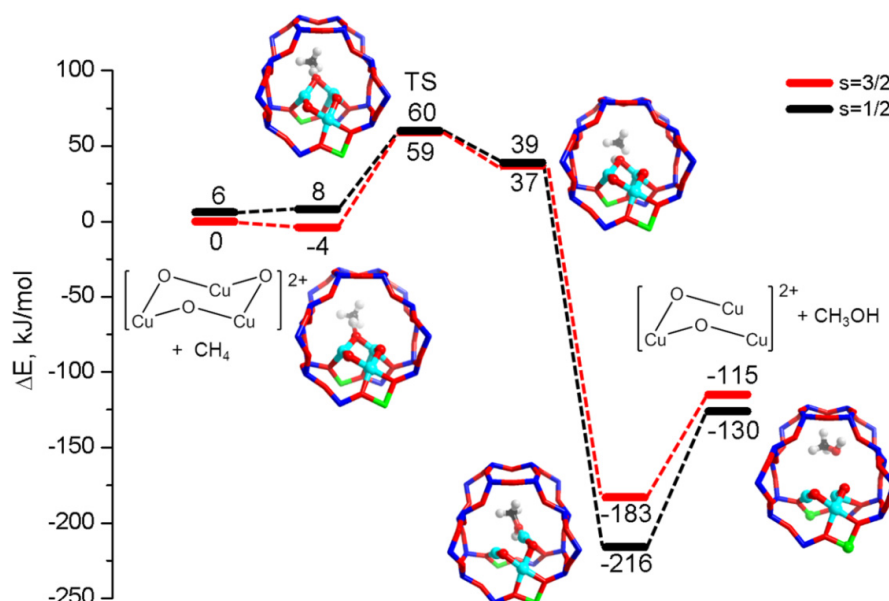


Figure 5.6. Reaction path for methane oxidation to methanol over trinuclear oxygenated $[\text{Cu}_3(\mu\text{-O})_3]^{2+}$ complex in the high ($S = 3/2$) and low-spin ($S = 1/2$) electronic configuration.

treatment. The computed reaction energy for this step is very close to that determined for the hydroxylated cluster and it equals to 13 kJ/mol.

In line with the discussion above for the case of the binuclear Cu complexes, in addition to the direct CH_3^\bullet rebound with the extraframework OH species, the recombination of the methyl radical formed at the initial methane activation step can take place with other sites present in the zeolite micropores. Because of the increased nuclearity of the active complex, we assume that the probability of the presence of several multinuclear extraframework Cu species near each other in high-silica zeolites is quite low. Therefore, the most probable alternative radical recombination path involves the “adsorption” of CH_3^\bullet onto basic oxygens from lattice anionic $[\text{AlO}_2]^-$ units accompanied with a single-electron transfer from the hydrocarbon moiety to the copper cluster. Although this reaction is preferred over the $[\text{Cu}(\mu\text{-O})\text{Cu}]^{2+}$ complex (Figure 5.2), DFT calculations demonstrate that the respective $\{[\text{Cu}_3(\mu\text{-O})_2(\mu\text{-OH})]^\bullet \cdots \text{CH}_3\text{-Z}\}$ intermediate in the case of the trinuclear active site is 60-90 kJ/mol less stable than the desired methanol adsorption complex $[\text{Cu}_3(\mu\text{-O})_2(\text{CH}_3\text{OH})]^{2+}$.

Thus, the computational results presented so far imply that trinuclear hydroxylated and oxygenated copper clusters can contribute to the activity of Cu/ZSM-5 zeolite in selective methane oxidation. The minimum energy reaction paths over the bi- and trinuclear Cu complexes are compared in Figure 5.7. The activation barrier for the initial C–H bond cleavage over trinuclear $[\text{Cu}_3(\mu\text{-OH})_2(\mu\text{-O})]^{2+}$ and $[\text{Cu}_3(\mu\text{-O})_3]^{2+}$ sites is 20-30 kJ/mol lower than that determined for the binuclear $[\text{Cu}(\mu\text{-O})\text{Cu}]^{2+}$ complex. It is important to note that

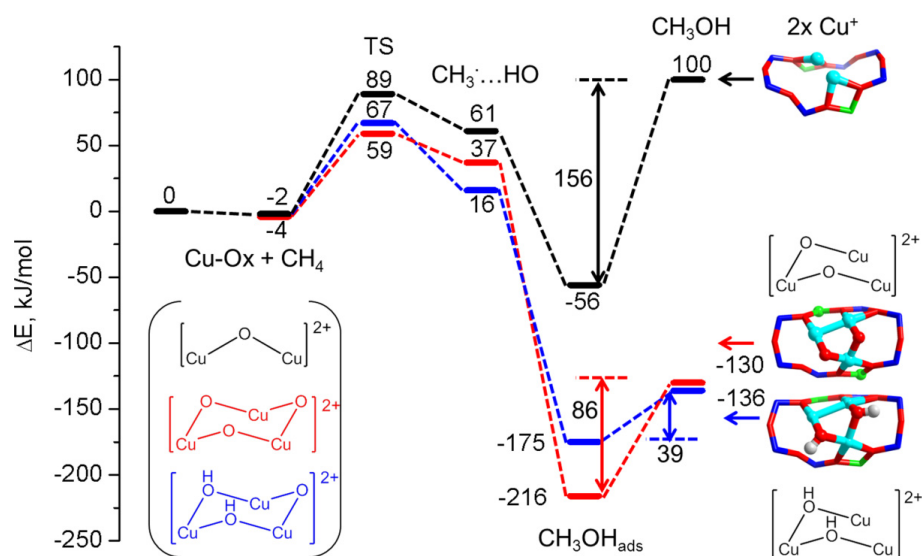


Figure 5.7. Comparison of the computed reaction energy diagrams for methane oxidation to methanol over binuclear $[\text{Cu}(\mu\text{-O})\text{Cu}]^{2+}$ and trinuclear $[\text{Cu}_3(\mu\text{-OH})_2(\mu\text{-O})]^{2+}$ and $[\text{Cu}_3(\mu\text{-O})_3]^{2+}$ sites.

the values obtained for the former sites is in a quantitative agreement with the apparent activation barrier determined experimentally ($E_{app} = 66$ kJ/mol [19]). The formation of the radical pair is also more favorable thermodynamically over the trinuclear clusters. More important is that the direct rebound of the CH_3 radical with the extraframework hydroxyl group is the preferred reaction path in this case, whereas alternative radical recombination paths dominate when the reaction is performed over $[\text{Cu}(\mu\text{-O})\text{Cu}]^{2+}$. Finally, the desorption of methanol from the partially reduced copper site is a much more favorable process for the former type of active complexes. The DFT computed desorption energies are equal to 39 and 86 kJ/mol for the trinuclear hydroxylated and oxygenated complexes, respectively, whereas desorption of methanol from the dual Cu^+ species proceeds with an energy change of 156 kJ/mol.

Thus, it is important to reconsider the generally accepted view on the nature of the active component in conventional Cu/ZSM-5 materials. All experimental studies reported up to date stress that the formation of an active material necessitates its activation in O_2 atmosphere at a very high temperature to transform reduced exchangeable Cu ions into the oxidized $[\text{Cu}(\mu\text{-O})\text{Cu}]^{2+}$ form. Moreover, the catalyst must be cooled down to the temperature, at which methane activation will be performed, again in the presence O_2 atmosphere to avoid the decomposition of these active species. According to the $^{18}\text{O}_2$ -TPD results of Schoonheydt et al. [20], They proposed that the oxidation of a Cu^+ pair to $[\text{Cu}(\mu\text{-O})\text{Cu}]^{2+}$ by O_2 is via a $\mu\text{-}(\eta^2:\eta^2)$ peroxo dicopper (II) $[\text{Cu}_2(\text{O}_2)]^{2+}$ species as precursor. The two additional electrons required for formation of the $[\text{Cu}(\mu\text{-O})\text{Cu}]^{2+}$ active

site from $[\text{Cu}_2(\text{O}_2)]^{2+}$ are provided by spectator Cu^+ ions in neighboring ion-exchanged sites. The second O atom is incorporated into the zeolite lattice. This is in an apparent contradiction with our DFT results. The oxidation of a Cu^+ pair to $[\text{Cu}(\mu\text{-O})\text{Cu}]^{2+}$ is a very exothermic process. The corresponding reaction energy change equals to -217 kJ/mol evidencing a very high stability of the oxygenated binuclear sites. On the other hand, the energetics of the elementary steps involved in the formation of the reactive trinuclear complexes reflect much better the experimental procedure. In this study we considered only a very small number of potential multinuclear Cu sites stabilized at a specific zeolite position. Nevertheless, the presented results strongly indicate the importance of aggregated Cu complexes with a nuclearity higher than 2 for the selective oxidation of methane and provide a theoretical support to the unexpected experimental findings obtained in the group of Lercher [47].

Summarizing, trinuclear hydroxylated and oxygenated extraframework Cu-containing cations in ZSM-5 are promising active sites for the oxidation of methane under mild conditions. The development of synthetic methodologies for a controlled and selective formation of such complexes within zeolite micropores will open an avenue towards the development of an efficient and economic technology for the direct conversion of natural gas to methanol.

5.4. Conclusion

An in-depth computational study on the nature of active sites and the reaction mechanism for methane oxidation over Cu/ZSM-5 zeolite is presented. Methane activation over the extraframework Cu-containing complexes proceeds via a homolytic (radical) C–H dissociation mechanism. This process leads to the formation of a free CH_3 radical species and therefore several possible reaction destinations have been discussed. For the reaction taking place over binuclear $[\text{Cu}(\mu\text{-O})\text{Cu}]^{2+}$ site, the formation of adsorbed molecular methanol can only be obtained by the rebound of CH_3 and bridging OH fragments over binuclear Cu site. However, CH_3OH desorption is highly endothermic and results in strongly Lewis acidic dual Cu^+ site which is very unfavourable. The most favourable reaction path is the formation of a methoxide group bridging two extraframework Cu ions via the CH_3 reaction with a second $[\text{Cu}(\mu\text{-O})\text{Cu}]^{2+}$ active site. In this case extraction of methanol is only possible with protic or water solvent, or by steaming. Thus, our DFT results indicate that selective methane oxidation to methanol performed in a catalytic manner over binuclear $[\text{Cu}(\mu\text{-O})\text{Cu}]^{2+}$ seems unpractical.

Alternatively, the plausible mechanisms of formation trinuclear hydroxylated $[\text{Cu}_3(\mu\text{-OH})_2(\mu\text{-O})]^{2+}$ and oxygenated $[\text{Cu}_3(\mu\text{-O})_3]^{2+}$ complexes generated by self-organization and aggregation behaviors of mononuclear and binuclear cationic species have been proposed. This investigation is motivated by the characterization and reactivity of multinuclear copper clusters in inorganic chemistry and enzymes. The calculated rather low reaction energy of formation trinuclear copper complexes indicates that the

aggregation process driven by coordination unsaturation of extraframework species with lower nuclearity is likely and can occur at high temperature in the presence of oxygen. Moreover, the reactivity of trinuclear hydroxylated $[\text{Cu}_3(\mu\text{-OH})_2(\mu\text{-O})]^{2+}$ and oxygenated $[\text{Cu}_3(\mu\text{-O})_3]^{2+}$ complexes for methane oxidation to methanol is much higher than that over binuclear $[\text{Cu}(\mu\text{-O})\text{Cu}]^{2+}$ site. The activation barriers of C–H bond cleavage over trinuclear sites are in good agreement with the reported apparent activation barrier experimentally. The rebound of CH_3 radical and OH fragment is highly exothermic and leads to adsorbed CH_3OH . This process is much more favourable than the diffusion away of the free radical from the active site observed over binuclear sites. Furthermore, the barriers for CH_3OH desorption over hydroxylated and oxygenated trinuclear sites are significantly lower than those over binuclear sites. It is due to the higher mobility of extraframework oxygens within the Cu clusters of higher nuclearity which not only facilitate the formation of methanol but also reduce the barrier for its subsequent elimination from the active site. It is proposed trinuclear copper clusters can play an important role in the selective oxidation of methane to methanol over Cu/ZSM-5 zeolite.

References

- [1] M.H. Groothaert, P.J. Smeets, B.F. Sels, P.A. Jacobs, R.A. Schoonheydt. *J. Am. Chem. Soc.* 127 (2005) 1394-1395.
- [2] N.V. Beznis, B.M. Weckhuysen, J.H. Bitter. *Catal. Lett.* 138 (2010) 14-22.
- [3] G.I. Panov, A.S. Kharitonov, V.I. Sobolev. *Appl. Catal., A* 98 (1993) 1-20.
- [4] V.I. Sobolev, K.A. Dubkov, O.V. Panna, G.I. Panov. *Catal. Today* 24 (1995) 251-252.
- [5] E.V. Starokon, M.V. Parfenov, L.V. Pirutko, S.I. Abornev, G.I. Panov. *J. Phys. Chem. C* 115 (2011) 2155-2161.
- [6] K.A. Dubkov, V.I. Sobolev, G.I. Panov. *Kinet. Catal.* 39 (1998) 72-79.
- [7] P.J. Smeets, M.H. Groothaert, R.A. Schoonheydt. *Catal. Today* 110 (2005) 303-309.
- [8] J.S. Woertink, P.J. Smeets, M.H. Groothaert, M.A. Vance, B.F. Sels, R.A. Schoonheydt, E.I. Solomon. *Proc. Natl Acad. Sci. USA* 106 (2009) 18908-18913.
- [9] P.J. Smeets, R.G. Hadt, J.S. Woertink, P. Vanelderen, R.A. Schoonheydt, B.F. Sels, E.I. Solomon. *J. Am. Chem. Soc.* 132 (2010) 14736-14738.
- [10] M.H. Groothaert, J.A. van Bokhoven, A.A. Battiston, B.M. Weckhuysen, R.A. Schoonheydt. *J. Am. Chem. Soc.* 125 (2003) 7629-7640.
- [11] M.H. Groothaert, K. Pierloot, A. Delabie, R.A. Schoonheydt. *Phys. Chem. Chem. Phys.* 5 (2003) 2135-2144.
- [12] A. Delabie, K. Pierloot, M.H. Groothaert, R.A. Schoonheydt, L.G. Vanquickenborne. *Eur. J. Inorg. Chem.* (2002) 515-530.
- [13] K. Pierloot, A. Delabie, M.H. Groothaert, R.A. Schoonheydt. *Phys. Chem. Chem. Phys.* 3 (2001) 2174-2183.
- [14] P. Vanelderen, J. Vancauwenbergh, B.F. Sels, R.A. Schoonheydt. *Coord. Chem. Rev.* 257 (2013) 483-494.
- [15] P. Vanelderen, R.G. Hadt, P.J. Smeets, E.I. Solomon, R.A. Schoonheydt, B.F. Sels. *J. Catal.* 284 (2011) 157-164.
- [16] C. Hammond, M.M. Forde, M.H. Ab Rahim, A. Thetford, Q. He, R.L. Jenkins, N. Dimitratos, J.A. Lopez-Sanchez, N.F. Dummer, D.M. Murphy, et al. *Angew. Chem. Int. Ed.* 51 (2012) 5129-5133.
- [17] M.H. Groothaert, K. Lievens, J.A. van Bokhoven, A.A. Battiston, B.M. Weckhuysen, K. Pierloot, R.A. Schoonheydt. *ChemPhysChem* 4 (2003) 626-630.
- [18] J.S. Woertink, L. Tian, D. Maiti, H.R. Lucas, R.A. Himes, K.D. Karlin, F. Neese, C. Wuertele, M.C. Holthausen, E. Bill, J. Sundermeyer, S. Schindler, E.I. Solomon. *Inorg. Chem.* 49 (2010) 9450-9459.
- [19] D. Maiti, J.S. Woertink, A.A.N. Sarjeant, E.I. Solomon, K.D. Karlin. *Inorg. Chem.* 47 (2008) 3787-3800.
- [20] R.A. Himes, K. Barnese, K.D. Karlin. *Angew. Chem. Int. Ed.* 49 (2010) 6714-6716.
- [21] R.L. Peterson, R.A. Himes, H. Kotani, T. Suenobu, L. Tian, M.A. Siegler, E.I. Solomon, S. Fukuzumi, K.D.

On the nature of active sites and mechanism of selective methane oxidation over Cu/ZSM-5 zeolite

- Karlin. *J. Am. Chem. Soc.* 133 (2011) 1702-1705.
- [22] S.T. Prigge, B.A. Eipper, R.E. Mains, L.M. Amzel. *Science* 304 (2004) 864-867.
- [23] R. Balasubramanian, S.M. Smith, S. Rawat, L.A. Yatsunyk, T.L. Stemmler, A.C. Rosenzweig. *Nature* 465 (2010) 115-131.
- [24] G.S. Nunes, I. Mayer, H.E. Toma, K. Araki. *J. Catal.* 236 (2005) 55-61.
- [25] M.J. Nappa, R.J. McKinney. *Inorg. Chem.* 27 (1988) 3740-3745.
- [26] E.I. Solomon, J.W. Ginsbach, D.E. Heppner, M.T. Kieber-Emmons, C.H. Kjaergaard, P.J. Smeets, L. Tian, J.S. Woertink. *Faraday Discuss.* 148 (2011) 11-39.
- [27] A. Burkhardt, E.T. Spielberg, H. Görls, W. Plass. *Inorg. Chem.* 47 (2008) 2485-2493.
- [28] A. Banerjee, R. Singh, P. Mondal, E. Colacio, K.K. Rajak. *Eur. J. Inorg. Chem.* 2010 (2010) 790-0798.
- [29] S.I. Chan, V.C.C. Wang, J.C.H. Lai, S.S.F. Yu, P.P.Y. Chen, K.H.C. Chen, C.-L. Chen, M.K. Chan. *Angew. Chem. Int. Ed.* 46 (2007) 1992-1994.
- [30] P.P.Y. Chen, R.B.G. Yang, J.C.M. Lee, S.I. Chan. *Proc. Natl Acad. Sci. USA* 104 (2007) 14570-14575.
- [31] S.I. Chan, S.S.F. Yu. *Acc. Chem. Res.* 41 (2008) 969-979.
- [32] S.I. Chan, C.Y.C. Chien, C.S.C. Yu, P. Nagababu, S. Maji, P.P.Y. Chen. *J. Catal.* 293 (2012) 186-194.
- [33] P.P.Y. Chen, S.I. Chan. *J. Inorg. Biochem.* 100 (2006) 801-809.
- [34] E.I. Solomon, R. Sarangi, J.S. Woertink, A.J. Augustine, J. Yoon, S. Ghosh. *Acc. Chem. Res.* 40 (2007) 581-591.
- [35] K. Yoshizawa. *Acc. Chem. Res.* 39 (2006) 375-382.
- [36] J. A. Lercher, A. van Veen. *TU Munich, unpublished results.*
- [37] H. van Koningsveld, J.C. Jansen, H. van Bekkum. *Zeolites* 10 (1990) 235-242.
- [38] E.A. Pidko, E.J.M. Hensen, R.A. van Santen. *Proc. R. Soc. A* 468 (2012) 2070-2086.



SUMMARY

STRUCTURE AND REACTIVITY OF IRON AND COPPER-CONTAINING HIGH-SILICA ZEOLITES

Transition metal-exchanged high-silica zeolites are efficient catalysts for a wide variety of chemical reactions. Among them, iron and copper modified high-silica ZSM-5 zeolite have been intensively investigated during the past two decades because they show unique catalytic activity and selectivity in several important chemical processes. However, the molecular picture underlying the catalytic properties and the structure of the extraframework iron- and copper containing species stabilized in micropores of ZSM-5 zeolite is still ambiguous and under intense debate. Therefore, identification of particular structures responsible for specific reactivity represents one of the major challenges in our understanding of the origin of the unique catalytic properties of iron- and copper-modified ZSM-5 catalysts.

This work aimed at developing a fundamental understanding of the factors that control structure and reactivity of extraframework cationic species in high-silica zeolites. In Chapter 2, the distribution and stability of isolated mononuclear and binuclear cationic iron-containing species, as well as other multinuclear complexes have been investigated by periodic DFT calculations and *ab initio* thermodynamic analysis. It is found that the zeolite local environment and the location of framework aluminum ions strongly influence the distributions of iron complexes in the zeolite micropores. The charge-compensation of bivalent cations in the zeolite necessitates the presence of two negatively-charged $[\text{AlO}_2]^-$ framework sites in its immediate vicinity. Moreover, highly symmetric location of lattice anions in the first coordination sphere of the cation is the key factor for its efficient stabilization. Among all potential positions, only six-membered rings α -, β -, and δ - cation sites with particular distributions of lattice Al atoms can accommodate exchangeable Fe^{2+} species. Because of the low flexibility of alternative double five-membered ring sites, the respective configurations of Fe^{2+} show the lowest stability.

The stability of alternative mononuclear $[\text{FeO}]^+$ cations is much less sensitive to the local geometry of the zeolite cation sites. Although six- and eight-membered ring sites are the preferred locations for such hypothetical species, it can be efficiently stabilized at any position inside ZSM-5 containing a framework $[\text{AlO}_2]^-$ anion required for the overall charge-neutrality. However, an important conclusion of this study is that despite being widely discussed in literature, such mononuclear $[\text{FeO}]^+$ cations cannot be formed in zeolites even with a very low Si/Al ratio in the framework. Because of the very high basicity of the extra-framework oxygen ion and pronounced coordination unsaturation of the iron center, such species readily self-organize into much more stable binuclear complexes. This process is proposed to be a general phenomenon for transition

Summary

metal-exchanged high-silica zeolite. The equivalent number of negative framework charges in adjacent positions is not necessary for the formation of multiple-charged binuclear oxygenated complexes.

The stability and interconversion of a wide range of different bi- and multinuclear Fe-containing complexes has been further investigated to elucidate the structures of the predominant species formed in Fe/ZSM-5 catalysts. It is demonstrated that neutral four-nuclear Fe-oxo and -hydroxo clusters are highly mobile and can be readily protonated by zeolite Brønsted acid sites resulting in hydroxylated cationic clusters. Several reaction paths for further transformations of these species were proposed and investigated. All of these paths lead to the formation of binuclear oxygenated $[\text{Fe}(\mu\text{-O})\text{Fe}]^{2+}$ and $[\text{Fe}(\mu\text{-O})_2\text{Fe}]^{2+}$ cations. Based on these results of DFT calculations, an *ab initio* thermodynamic analysis of the stability of different Fe complexes during catalyst activation has been performed. It is shown that at high temperature and O_2 free conditions, binuclear Fe^{II} -containing $[\text{Fe}(\mu\text{-O})\text{Fe}]^{2+}$ species are predominantly formed. When the activation process is carried out in oxygen-rich atmosphere, the alternative Fe^{III} -containing $[\text{Fe}(\mu\text{-O})_2\text{Fe}]^{2+}$ complexes are formed.

Thus, it is shown that the stabilization of isolated Fe^{2+} cations can only be achieved within a limited number of specific zeolite sites composed of six-membered zeolite rings with symmetrically distributed framework Al ions. In high-silica zeolites, the number of such configurations is low and most of the zeolite sites are occupied by multinuclear iron complexes, namely $[\text{Fe}(\mu\text{-O})_2\text{Fe}]^{2+}$ and $[\text{Fe}(\mu\text{-O})\text{Fe}]^{2+}$. The relative distribution of these sites depends on the conditions of catalyst activation.

The investigation of the stability of different Fe-containing extraframework complexes was followed by a DFT study of their reactivity in the selective oxidation of benzene to phenol reaction. Main results of this study are summarized in Chapter 3. It is shown that the reactivity of isolated mononuclear Fe^{2+} cations does not strongly depend on the local zeolite environment. The activation barriers and reaction energies for initial active oxygen generation step over different Fe^{2+} configurations are very similar. However, for subsequent benzene oxidation reaction, the reaction energy profile is sensitive to the confinement of zeolite framework on the reactant and product. A stronger confinement of the reaction intermediates may facilitate the desorption process of phenol and regeneration of the active Fe^{2+} site.

Independent of chemical composition, all considered alternative oxygen-containing Fe complexes show relatively low barriers for the initial N_2O activation and the formation of reactive extraframework oxygen centers. Although their reactivity towards N_2O bond dissociation is slightly lower than that of the mononuclear Fe^{2+} , subsequent C–H activation is much more favorable over these species. Nevertheless, the reaction cannot proceed over these oxygenated sites in a catalytic manner. In the presence of strongly basic extraframework oxygen ions, adsorbed phenol formed at the end of the reaction heterolytically dissociates over the $\text{Fe}^{\delta+}\cdots\text{O}^{\delta-}$ acid-base pair yielding a phenolate species

(C₅H₆O⁻) and an OH group grafted to iron sites. This reaction competes with the phenol desorption step that is necessary for the regeneration of the active site. These bulky phenolate species block the zeolite channels and thus decrease the accessibility of the active sites. They are proposed to be coke precursors contributing to the fast deactivation of Fe/ZSM-5 zeolite catalysts during benzene oxidation to phenol reaction. Thus, only isolated exchangeable Fe²⁺ cations in ZSM-5 zeolite can promote benzene oxidation to phenol in a catalytic manner, whereas all other types of extraframework species mainly contribute to the catalyst deactivation.

In Chapter 4, the reactivity of different mononuclear and binuclear iron-containing species towards N₂O decomposition and O₂ evolution has been investigated. It is shown that the reactivity in this case is very different from that observed in the case of benzene oxidation. Both mononuclear and binuclear iron-containing species exhibit high activity for the activation of the first N–O bond and the generation of a highly reactive extraframework oxygen atom. However, the activation barriers for the subsequent dissociation of a second N₂O molecule over isolated iron complexes are too high to be realized under practical condition. The catalytic reaction is therefore not possible over the mononuclear Fe species. Nevertheless, the migration and recombination of extraframework oxygen species over different mononuclear centers cannot be ruled out and could be the rate-limited step of the overall reaction when Fe/ZSM-5 materials predominantly containing such sites are considered. The N₂O decomposition over the predominant binuclear [Fe(μ-O)Fe]²⁺ and [Fe(μ-O)₂Fe]²⁺ is much more favorable. The reaction mechanism involves an interconversion of these complexes during the catalytic process. An important observation is that numerous spin-crossing transitions occurring at different elementary reaction steps dramatically modify the reaction energy diagram. The electronic structure of the reaction intermediates is continuously changing following the structural rearrangement and the change of the interaction between the iron and extraframework oxygen atoms. To get a further insight into the reaction mechanism and to provide a basis for comparison between the DFT results and the available experimental observations, a microkinetic analysis of the N₂O decomposition reaction over the preferred binuclear sites was performed. The calculated apparent activation barrier of the overall reaction is in a good agreement with the experimental results. In line with the available experimental results, the reaction order with respect to N₂O is decreasing from 1 → 0 at low temperatures and then again increases to 1 at temperatures above 800 K. This evidences that the rate-determining step of the reaction depends on the temperature. At very low temperatures, the reaction is limited by the initial dissociation of N₂O, while in the intermediate temperature regime O₂ recombination becomes rate-limiting. At high temperature, because of the weak adsorption, again N₂O dissociation becomes the rate-determining step.

The results in Chapter 3 and 4 clearly demonstrate that different extraframework Fe species are responsible for the activity of Fe/ZSM-5 in the oxidation of benzene to phenol and in the catalytic N₂O decomposition. In the former process, only isolated Fe²⁺ cations

Summary

promote the catalytic reaction, whereas the dominant multinuclear oxygenated species contribute to the catalyst deactivation. On contrary, N_2O decomposition proceeds in a catalytic manner only over binuclear sites.

In Chapter 5, the study is further extended into the relationship between the properties of extraframework copper-exchanged ZSM-5 zeolites and their reactivity in direct methane oxidation to methanol. The reactivity of both the generally accepted binuclear cationic $[Cu(\mu-O)Cu]^{2+}$ and newly proposed trinuclear complexes was considered. It is found that despite the initial homolytic (radical) dissociation of C–H bond in methane can occur over a wide range of zeolite cations, subsequent selective radical recombination and methanol formation necessitates very specific properties of the active site. The free CH_3 radical formed over binuclear $[Cu(\mu-O)Cu]^{2+}$ site prefers to diffuse away to bond to basic zeolite lattice rather than to rebound with bridging OH group of $[Cu(\mu-OH)Cu]^{2+}$ to form adsorbed methanol. Methanol in this case can only be obtained by extraction with protic solvent. Here, alternative reaction species are proposed. A plausible path for the formation of alternative intrazeolitic Cu complexes with a nuclearity higher than 2 is demonstrated. The availability of several low-lying electronic states in trinuclear Cu clusters is shown to be the key for a facile rebound of the activated radical species and the formation of molecular methanol. Moreover, methanol desorption from such active sites is much easier than that from the binuclear complexes because of the higher mobility of extraframework oxygen atoms. Thus, the copper clusters with nuclearity higher than 2 are suggested to be promising active sites for selective methane oxidation to methanol.

The results presented in this thesis contribute to a fundamental understanding of the stability and reactivity of iron and copper exchanged ZSM-5 catalysts. This investigation can provide constructive suggestions for the design of novel tailor-made transition metal-exchanged high-silica zeolites for particular catalytic reactions.

ACKNOWLEDGEMENTS

At the end of my thesis, when looking back over the two years spent in the Netherlands, my heart is full of gratitude, my mind is filled with all wonderful memories despite that this journey was sometimes accompanied by confusion, stress and uncertainty. I would like to take these last words of my thesis to acknowledge all the people who have contributed to this thesis.

First and foremost, I would like to give appreciation to my three inspiring supervisors: Prof. Rutger van Santen, Prof. Can Li, and Dr. Evgeny A. Pidko. Actually, I never thought I had the courage to challenge a double doctoral degree in the Netherlands if I hadn't been studying in Rutger's group for one year from 2009-2010. From this experience, I was encouraged to continue doing research on an interesting and challenging topic. Fortunately I made a correct decision. Rutger, thank you for giving me motivation and inspiration. Your invaluable insight and comments imposed me to learn a new research field and to work on a different project. I am very grateful to you for your careful guidance and inspiring discussions throughout my PhD study in the Netherlands.

I would also express my gratitude to Prof. Can Li. I thank you so much for giving me the opportunity to work in your group in DICP and to join the PSA program between China and the Netherlands. Your strategic suggestion of cooperation through a double doctoral degree program between DICP and TU/e initiated my PhD study in the IMC group and eventually this thesis. I couldn't finish this thesis in time without your previous five years of supervision. You taught me how to learn scientific knowledge in a correct and efficient way, how to do research with a critical attitude, and how to keep great enthusiasm despite the very challenging scientific problems in front of me. I am really grateful for all these scientific qualities and personalities learned from you, which are worth treasuring for my whole life.

Dear Evgeny, my PhD work could not be done without your careful help. You deserve my special thanks. You have taught me much regarding the field of zeolites. You always added great insight into my project and gave me so many practical advices, and most of all, you were always there for me when I was lost in the project. More importantly, I got a lot of inspiration from your wisdom, hard work, and enthusiasm. I would also love to thank you for your tireless correction of my manuscript and thesis. Especially during the stressful and frustrating times in thesis writing, your encouragement and help to me is invaluable and a source of motivation. In addition, thank you very much for your encouragement and taking care of me to make me more confident, release my shyness and culture shock abroad, and get along well with our group. Thank you for everything you did for me. What I learned from you and would like to share with others is that you taught me: "In chemistry everything is the same, just close your eyes play and have fun with the atoms".

Acknowledgements

During the last two years in IMC group, I had a lot of fruitful discussions with Prof. Emiel Hensen. I acknowledge all your suggestions and instructions given on my project. I am grateful to you for all your elegant comments and fresh ideas on my results and for reviewing my manuscript. I also would like to thank you for your support and arrangement of every procedure for my PhD study in TU/e. Thank you very much!

With regard to my project on zeolites, I must thank one important colleague in DICP, Dr. Fengtao Fan. You were the first person who taught me research about zeolites and inspired my interest in it and finally I chose it as my thesis project. Thank you for involving me into a lot of discussions of Raman spectra and zeolites. You were also the first person who cooperated with me on computational chemistry. I really appreciate your trust and support when I was unconfident and hesitant about my simulation project.

I would like to extend my thanks to Cristina and Ivo. Cristina, thank you very much for helping me finish the thermodynamic analysis part of my thesis. All the discussions with you were very helpful. Ivo, thank you for your contributions towards the microkinetic analysis part of my work. I also enjoyed the C++ course and theoretic group lunch meeting a lot. Thank you for your time and patience to organize them. My thanks also go to Evi, who taught me how to perform microkinetic analysis. Thank you all for many interesting discussions and fruitful cooperations.

It was my pleasure to work together with many nice colleagues in the theory subgroup. Pieter, thank you for the computational administration and VASP learning. Weiyu, thank you for all the helpful discussions about theory, software, and up-to-date literature. The quantum chemistry books and useful online information shared from you were very nice. It was my great pleasure to work with you. Shuxia and Xueqing, thank you for offering a warm and nice working atmosphere in STW 4.27. Also a lot of scientific discussions were delivered. My thanks are also given to Tianwei, Tonek, Minhaj, and Gang Yang for your kind help.

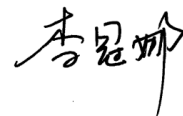
All the people in IMC group are acknowledged for the kind help and friendship. I am thankful to the beautiful and fashionable Emma for giving me a lot of help in administrative matters and fun in IMC. I also would like to express my gratitude to Lennart and Tamas, two very nice officemates in STW 3.26.

My life in the Netherlands would be boring if without the friendship with so many nice persons. Yanmei, thank you for picking me up at Eindhoven station and making my life in Eindhoven much easier. Mian, thank you for accompanying me during the last two years in TU/e, especially for your and Yanmei's help in the first few months which released my home-sickness a lot. The times we spent together were indeed the most memorable days of my life in Eindhoven. I believe the friendship among "Lücha", "Xiaotu", and "Diandian" will last forever. Many thanks to Liu Peng and his family, Peiyuan and his family for helping me a lot. Shuxia, I miss the time we took walks together after lunch, playing table tennis, shopping in the weekends, the very nice food and evenings at your home. I also thank you for sharing lots of pregnancy knowledge. I wish you and your family have a

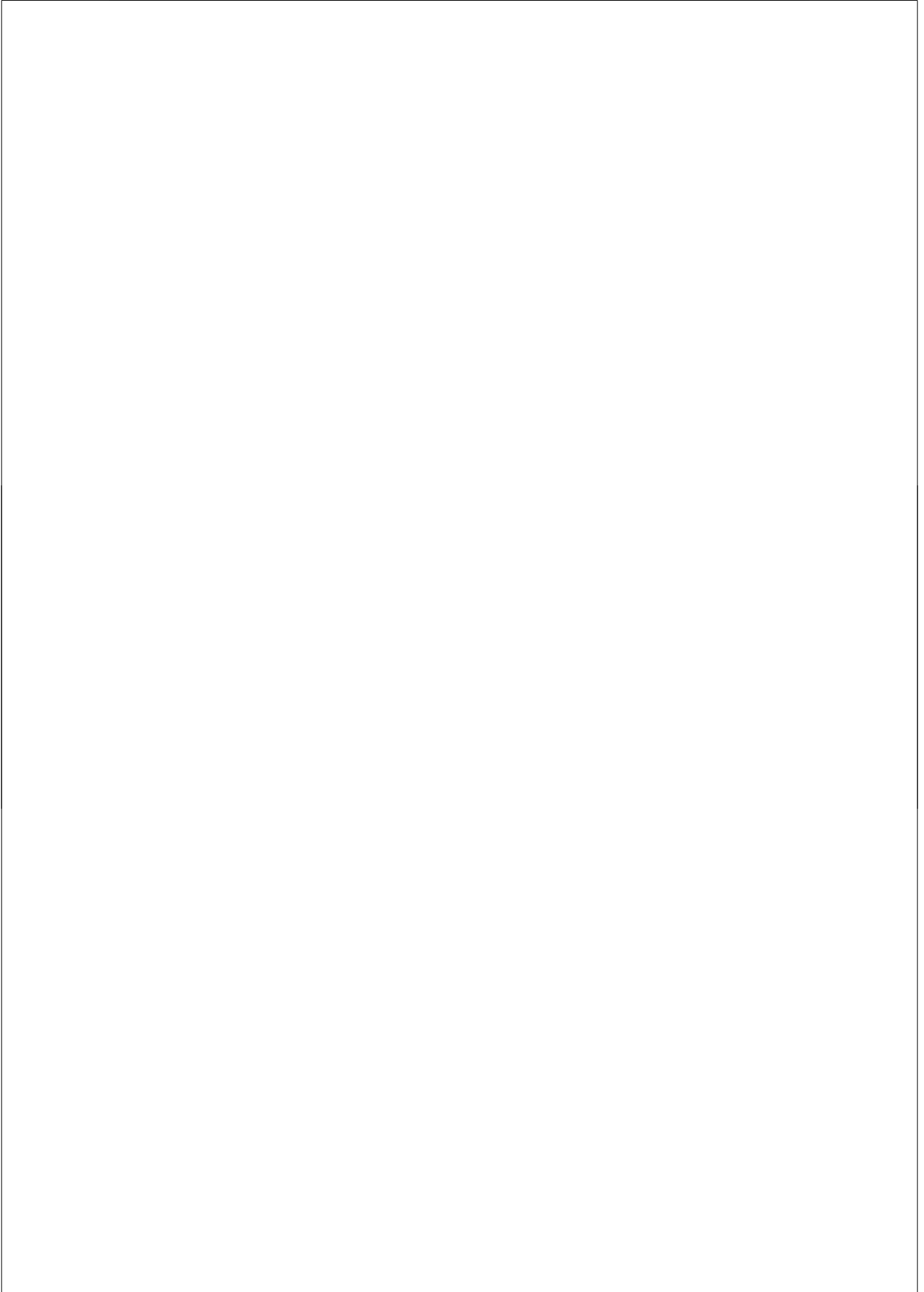
very happy life in the future. Leilei, Yi, and Tianwei, Thank you for your help and so many enjoyable times with you all. Many thanks to our lunch partners: Alessandro and Xianyang Quek. The chats during lunch are always very interesting and relaxing. My thanks also go to Xueqing, Gao Lu, Chen Delei for your kind help both at work and life. I would like to thank all the girls in Chinese Dance Group. I really enjoyed all the shining Sunday afternoons with beautiful dance and music. I thank Li Jing, the founder of the dance group, for accepting me into the group and giving me help. I highly appreciate the three lovely girls, Bilin, Tang Pei and Caixia, who live in Spacebox. Dear girls, thank you so much for your friendship. I enjoyed very much all the wonderful spare time we spent together. I wish you dear girls all the best for your study and life in the Netherlands, and meet your unique Mr. Right at the right time. Haodong, thank you for your help at life. You were a very nice “uncle” who always tolerated our jokes. We missed our “uncle” a lot after your went back to China. Caixia, thank you for your kindhearted help. Tang Pei and Bilin, I really acknowledge you for the delicious noodles and dishes you cooked for me, the relaxing chat and singing with you when I was very exhausted with thesis writing. The times were so warm and huge sources of my refreshment.

Besides the friends in TU/e, my friends in Dalian also deserve my deep appreciation. Many thanks go to Prof. Zhaochi Feng, Guoqing and her family, Fengtao, Meiling, Wang Xiang, Dong’e, Xiuli, Jingxiu. Your continuous greetings, support, and friendship were among the most important sources of my happiness in the Netherlands. Meiling, Fengtao, and Guo Qiang, I thank you all for the enjoyable activities we spent together in the Netherlands.

Last, but certainly not least, I would like to thank my parents, my grandparents, my brother and sister, and my husband. I am deeply indebted to you for providing me infinite support and love. Dear baba and mama, I deeply appreciate everything you give me in my life. Dear grandpa and grandma, thank you for your love, cherishing, and enlightened educations during my childhood. You are gone but always with me in my heart. Dear brother and sister, whom I grew up with, your love makes me never feel alone. Dear pengpeng, thank you for giving me your kindness, tolerance, and love. Thank you very much for everything you have done for me. In your eyes, I see the better in me. I love you all forever!



Eindhoven, Jan. 2013



LIST OF PUBLICATIONS

1. **Guanna Li**, Evgeny A. Pidko, Rutger A. van Santen, Zhaochi Feng, Can Li*, Emiel J. M. Hensen*, Stability and reactivity of active sites for direct benzene oxidation to phenol in Fe/ZSM-5: a comprehensive periodic DFT study, *J. Catal.*, **2011**, *284*, 194-206. (**Chapter 2-3**)
2. **Guanna Li**, Evgeny A. Pidko, Rutger A. van Santen, Can Li*, Emiel J.M. Hensen*, Stability of Extraframework Iron-containing Complexes in ZSM-5 Zeolite, *J. Phys. Chem. C*, **2013**, *117*, 413-426. (**Chapter 2**)
3. **Guanna Li**, Evgeny A. Pidko, Ivo A.W. Filot, Rutger A. van Santen, Can Li*, Emiel J.M. Hensen*, Catalytic Properties of Extraframework Iron-containing Species in ZSM-5 for N₂O Decomposition, *in preparation*. (**Chapter 4**)
4. **Guanna Li**, Pieter Vassilev, Evgeny A. Pidko*, Emiel J.M. Hensen*, On the nature of active sites and mechanism of selective methane oxidation over Cu/ZSM-5 zeolite, *in preparation*. (**Chapter 5**)

Others during study in DICP

5. Meiling Guo, **Guanna Li**, Fengtao Fan, Zhaochi Feng, Can Li*, Enhancement of the visible light absorption intensity of microporous vanadosilicate AM-6, *Chem. Commun.*, **2012**, *48(97)*, 11892-11894.
6. Qiang Guo, Keju Sun, Zhaochi Feng, **Guanna Li**, Meiling Guo, Fengtao Fan*, Can Li*, A Thorough Investigation on the Active Titanium Species in TS-1 Zeolite by In Situ UV Resonance Raman Spectroscopy, *Chem. Eur. J.*, **2012**, *18(43)*, 13854-13860.
7. Meiling Guo, Zhaochi Feng, **Guanna Li**, Jan P. Hofmann, Evgeny A. Pidko, Pieter C.M.M. Magusin, Qiang Guo, Bert M. Weckhuysen, Emiel J.M. Hensen, Fengtao Fan*, Can Li*, "Extracting" the key fragment of ETS-10 crystallization and its application in AM-6 assembly, *Chem. Eur. J.*, **2012**, *18(38)*, 12078-12084.
8. Shi Qiu, **Guanna Li**, Peng Wang, Guoqing Jia, Zhaochi Feng*, Can Li*, Hydrogen bonding in homochiral dimers of hydroxyesters studied by Raman Optical Activity spectroscopy, *J. Raman Spectrosc.* **2012**, *43*, 503-513.
9. Shi Qiu, **Guanna Li**, Shengmei Lu, Baokun Huang, Zhaochi Feng*, Can Li*, Chiral Sulfur Compounds Studied by Raman Optical Activity: tert-Butanesulfinamide and its Precursor tert-Butyl tert-Butanethiosulfinate, *CHIRALITY*, **2012**, *24*, 731-740.
10. **Guanna Li**, Guoqing Jia, Qiang Gao, Zhaochi Feng*, Can Li*, Effect of Substituted Groups on the Electronic Circular Dichroism of Aldols: A Combined Experimental and Time-Dependent DFT Study, *J. Phys. Chem. C*, **2011**, *115*, 972-981.

List of publications

11. Shi Qiu[§], **Guanna Li**[§], Peng Wang, Jun Zhou, Zhaochi Feng*, Can Li*, pH-Dependent Chirality of L-Proline Studied by Raman Optical Activity and DFT, *J. Phys. Chem. A*, **2011**, *115*, 1340-1349. ([§]co-author)
12. Shi Qiu[§], **Guanna Li**[§], Peng Liu, Changhao Wang, Zhaochi Feng*, Can Li*, Chirality transition in the epoxidation of (-)- α -pinene and successive hydrolysis studied by Raman optical activity and DFT, *Phys. Chem. Chem. Phys.*, **2010**, *12*, 3005-3013. ([§]co-author)
13. Guoqing Jia, Shi Qiu, **Guanna Li**, Jun Zhou, Zhaochi Feng*, Can Li*, Alkali-hydrolysis of D-glucono-delta-lactone studied by chiral Raman and circular dichroism spectroscopies, *Sci. China, Ser. B*, **2009**, *52*, 552-558.
14. Fengtao Fan, Zhaochi Feng, **Guanna Li**, Keju Sun, Pinliang Ying, Can Li*, In Situ UV Raman Spectroscopic Studies on the Synthesis Mechanism of Zeolite X, *Chem. Eur. J.*, **2008**, *14*, 5125-5129.

CURRICULUM VITAE

Guanna Li was born on 17th of February 1983 in Ruzhou, Henan province, CHINA. After finishing her bachelor degree on Chemistry from Department of Chemistry, Zhengzhou University in 2005, she started a master-doctor continuous project in State Key Laboratory of Catalysis, Dalian institute of chemical physics, Chinese Academy of Science (DICP, CAS), under the supervision of Prof. Can Li. During her PhD study, she participated in the Program for Strategic Scientific Alliances between China and The Netherlands (PSA). From Oct. 2009 to Oct. 2010, she was supported by PSA program as a guest PhD student in Inorganic Materials Chemistry group (IMC), Department of Chemical Engineering and Chemistry, Eindhoven University of Technology (TU/e), the Netherlands. In Oct. 2011, she obtained her PhD degree from DICP with the project of Density Functional Theory Calculations on Chiroptical Spectra and Active Sites in Fe/ZSM-5 Catalyst. Then she continuously worked on a double doctoral degree program between DICP and TU/e in IMC group, under the supervision of Prof. Rutger A. van Santen. Her research during this period was mainly focused on the development of fundamental understanding of the structures and catalytic properties of iron and copper exchanged high-silica ZSM-5 zeolites by computational methods. The most important results are reported in this thesis.

